Alma Mater Studiorum – Università di Bologna

DOTTORATO DI RICERCA IN

SCIENZE CHIMICHE

Ciclo XXVI

Settore concorsuale di afferenza: O3/C1–CHIMICA ORGANICA

Settore Scientifico disciplinare: CHIM/06–CHIMICA ORGANICA

Silica-Supported Gold Nanoparticles: Synthesis, Characterization and Reactivity

Presentata da:

Silvia Fazzini

Coordinatore Dottorato:

Prof. Aldo Roda

Relatore:

Prof. Daniele Nanni

Correlatori:

Prof. Barbara Ballarin

Prof. Maria Cristina Cassani

Prof. Jean-Sebastién Girardon

Esame finale anno 2014

Thesis scope and organization

The aim of this work was the synthesis and applications of functionalized-silica-supported metal (namely gold) nanoparticles. The silica-anchored functionalities, e.g. amine, alkynyl carbamate, and sulfide moieties, have been chosen in order to both capture and spontaneously reduce the gold precursor, and to stabilize the resulting nanoparticles avoiding their mobility and aggregation. In the literature only few works are reported where analogous techniques have been employed, yielding, in general, quite large nanoparticles. This new synthetical strategy, potentially suitable for catalysis applications, represents a good challenge toward a more "green" synthesis of supported gold nanoparticles, since it avoids use of additional reducing agents.

Various methods of characterization have been used, such as ultraviolet-visible (UV-Vis) spectroscopy, transmission electron microscopy (TEM), dynamic light scattering (DLS), UV-Vis diffuse reflectance spectroscopy (UV-Drs), X-ray fluorescence (XRF), SEM-FEG microscopy, X-ray absorption spectroscopy (XAS), and X-ray photoionization (XPS).

In this thesis is also presented part of the work developed during a seven-months Marco Polo fellowship stay at the University of Lille (France) under the supervision of Dr. J. Girardon, regarding nanoparticles nucleation and growth inside a microfluidic system and the study of the corresponding mechanism by *in situ* characterization by XAS spectroscopy.

The singles chapters can be described as follows:

Chapter 1: general introduction to nanoparticles synthesis and their use in catalysis, followed by a description of the different techniques used to support gold nanoparticles (Au_{NPs}) in particular on silica.

Chapter 2: synthesis and characterization of stable silica-supported Au_{NPs} by addition of an $HAuCl_4$ aqueous solution to commercial polyethyleneimine-functionalized silica beads (SiO_2-PEI), followed by description of the resulting material as a catalytic system for reduction of 4-nitrophenol to 4-aminophenol by $NaBH_4$. These materials were also characterize by XAS analysis, which gave important structural information on gold oxidation state.

Chapter 3: synthesis and characterization of silica nanoparticles functionalized with alkynyl carbamate moieties and, subsequently, with amino-sulfide branches by using a click-chemistry approach (radical "thiol-yne" reaction): both these novel materials were reacted with $HAuCl_4$ to obtain silica-supported gold nanoparticles.

Chapter 4: study of the Turkevich gold nanoparticles synthesis ($HAuCl_4$ reacted with sodium citrate as both a reducing and a stabilizing agent) carried out under microfluidic set-up and *in situ* mechanistic studies by XAS spectroscopy (in collaboration with the University of Lille).

Chapter 5: preparation of gold nanoparticles supported by detonation nanodiamonds (DND) adding an aurate salt complex as precursor. The obtained system was used to reduce 4-nitrophenol to 4- aminophenol.

Contents

CHAPTER 1 - INTRODUCTION 1

1 INTRODUCTION 1

1.1 Gold Nanoparticles: a general overview 2

1.1.1 Optical Properties 2

1.1.2 Gold Colloids Synthesis 3

1.1.3 Mechanistic studies on Turkevich synthesis 7

1.1.4 Turkevich synthesis by a microfluidic set-up 10

1.2 Supported Gold Nanoparticles 11

1.2.1 Synthesis of heterogeneous gold catalysts 11

1.2.2 Reactions catalyzed by gold 14

1.3 Silica Nanoparticles 15

1.3.1 Functionalization of silica nanoparticles 17

1.4 Thiol-yne reaction 19

1.5 Characterization Techniques 21

1.5.1 X-ray absorption spectroscopy (XAS) 21

1.5.2 X-ray photoelectron spectroscopy (XPS) 24

1.5.3 XRF spectrometers 25

1.5.4 Field emission gun scanning electron microscopy (SEM-FE) 26

1.5.5 Transmission electron microscopy (TEM) 27

1.6 Purpose of the work 29

CHAPTER 2 - SYNTHESIS OF GOLD NANOPARTICLES SUPPORTED ON COMMERCIAL SILICA-POLYETHYLENEIMINE BEADS 35

2.1 Results and Discussion 36

2.1.1 Characterization of SiO_2-PEI 36

2.1.2 Preparation of AuNPs/(SiO_2-PEI) beads 38

2.1.3 X-Ray Absorption Spectroscopy studies 44

2.1.4 Catalytic activity 50

2.2 Experimental Section 55

2.2.1 Materials 55

2.2.2 Instruments 55

2.2.3 Preparation of AuNPs/(SiO_2-PEI) beads 56

2.2.4 XAS Data Collection 57

2.2.5 Catalytic reduction of 4-nitrophenol (4-NP) 58

2.3 Conclusions 60

CHAPTER 3 - SYNTHESIS OF SUPPORTED GOLD NANOPARTICLES BY FUNCTIONALIZED SILICA NANOPARTICLES 64

3.1 Results and Discussion 65

3.1.1 Alkyne-functionalized silica nanoparticles (SiO_2@Yne) 65

3.1.2 Thiol-yne functionalized silica nanoparticles (SiO_2@Thio-Yne) 76

3.1.3 AuNPs supported by SiO_2@Yne (Au-SiO_2@Yne) 86

3.1.4 AuNPs supported by SiO_2@Thio-Yne (Au- SiO_2@Thio-Yne) 95

3.2 Conclusions 102

3.3 Experimental Section 103

3.3.1 Materials 103

3.3.2 Synthesis of [3-(2-Propynylcarbamate)propyl]triethoxysilane 103

3.3.3 General preparation of Alkyne-Functionalized Silica Nanoparticles (SiO_2@Yne) 104

3.3.4 Thiol-yne reaction on with propargyl alcohol and cysteamine hydrochloride 105

3.3.5 General method to prepare SiO_2@Thio-Yne 105

3.3.6 Synthesis of Au-SiO_2@Yne and Au-SiO_2@Thio-yne 106

3.3.7 Charachterization 106

3.4 Appendix 108

3.4.1 SiO_2@Thio-Yne Thermograms 108

3.4.2 NMR and ES-MS spectra 110

3.4.3 XPS DATA 111

3.4.4 FT-IR 113

CHAPTER 4 - DIRECT INVESTIGATION OF GOLD NANOPARTICLES FORMATION INSIDE A MICROFLUIDIC CHANNEL BY IN SITU XANES SPECTROSCOPY 116

4.1 Results and Discussion 117

4.1.1 Gold nanoparticles synthesis by a microfluidic set-up 117

4.1.2 Microfluidic setup adapted to in situ XANES characterization 119

4.2 Experimental section 124

4.2.1 Materials 124

4.2.2 XAS Data Collection 124

4.3 Conclusion 125

CHAPTER 5 - GOLD NANOPARTICLES ON NANODIAMOND AS NEW GENERATION CATALYST 128

5.1 Results and Discussion 129

5.1.1 Synthesis of Au-NDs 129

5.1.2 Characterization of Au-ND 129

5.1.3 Catalysis 132

5.2 Conclusions 135

5.3 Experimental Section 136

5.3.1 Materials 136

5.3.2 Synthesis of Au-ND 136

5.3.3 Catalysis 136

5.4 APPENDIX 138

CHAPTER 1 ..... **1**

1 INTRODUCTION **1**

1.1 Gold Nanoparticles: a general overview **2**
1.1.1 Optical Properties 2
1.1.2 Gold Colloids Synthesis 3
1.1.3 Mechanistic studies on Turkevich synthesis 7
1.1.4 Turkevich synthesis by a microfluidic set-up 10

1.2 Supported Gold Nanoparticles **11**
1.2.1 Synthesis of heterogeneous gold catalysts 11
1.2.2 Reduction of aromatic nitro compounds 13

1.3 Silica Nanoparticles **15**
1.3.1 Functionalization of silica nanoparticles 17

1.4 Thiol-yne reaction **19**

1.5 Characterization Techniques **21**
1.5.1 X-ray absorption spectroscopy (XAS) 21
1.5.2 X-ray photoelectron spectroscopy (XPS) 24
1.5.3 XRF spectrometers 25
1.5.4 Field emission gun scanning electron microscopy (SEM-FEG) 26
1.5.5 Transmission electron microscopy (TEM) 27

1.6 Purpose of the work **29**

CHAPTER 1

1 Introduction

Nanotechnology is one of the largest and most rapidly growing interdisciplinary research fields in modern science and engineering. Nanotechnology deals with design, characterization, production, and application of structures, devices, and systems with shape and size at nanometric scale.[1]

Nanomaterials (1-100 nm scale) exhibit unique optical, electronic and catalytic properties, different from those of the bulk state or separate atoms. As particles size decreases, the number of surface atoms becomes equal to, or even exceeds, the number of inner-core atoms. By this maximization of surface area and quantic confinement, new properties derive, strictly dependent on size and shape of the structure, rather than on the nature of the material.[2,3,4] Noble metal nanoparticles (NPs), in particular, have attracted intense interest in biology, optics, and catalysis.[5,6,7] Among them, silver and gold nanoparticles (Au_{NPs}) are among the most remarkable members of metal nanoparticles, with fascinating aspects and applications, e.g. in surface plasmonics, surface enhanced Raman scattering (SERS), chemical and biological sensing, photo-thermal therapy, and catalysis.[8,9]

Catalysis by gold is a topic of widespread up-to-date interest. It was believed for a long time that Au lacked any catalytic activity, until Haruta discovered that Au_{NPs}, supported on metal oxide surface, were catalytically active at low temperatures for CO oxidation.[10,11,12] Since this breakthrough considerable research efforts have been oriented towards gold catalysis, as it is shown by the exponential growth in the number of publications on this subject (Fig 1.1)

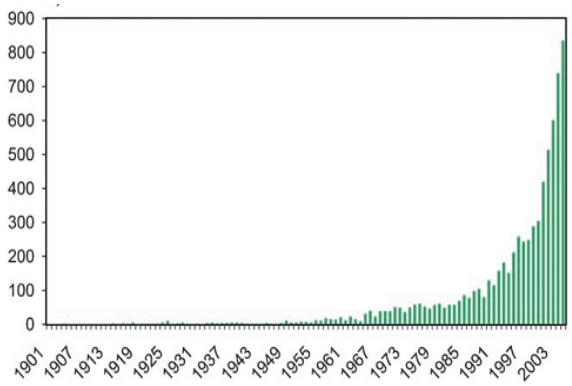

Figure1.1 Publications on heterogeneous catalysis by gold in the different years.[13]

The catalytic activity of gold, strictly connected to the nanoparticles size, can disappear completely as the particle size grows into the micrometric scale. Use of supported or unsupported nanoparticles in catalysis can provide a point of convergence between homogeneous and heterogeneous catalysis, two disciplines fairly independent.[14]

1.1 Gold Nanoparticles: a general overview

1.1.1 Optical Properties

In 1857 Faraday first prepared colloidal gold by reducing an aqueous solution of gold chloride with phosphorous in carbon disulfide. He was among the first to realize that this ruby red color arose from the presence of finely dispersed colloidal gold or gold nanoparticles, as known today.[15] The phenomenon that can explain the change in color from the bulk material (bright yellow color) to gold nanoparticles (ruby red for gold spheres of 15 nm) is the so-called *Localized Surface Plasmon Resonance* (LSPR), based on coherent interaction of free electrons in the conduction band of the metal with light. In bulk metals this effect is negligible due to a relatively low amount of surface electrons, while in nanoparticles, with a maximization of the surface area, a large portion of the electrons are at surface. As the wave front of the light passes, the electron density is polarized to one surface and oscillates in resonance at light frequency, causing a standing oscillation (Fig. 1.2)

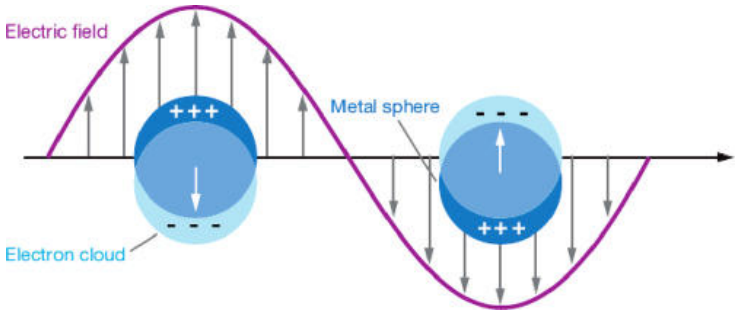

Figure1.2 Representation of interaction of an oscillating electric field with electron clouds of metal nanoparticles.[16]

In general, spherical gold nanoparticles absorb light in the visible region but, varying size and morphology of nanoparticles as well as the dielectric constant of the surrounding medium, the oscillation frequency of electrons can be changed, resulting in variation on scattering effects and absorption spectra (Fig. 1.3)

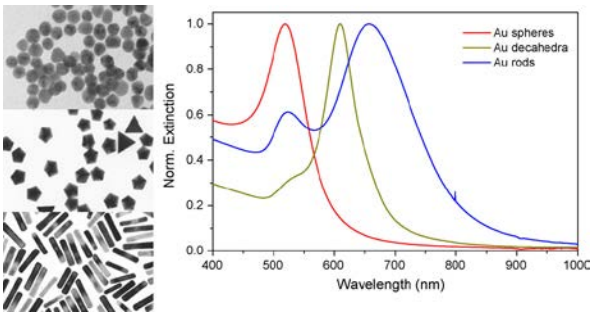

Figure1.3 Transmission electron micrographs and UV—Vis absorption spectra of gold-nanoparticle colloids with various geometries (spheres, decahedra, and rods).[17]

The absorption coefficient of the LSPR is orders of magnitude larger than that of strongly absorbing dyes. This property, conjugated with the possibility to vary the optic properties as function of the shape and size of the nanoparticles, make these particles very attractive for sensing, diagnostics, and photo-thermal therapeutic applications in many areas.[8] Above all, the absorption and scattering properties of gold nanoparticles can yield a lot of information about the structure and size of the nanoparticles themselves.

1.1.2 Gold Colloids Synthesis

Synthetic techniques to generate metal nanoparticles depend on isolation of small amounts of material. There are two general strategies to obtain materials on the nanoscale: *top down* and *bottom up* approaches (Fig. 1.4). For *top down* procedures, a bulk Au is systematically broken down to generate Au_{NPs} of desired dimensions. Common techniques are photolithography and electron beam lithography.[5] In the *bottom up* strategy the formation of Au_{NPs} originates from the assembly of atoms, produced by reduction of ions to generate nanostructures. Many reduction methods are available, such as templating, chemical, electrochemical, sono-chemical, thermal, and photochemical techniques. [18]

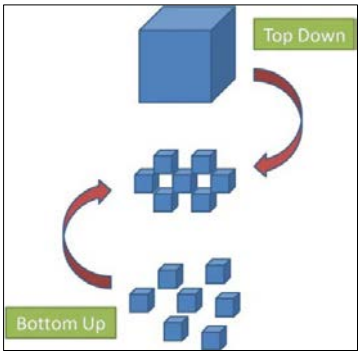

Figure1.4 Schematization of top-down and bottom-up approaches.

The chemical reduction method involves two steps: nucleation followed by growth. It is called *in situ* synthesis when the nucleation and successive growth are completed in the same

process; otherwise it is called *seed-growth method*. The traditional *in situ* synthesis provides spherical or quasi-spherical Au_{NPs}, whereas the seed-growth strategy has emerged as a very efficient method to synthesize mono-dispersed Au_{NPs} with large sizes (up to 300 nm) and well-defined shapes, e.g. rods, cubes, disks, wires, etc.[19,20,21,22,23]

Gold nanoparticles are generally prepared by *in situ* chemical reduction from a metal salt, a reductant, and a stabilizing agent. The latter has the important function to decrease the attractive Van der Waals forces between nanoparticles, providing the electrostatic and/or steric stabilization that can keep the particles at the right distance as to prevent aggregation.[24] Two of the most conventional methods to obtain gold colloids[i] are known as the Turkevich and Brust methods.[25,26]

The *Turkevich synthesis*, one of the oldest synthetic procedures (1950s),[25] implies addition of a gold precursor to a boiling sodium citrate aqueous solution, and it yields nanoparticles with an average diameter of 15 nm. In this synthesis the citrate anion plays the double role of a weak reducing agent (relatively high temperatures are required to reduce Au) and a capping agent, stabilizing the resulting nanoparticles both electrostatically and sterically (Fig 1.5).

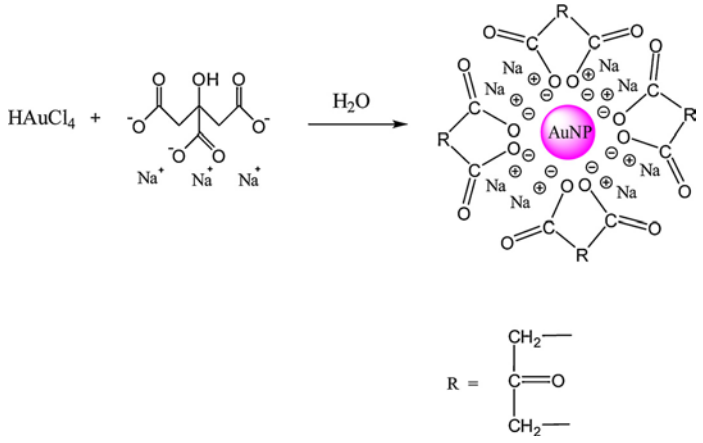

Figure1.5 Au_{NPs} synthesis using the *Turkevich method*. Sodium citrate molecules reduce first Au(III) to metallic gold Au(0) and then they are adsorbed on the nanoparticle surface, stabilizing the system and preventing further aggregation.[5]

In general, conditions such as the gold-to-citrate ratio, order of the addiction, and reagent concentrations control size distribution of the generated gold nano-spheres. In 1973, Frens published an improved approach where a broad size range of Au_{NPs} (from 15 to 150 nm) could be obtained by controlling the trisodium citrate to Au ratio.[27] Another remarkable modification was the reversed order of addition, that was conducted by adding $HAuCl_4$ to the citrate solution, producing

[i] IUPAC: The term *colloid* refers to a state of subdivision implying that the molecules or polymolecoular particles dispersed in a medium have, at least in one direction, a dimension roughly between 1 nm and 1 µm, or that in a system discontinuities are found at distances of that order.

mono-dispersed Au_{NPs} with a relatively small size (less than 10 nm).[28] Lately, several research groups focused their attention on improvement of the Turkevich-Frens method in order to promote the convenient use of citrate-stabilized Au_{NPs}. Moreover, many publications also aimed at understanding the mechanism of Au_{NPs} formation using this "old" protocol.[29]

Stabilization of gold nanoparticles by alkanethiols has been known since the late 1980s.[30] *Brust et al.* reported for the first time in 1994 a convenient two-phase synthesis of isolable and alkanethiolate-protected gold nanoparticles. In this reaction $HAuCl_4$ was transferred to toluene, using tetraoctylammonium bromide (TOAB) as a phase-transfer reagent, and reduced with aqueous sodium borohydride in the presence of dodecanethiol. On addition of the reducing agent, the organic phase changes in colour from orange to deep brown (within a few seconds) with formation of Au_{NPs} of 2–5 nm in diameter and a narrow size distribution (Fig. 1.6). Strong reducing agents such as $NaBH_4$, in the absence of thiolate ligands, would lead to aggregates formation in a short time; in that system, due to the great affinity between sulfur and gold, the nanoparticles are instead long-time stabilized. In the subsequent years this synthesis was extended to single-phase systems[31] and others phosphorous-, oxygen-, and nitrogen-based ligands.[32]

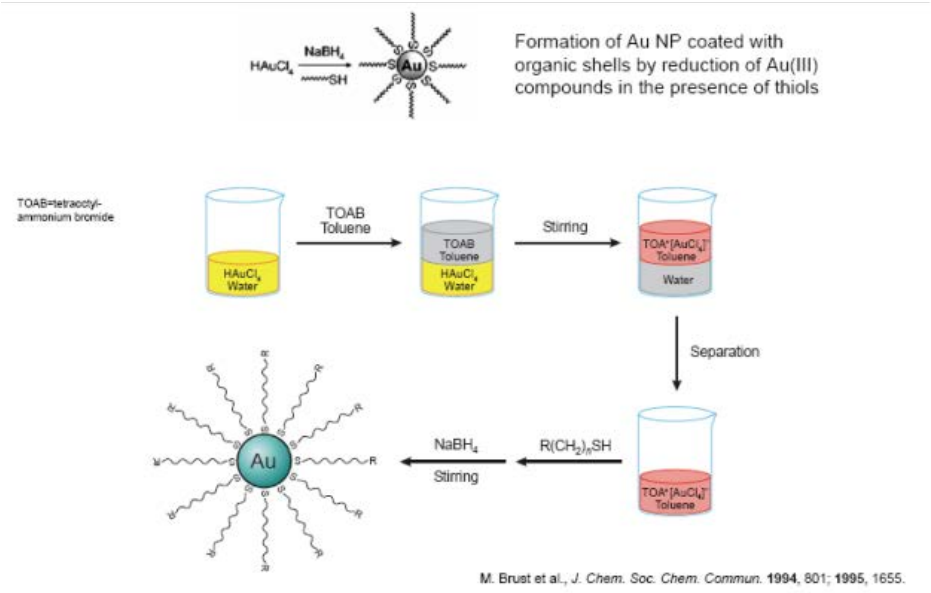

Figure1.6 General scheme for the ligand-exchange reaction between alkanethiol-Au_{NPs} of the Brust type and various functionalized thiols.[26]

The main problem of the *bottom-up* approach is however poor control of the nanoparticle dimensions due to the need to suitably arrest the growth of the nanoparticles at the required point. Both *Turkevich* and *Brust* syntheses afford stable gold nanoparticles by using simple molecules, but many efforts are still underway in order to find new syntheses that can permit size control in

nanoparticle formation.[33] The use of a surfactant, for example, allows stabilization of the nanoparticles by electrostatic bonding between gold surface and surfactant heads, followed by reverse micelle formation in a water-oil micro-emulsion, which acts like a template for nanoparticles formation.

Au_{NPs} can be also synthetized using *macromolecules, dendrimers,*[ii] *or polymers*[34] combined with a strong reducing agent. In general, the metal cation (Au^{3+}) interacts with the electronegative groups present in the system (polymers, macromolecules, or dendrimers), such as thiol, phosphine, amine, carboxyl, or carbonyl moieties. Some polymers and macromolecules have shown the capability to act directly both as reducing and stabilizing agents. In this case nanoparticles with big size are obtained, which may be unfavorable.[5] On the other hand, this synthetic route is important from a "green" and atom-economy point of view.

In the *Seed-growth method* nucleation and growth did not happen in the same process. By this technique the nanoparticles are enlarged step by step with an easier control of size and shape. According to a general procedure, a seed solution with small-size Au_{NPs} was introduced to a growth solution containing gold precursor, stabilizing agent and mild reducing agents. The reduction takes place only in the presence of the seed solution. In this way no new particle nucleation occurs and the newly reduced Au(0) grows around the seed surface to form Au_{NPs} of larger size. The process can be repeated to continue the growth. The final size is also influenced by the size of seed, amount and nature of reducing agent and stabilizer. The first seed-mediated growth gold nanoparticles were synthetized by Natan *et al*.[35] using citrate and capped spherical Au seeds (12 nm in diameter) into a growth solution containing a mild reducing agent such as citrate or hydroxylamine, obtaining Au_{NPs} between 20 - 100 nm. Besides spherical or quasi-spherical nanoparticles by using an additional structure-directing agent,[36] favoring the growth of Au(0) on some facets, lead to anisotropic Au_{NPs} structures such as nanorods, nanocubes, nanohexapods, nanopolyhedra. Murphy[37] and El Sayed[38] developed methods using hesadeciltrimethylammonium bromide (CTAB) to prepare gold nanorods. In these syntheses, experimental conditions, such as temperature, pH, gold precursor on gold seed ratio, can vary the size distribution and the shape of the nanorods. The synthetic tunability of nanorod structures and their strong absorption in the near-infrared light, [ii] where tissue absorption is minimal, make these materials very useful for potential *in vivo* applications. For this reason, nanorods and anisotropic structures in general found wide potential use in nanomedicine.[8,39]

[ii] Dendrimers are highly branched, cauliflower-shaped, monodispersed, synthetic macromolecules with well-defined composition, dimension, and structures.

[ii] Gold nanorods show two plasmon bands (Fig. 1.3, blue line): a strong longitudinal band in the near-infrared region and a weak transverse band, similar to that of gold nanospheres, in the visible region.

1.1.3 Mechanistic studies on Turkevich synthesis

Generation of spherical Au_{NPs} is commonly carried out by the citrate reduction method reported by Turkevitch in 1951.[25] By the use of only chloroauric acid $HAuCl_4$, sodium citrate, and water, Au_{NPs} of 15-20 nm can be obtained. Variations in temperature, gold-to-citrate ratio, order of addition, and reduction rate influence the final size of the nanoparticles.[40,41,42] For this reason, to understand the mechanism of the Au_{NPs} formation is a big challenge, whose rationalization could be however crucial to reach a complete control of the synthesis, so that a lot of research is still underway on this topic.

A general relation between the gold-to-citrate ratio and the final size of the particles[27] can be found in the work of Ji *et al*,[43] where the influence of pH (in turn dependent on the sodium citrate amount) on the reaction outcome is described. Two different mechanisms are suggested by monitoring the reaction by UV-Vis spectroscopy and TEM at different pH values. At pH lower than 6.5 the nucleation step is extremely rapid (< 10 s); this is followed by a step entailing coalescence of nuclei and formation of "fluffy" structures and, eventually, by an intra-particle ripening to form the final gold particles (pathway I, Fig. 1.7). At pH higher than 6.5, on the contrary, the nucleation time is longer (~60 s) and it is directly followed by a slow maturation (growth) of the nuclei to form gold nanoparticles (pathway II, Fig. 1.7).

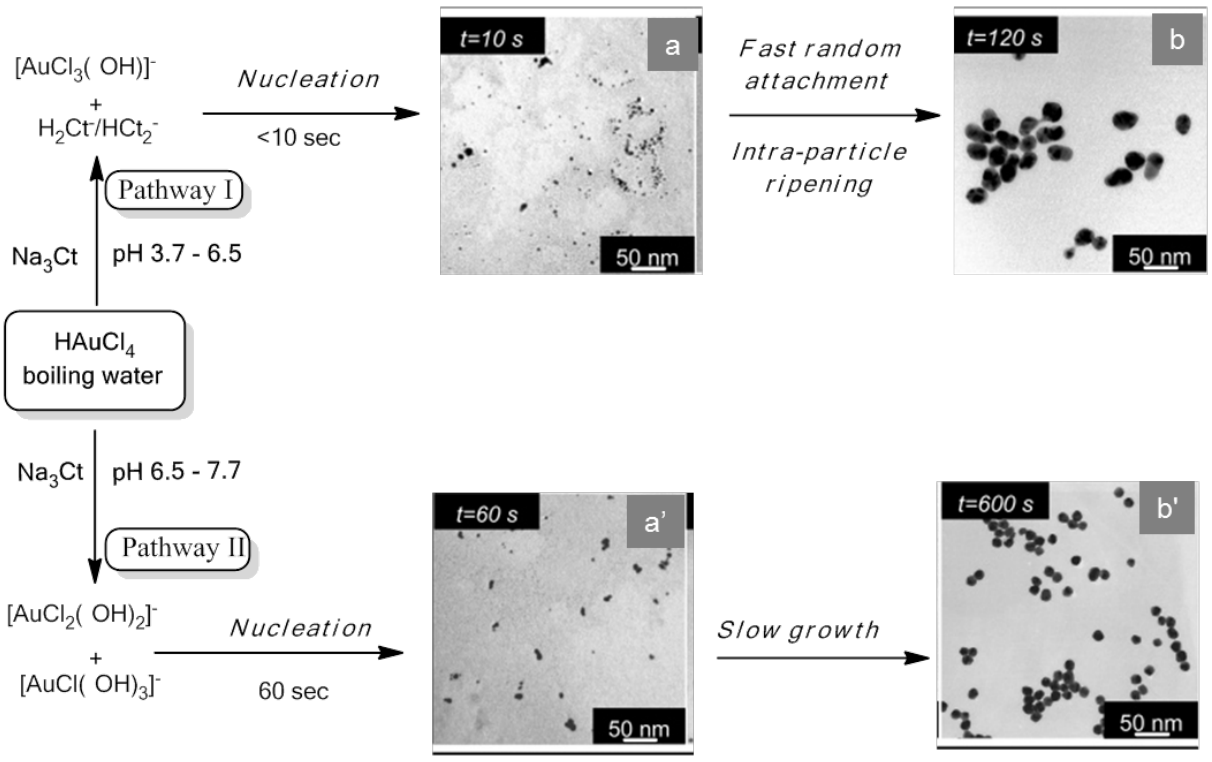

Figure 1.7 Temporal size/shape evolution by TEM using two different precursor ratios, with consequently different pH and mechanism (Ct = citrate).

Relying on TEM analysis, Rodriguez *et al* [44] have proposed another mechanism, suggesting that, during the nucleation and formation phases, the process began first with large agglomerates formation (100 nm), eventually followed by dispersion of these large systems, resulting in final 15 nm nanoparticles.

In their recent study Ojea-Jimenez *et al* [45] have proposed another pathway, based on experimental evidence and the existing literature,[46] in which the gold precursor $HAuCl_4$, after a ligand exchange reaction where a chloride is substituted by a citrate anion, is reduced to a Au(I) $[AuCl_2]^-$ species (Fig. 1.8), with eventually lead to Au(0) and thence to nuclei formation.

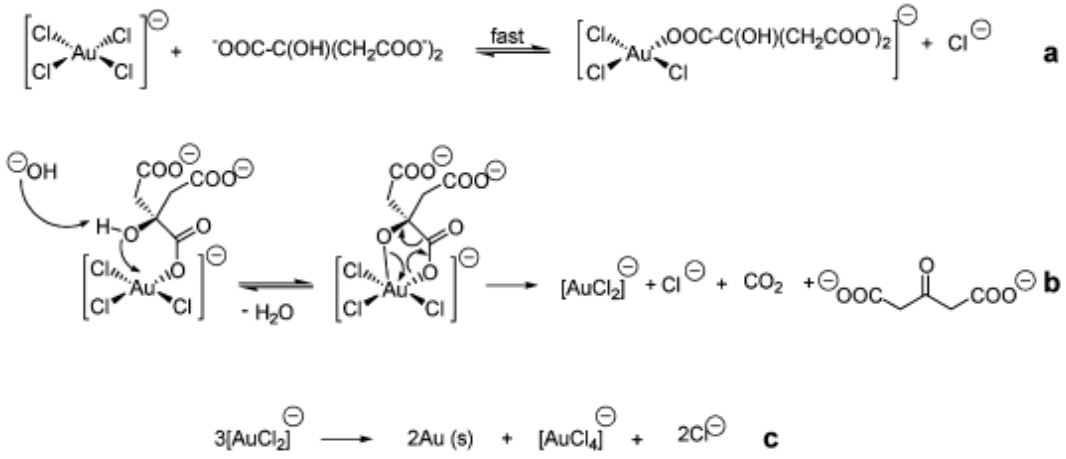

Figure1.8 (a) Ligand exchange reaction, **(b)** decarboxylation and reduction of Au(III) to Au(I) species, and **(c)** reduction of Au(I) to Au (0).

Synchrotron radiation related techniques can be useful to characterize the embryonic stage of the nucleation.[47] Indeed, Polte *et al.*[48] recently analyzed levitated sample droplets of Turkevich synthesis with small-angle X-ray scattering (SAXS)[iii] and X-ray absorption near-edge spectroscopy (XANES), employing synchrotron radiation to directly monitor precursor reduction and nanoparticle formation (Fig. 1.9). The synthesis was carried out under stirring in a flask immersed in a temperature-controlled water bath according to the Turkevich procedure. Liquid samples, ca. 4 μL each, were extracted from the batch solution by pipet for SAXS/XANES analyses at different reaction times and placed as droplets in an acoustic levitator, applied as sample holder for X-ray analysis. The acoustic levitator was used to prevent X-ray-induced reduction with metallic gold formation on the wall of the sample holder, such us in the case of Plech *et al.*[49]

[iii] SAXS is used for the determination of the microscale or nanoscale structure of particle systems in terms of such parameters as averaged particle sizes, shapes, distribution, and surface-to-volume ratio.

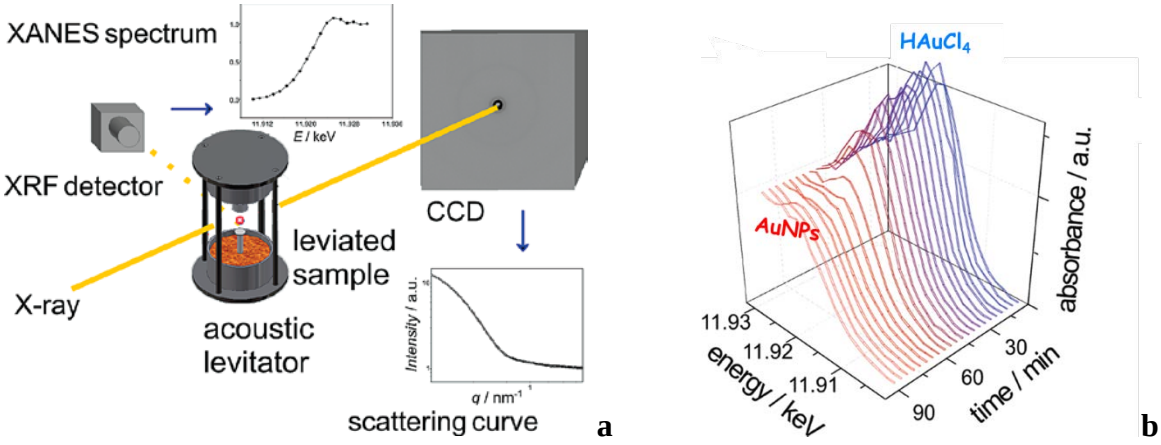

Figure 1.9 a) Schematic representation of the experimental setup employed for SAXS and XANES analyses on droplets of the reaction solution during Au_{NPs} formation; **b)** Series of XANES spectra recorded during Au_{NPs} synthesis. The diminishing of the pre-edge peak indicates reduction of Au(III) to Au(0).

The experimental evidence derived from *in situ* XANES and SAXS experiments revealed different phases of nanoparticle formation Fig. 1.9, panel **b**, and Fig. 1.10. The initial phase (first 60 s) starts with a rapid nucleation process, during which about 20% of the gold precursor is transformed into nuclei or particles. Those particles initially show a mean radius of 2 nm and, in about 20 min, they merge and aggregate to particles with a mean radius of 4 nm. This step is accompanied by a slow reduction process, as proven by the consumption of Au(III). In a second growth phase, taking place between 25 and 50 min, SAXS data indicate that particles grow continuously to a mean radius of 5.5 nm and the polydispersity decreases down to 14%, whereas the number of particles remains almost constant. This implies that metallic gold is growing onto the particles by diffusional growth but, because of the low reduction rate, chemical reduction of the gold precursor becomes the limiting factor and consequently determines the nanoparticles growth rate. The third phase (50-70 min) includes rapid consumption of the remaining Au(III) species (ca. 70%), accompanied by an increase in the particle size and a further decrease of polydispersity to 10%, resulting in a final Au_{NPs} mean radius of 7.7 nm. The accelerated consumption of Au(III) observed after 50 min and with a Au_{NPs} radius of about 5 nm could be attributed to an autocatalytic reduction on the surface of the formed nanoparticles.

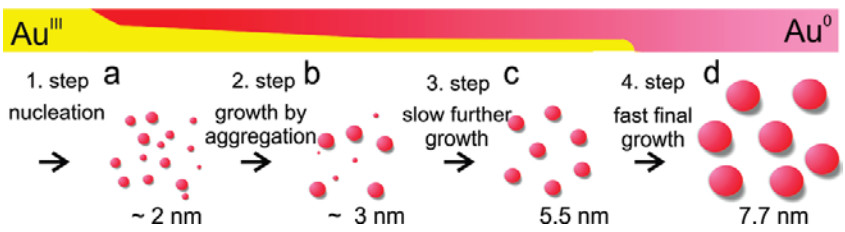

Figure1.10 Schematic illustration for the suggested process of gold nanoparticle formation.

From all the above mentioned works, it can be noted that different mechanisms describing the synthesis of gold nanoparticles in the presence of sodium citrate can occur depending on the experimental conditions (temperature, concentration, etc.), which may favor one pathway at the expense of another. In this scenario, it can be stated that the mechanisms of gold nanoparticles formation in the Turkevich synthesis is not known with certainty, difficulties coming from the relative short time scale of the nucleation and growth step and the limited accessibility to *in situ* time-resolved characterization.

1.1.4 Turkevich synthesis by a microfluidic set-up

Continuous flow microfluidic systems show particular promise in controlling shape and size distribution of synthesized micro- and nanoparticles.[50] Microfluidics is the science and technology of systems that process or manipulate small (10^{-9} to 10^{-18} litres) amounts of fluids, using channels with dimensions of tens to hundreds of micrometres. These technologies are in rapid development, offering a solution to improve the control of the reaction parameters with a faster heat transfer and mixing, as a result of the increased surface area-to-volume ratio of the system. The first nanoparticle synthesis in a microsystem was reported by Wagner et al. who studied the growth of gold nanoparticle seeds in a glass micro-channel reactor at room temperature.[51]

Girardon et al.[52] recently reported fine tuning of the gold nanoparticle size by the transposition of Turkevich's classic gold nanoparticle synthesis under continuous flow conditions. The microfluidic reactor, made from commercially available items, permitted short mixing, heating, and quenching times, which are the key parameters of this synthesis (Fig. 1.11)

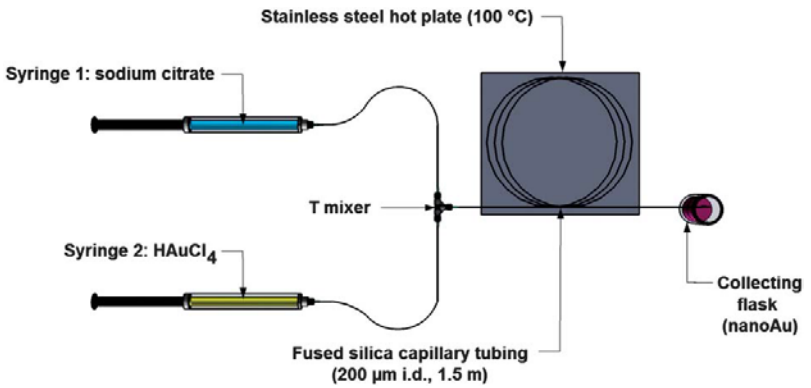

Figure1.11 Two syringes, one containing $HAuCl_4$ (5.4×10^{-3} M) and the other a sodium citrate solution (16.3×10^{-3} M), were connected by a 15 cm long silica capillary to a "T" micro-mixer connector in order to mix the reagents (driven by syringes pumps, not shown in the picture) into a coiled silica capillary of 1.5 m. The capillary, with an inner diameter of 200 µm, was positioned on a hot plate (100 °C).

1.2 Supported Gold Nanoparticles

1.2.1 Synthesis of heterogeneous gold catalysts

Catalysis drives many reactions due to the ability to lower their activation energy, hence increasing reaction rate and yield of the desired products. The use of nanoparticles as catalysts has become more and more widespread as nanoparticle properties and reactions were better understood. The possibility of using less amount of material and of tuning the catalyst properties by modelling the different shapes and sizes of nanoparticles is a very attractive feature of these systems. A well indepth state-of-the-art description of nanocatalysis has been reported in a recent review.[53]

Nanoparticle catalysis has been investigated for both homogeneous (catalyst and reactants are both in solution) and heterogeneous (catalyst are supported on an insoluble substrate) systems, but in general the use of a supported material facilitates catalyst recycling and hence reduce the required amount of metal. The primary role of the support, as for the stabilizing agents (ligands) with gold colloids, is to avoid aggregation and agglomeration, although the support features (such as surface area, density of defects, and presence of hydroxyl groups on the surface) can also have a direct or indirect role in the catalytic activity (Fig. 1.12).

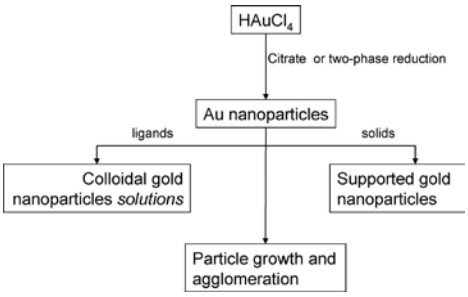

Figure1.12 Strategies to stabilize gold nanoparticles against agglomeration.[53]

Supports used in catalysis are in general mesoporous oxides (TiO_2, CeO_2, SiO_2, Fe_3O_4, Al_2O_3, ZrO_2) and different carbon structures.

Heterogeneous catalysts are generally prepared by either direct adsorption of the gold precursor on the support followed by reduction, or addition of pre-formed gold nanoparticles onto the support. In the former case two different methods are available: *adsorption* and *deposition–precipitation*. In both techniques the most important parameters are the pH of the starting aqueous solution of the dissolved gold salt and the isoelectric point of the support (the pH at which the surface is zero-charged, IEP). Indeed, at pH values over or below the isoelectric point the surface

becomes positively or negatively charged, respectively. This value allows classification of the materials into acidic or basic.

In the *adsorption* method the interactions between the gold species in solution (products of the hydrolysis of $HAuCl_4$ in water [$Au(OH)_xCl_{4-x}$]) and the charged surface of the materials bring to the Au anion spontaneous adsorption. This method is generally used for TiO_2 (with IEP = 6) that at pH below 6 is positively charged and absorbs through columbic interaction anions such as [$AuCl_4^-$] or [$AuCl_3(OH)^-$]. It has been also reported that 60% of $HAuCl_4$ solution can be absorbed on titania at pH = 3, when the predominant species is [$AuCl_3(OH)^-$]. In fact, one possibility is that the initial interaction between the gold species and the support surface is more favourable for hydrolysis species having Au-OH groups than Au-Cl. Some studies reported in the literature[54,55] suggest that the absorption of the gold hydrochlorides is not purely a columbic interaction with the support but also involves formation of covalent bonds with the solid surface by reaction with hydroxyl groups. After attachment onto the surface, the gold precursor is reduced by addition of a reducing agent and the formation of the nanoparticles is believed to occur in two steps, involving nucleation and growth. Once the gold atoms are being organized in small nuclei, where the aurophilicity of gold to form Au-Au bonds will play a significative role, growth will occur to form the eventual nanoparticles. Concentration and the presence of chloride ions are the many parameter that can affect the growth.

The *deposition-precipitation* method was first used by the Haruta's group and since then it has been the most used method for preparation of gold catalyst. Here, the [$AuCl_4^-$] anion is hydrolysed by raising the pH of the solution to form insoluble $Au(OH)_3$, which becomes absorbed on the surface as a precipitate.[56,57] Haruta has suggested that precipitation of $Au(OH)_3$ takes place exclusively on surface defects that act as nucleating sites. After absorption on the solid, gold nanoparticles formation occurs by nucleation and growth, as indicated before, and the final size of Au_{NPs} are influenced by gold loading, the nature of the solid surface, the presence of chloride ions, and thermal treatments. Thermal treatments are generally avoided in the adsorption method, since they hinder removal of chloride ions, made possible by exhaustive washing and hydrogen stream treatments. In the deposition-precipitation method, working at high pH values, the amount of chloride ions is reduced by favouring deposition of species substituted more with the OH ligand rather than Cl^-; the resulting nanoparticles have an average size generally smaller than those obtained with the *absorption* method.

In the *deposition-precipitation* methods the nature of support plays an important role, and indeed the procedure is applicable only on metal oxides having high IEP, such as TiO_2, Fe_2O_3, Al_2O_3, ZrO_2, and CeO_2. In materials with low isoelectric points, such as SiO_2 (IEP $\cong$ 2), the

deposition precipitation method is not recommended; in fact, under the high pH conditions required in this method, the weak interactions between the negatively charged silica and the $[Au(OH)_nCl_{4-n}]^-$ species hinder gold absorption and facilitate mobility of Au_{NPs}. Preparation of silica supported gold nanoparticles generally involves the use of other methods, such as modification of the surface with organic groups by post-grafting or co-condensation (described in more details in paragraph 1.1.2), chemical vapour deposition, absorption of preformed nanoparticles (colloidal solution protected by ligand or polymers), or modification of the surface with inorganic additives (TiO_2, Al_2O_3, CeO_2).

Absorption of preformed nanoparticles, in particular, is generally used for materials where the deposition-precipitation method is difficult to perform: besides metal oxides with low isoelectric points, this is the case of carbon supports, where the hydrophobic nature of carbons and the low density of surface hydroxyl groups brings to large aggregates of gold. Anyway, gold nanoparticles supported on active carbon are among the most used catalysts in oxidation and hydrogenation reactions. The nanoparticles used are generally colloidal solution protected by particular ligands, polymers, dendrimers, or macromolecules, or obtained by chemical vapour deposition and sonochemical or photochemical irradiation.

This technique also offers the advantage to support gold nanoparticles suitable for homogenous catalysis simplifying the catalyst recovery and improving the surface area and mechanical strength of dendrimers and polymers.[58,59,60] For example, *Corma et al*. dispersed chitosan, an abundant biopolymer, on the silica surface to stabilize gold nanoparticles by means of its nitrogen and oxygen groups (Fig.1.13). The Au_{NPs} (4-6 nm) were obtained by impregnation of the composite material with the gold precursor, followed by spontaneous thermally promoted reduction.[58]

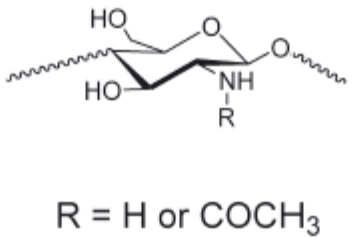

Figure 1.13 Glucosamine building unit of the natural chitosan polymer.

1.2.2 Reduction of aromatic nitro compounds

In recent times, there has been an impressively growing interest towards chemical transformations achieved by "green" processes,[61] procedures involving non toxic reagents and

solvents (the latter often substituted with water) and mild reaction conditions (e.g. ambient temperature and pressure, so that energy consumption is lowered as much as possible). Organic nitro compounds are very common chemicals, usually toxic for the environment, generated as by-products in different industrial processes leading to agrochemicals, dyes, and drugs. Among them, 4-nitrophenol (4-NP) is one of the most frequently occurring products. In pharmaceutical industries, it is usually employed as a starting material for production of 4-aminophenol (4-AP) (Scheme 1.1). The latter is in turn an important building block for the synthesis of different analgesics and drugs, among which paracetamol, obtained by treatment of 4-AP with acetic anhydride. (Scheme 1.2).

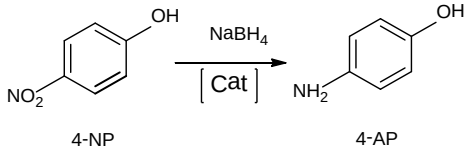

Scheme 1.1 Synthesis of 4-AP by 4-NP reduction by the use of a catalyst and $NaBH_4$.

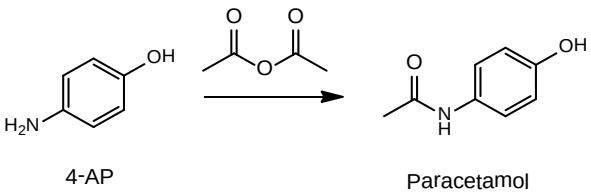

Scheme 1.2 By treatment of 4-AP with acetic anidrhyde paracetamol is obtained.

In the majority of cases, the reduction of 4-NP to 4-AP occurs by use of a metal (generally iron) under acid conditions. The main disadvantage of this reduction process is however the generation of large amounts of iron-oxide sludge (1.2 kg of FeO sludge/kg product), which is related to great environmental hazards.

As a viable alternative, 4-NP can be converted into 4-AP via a metal-nanoparticle-catalyzed reduction of 4-nitrophenol with $NaBH_4$. This procedure has already replaced the previous ones due to its straightforwardness and environmental friendship. It has also become a "model" reaction since it is extremely simple to follow by UV-Vis spectroscopy. In fact, the 4-NP solution exhibits a strong absorption peak at 317 nm under neutral or acidic conditions; upon addition of $NaBH_4$, the absorption peak shifts to 400 nm, which corresponds to a color change from light-yellow to yellow-green, due to the formation of 4-nitrophenolate; addition of the catalyst (the reaction does not occur with $NaBH_4$ alone) brings about disappearance of that peak in favour of that of 4-aminophenolate (Fig. 1.14).

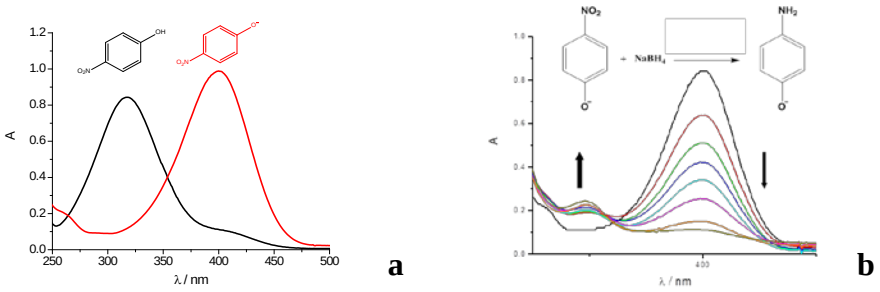

Figure1.14 a) UV-Vis spectra of 4-NP before (black line) and after (red line) addition of $NaBH_4$ solution; **b)** UV-Vis spectra of 4-NP reduction in the presence of excess $NaBH_4$ and a catalyst.

In literature there are several examples of 4-NP reduction with $NaBH_4$ in the presence of various catalysts. The kinetic constants generally obtained for gold-nanoparticles-based systems are of the order of magnitude of 10^{-3} s^{-1}, with a pseudo first order kinetic law. Additional kinetics details on this reaction will be furnished in the experimental part of Chapter 2 and Chapter 4.

1.3 Silica Nanoparticles

Silica is an attractive material due to its large abundance, stability, commercial availability, low cost, and ease of processing, and it find diffuse application in technological fields such as optical devises, catalysts, filler for polymers, and so on.[62] Silica gels are common in nature (opals and agates) and can be obtained synthetically. There are many synthesis available, but in general monodispersed systems are formed from controlled homogenous nucleation processes, which are analogous to the process used to form metal oxides from the controlled hydrolysis of metal salts in aqueous solutions.

The synthesis of colloidal silica by hydrolysis of tetraethoxysilane (or tetraethylorthosilicate, TEOS) in alchols has been widely studied. This alkoxide is of great interest in the synthesis of silicate glasses and ceramic powders. The overall reaction consists first in hydrolysis of the silicon alkoxide to a silanol (Scheme 1.3), followed by a condensation step of the dispersed-phase materials (Scheme 1.4). Since the hydrolysis with water alone is very slow, either an acid or a base is normally added as a catalyst, where the kind of catalyst influences the final system structure. Generally, the use of an acid encourages growth of gel structures in the subsequent condensation, while the use of a base, such as ammonia or NaOH, affords spherical particles (like in the Stöber synthesis).

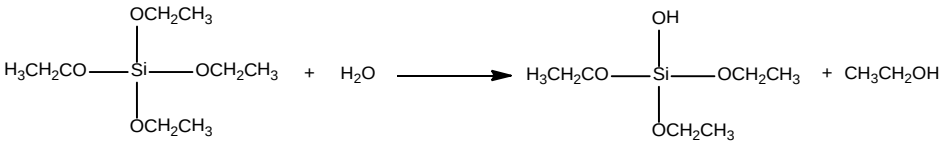

Scheme 1.3 Hydrolysis of silicon alkoxide with formation of silanol species.

Hydrolysis of the silanol can continue further by condensation reactions of two silanols (or a silanol plus an alkoxide), resulting in a bridging oxygen that links two silicon atoms together (Scheme 1.4).

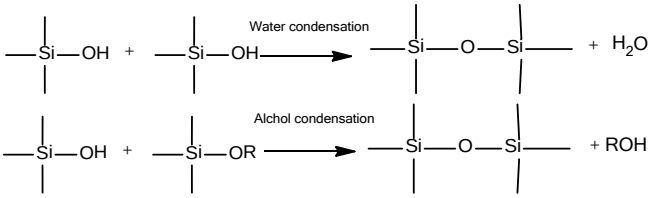

Scheme 1.4 Condensation reactions of silanols with loss of one molecule of water or alcohol.

Further hydrolysis and condensation reactions continue to afford a silicon-based polymer chain. In solution, these reactions begin simultaneously at many different locations leading to the formation of numerous growing silicon oxide/alkoxide particles. The mechanisms of hydrolysis and condensation reactions of silicon alkoxides involve bimolecular nucleophilic substitution reactions that can occur under either acid- or base-catalyzed conditions. Under acid-catalyzed conditions, the rate of hydrolysis is slow compared to the rate of condensation, which leads to longer polymer chains in the sol that continue to grow and entangle, with formation of gel. In contrast, under base-catalyzed conditions, hydrolysis occurs rapidly (only the first ethoxy-group substitution is slow), resulting in more highly branched clusters in the sol that do not readily interpenetrate but link up like a pearl necklace at the gelation point.[63,64]

In the Stöber synthesis, the ammonia-catalyzed reactions of TEOS with water in low molecular weight alcohols produce highly monodisperse spherical silica nanoparticles with a size range from 6 to 2000 nm. [65] In his work, Stöber made a systematic investigation on the influence of different experimental parameters, such as concentrations of water, ammonia, and TEOS, on the final size of the silica particles. He showed that the condensation rate depends strongly upon the water and ammonia content, noting that an increase in ammonia concentration brings to larger particle formation. In the absence of ammonia the silica flocculated in irregularly shaped particles and no spheres could be observed. Hence, ammonia influence the spherical shape of the particles, as shown in the TEM micrograph reported in Fig 1.15.

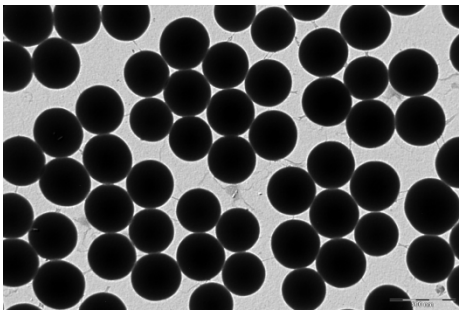

Figure 1.15 TEM micrograph of silica nanoparticles, obtained by the Stöber's method, with an average size of 360 nm ±15 nm.

1.3.1 Functionalization of silica nanoparticles

The Stöber synthesis finds application in many techniques; this synthesis can be tailored as to cover different kinds of nanoparticles, such as gold and[66] iron or cobalt[67] oxide, with a silica layer, but can also be used as a direct method to obtain silica-functionalized nanoparticles by simply adding a suitably substituted alkoxysilan, bearing incondensable units, to the mixture of TEOS and ammonia.

Generally speaking, there are two basic approaches for the covalent introduction of chemical functionalities to silica NPs: surface silanization and co-condensation methods. The *silanization* method (grafting) was first reported in 1989 by Philipse and Vrij[68] and it is now frequently used in various fields of chemistry. The possibility of introducing chemical functionalities to silica NPs by *co-condensation* of TEOS with an appropriate organosilane, yielding stable hybrid organo-silica NPs, was instead first reported in 1993 by Van Blaaderen and Vrij; by this method a huge variety of chemical functionalities can be introduced on the silica surface, leading in general to a homogenous distribution of the organic functionalities, such as amine,[69] fluorescent dyes,[70] carbazole,[71] and alkyne[72] moieties, onto the silica nanoparticles.

Both silanization (grafting) and co-condensation methods are widely used techniques to prepare gold catalyst onto a silica support, in particular by grafting to the silica surface functionalities which possess big affinity for gold (thiols, amines), such as to avoid mobility and aggregation of the nanoparticles. In the grafting technique the silica surface is modified by adding the suitably functionalized organosilane species to a refluxing mixture of silica NPs in toluene or ethanol (Scheme 1.7). The resulting modified silica is then dispersed in a solution of the gold precursor, as to allow absorption of the gold species onto the silica surface by ion-exchange and subsequent reduction either by thermic treatments or by adding a $NaBH_4$ solution.[73]

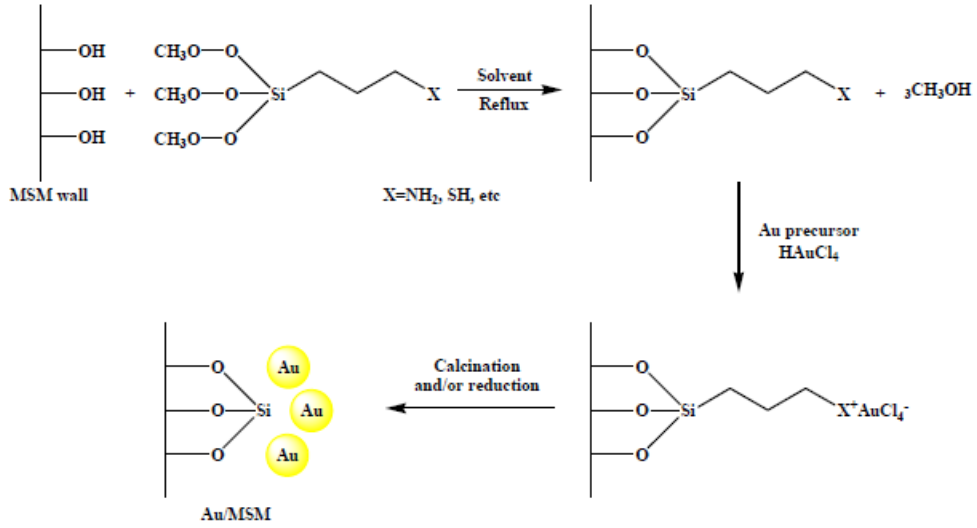

Scheme 1.5 General procedure for the synthesis of silica supported gold catalysts by post-synthetic functionalization before gold loading.[73]

The co-condensation method, also called self-assembly functionalization, use the co-condensation of TEOS with other silanes containing suitable organic functional groups in order to functionalized the surface with positively charged groups (Scheme 1.8). Gold is introduced in a subsequent step, mainly by a deposition-precipitation method using $HAuCl_4$ and reduction by a thermic treatment.

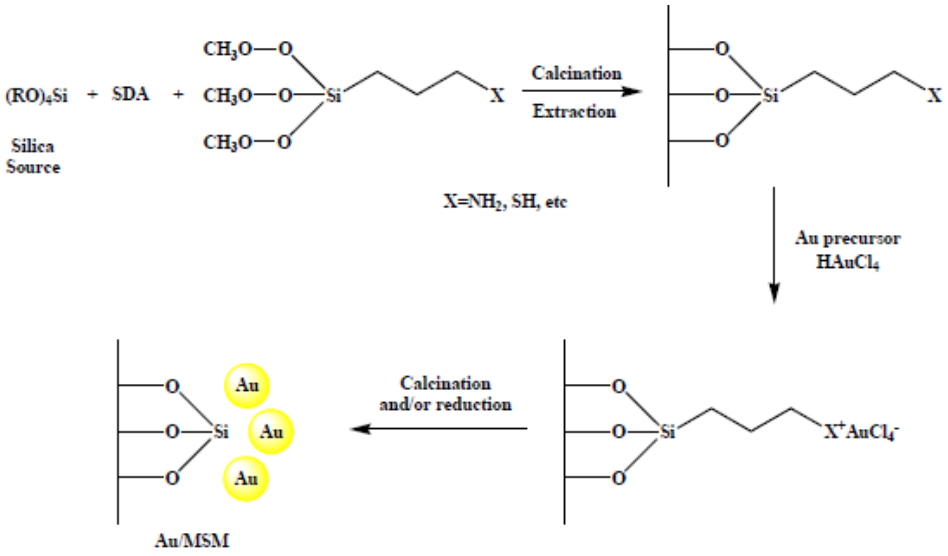

Scheme 1.6 General procedure to prepare gold catalysts by co-condensation method.

1.4 Thiol-yne reaction

With the term "click chemistry" we refer today to a crucial branch of chemistry that is slightly more than one decade old but it is getting more and more importance for its safety, environmental, and hence "green" consequences. It is generally recognized that the "click chemistry realm" was founded by the turn of the century by Sharpless, [74] who established a series of characteristics that make chemical reactions "click processes": these include orthogonality with other common synthetic procedures (definitely one of the most notable aspects), very mild reaction conditions, use of benign catalysts and solvents, high reaction rates, insensitivity to water and (often) oxygen, complete regio- and stereo-selectivity (if required), ready availability of reagents, ease of workup, and high yields. Altogether, "click reactions" are hence very simple procedures (something like putting together two Lego bricks) that can be conducted under very straightforward, safe, and atom-economy conditions. It is worth noting that the realm of click chemistry does not contain at all "exotic" syntheses: on the contrary, it is full of "historic" reactions that were simply brought to a new life by recognizing their so far underesteemed value. Among click reactions we therefore can find the Cu-catalysed azide-alkyne cycloaddition (CuAAC), probably the most popular one, but also a couple of very old radical reactions such as addition of thiols to alkenes and alkynes. The latter reactions are of particular importance since they does not need any potentially toxic metal catalyst (contrary to the CuAAC coupling) and can therefore be conveniently used not only for material derivatization[75] (a field that is becoming of crucial significance), but also in those arenas where biotoxicity could be an important issue, i.e. in bioconjugation.[76]

Radical thiol–yne coupling (the thermally or photochemically induced radical addition of thiols to alkyne, TYC) has recently emerged as one of the most attractive click chemistry procedures.[77],[78] Like any radical thiols addition the reaction entails three steps including initiation, propagation and termination. Scheme 1.9 shows the radical chain mechanism in the TYC reaction. H-abstraction from thiols in the presence of thermal/photochemical initiators (such as peroxides, or irradiation with UV light in the presence of photosensitizers) give sulfanyl radicals. Addition of a sulfanyl radical to C≡C triple bond gives a β-sulfanyl-vinyl radical (propagation) that readily abstracts hydrogen from the thiol to regenerate the chain (termination) with concomitant formation of a sulfur-radical intermediate and the vinyl sulfide monoadduct (TYC chain). Under certain conditions this mono-adduct can react with another sulfanyl radical to give an α,β-disulfanyl-alkyl radical that can subsequently abstract hydrogen from the thiol to give the final bis-sulfide bis-adduct (TEC – Thiol-Ene-Coupling – chain). Unlike the primary vinyl radical, the successive alkyl-

counterpart occurs in a reversible fashion: this allows for properly tuning reaction conditions in order to favour formation of the bis-addut (TYC-TEC sequence) or mono-adduct (TYC).

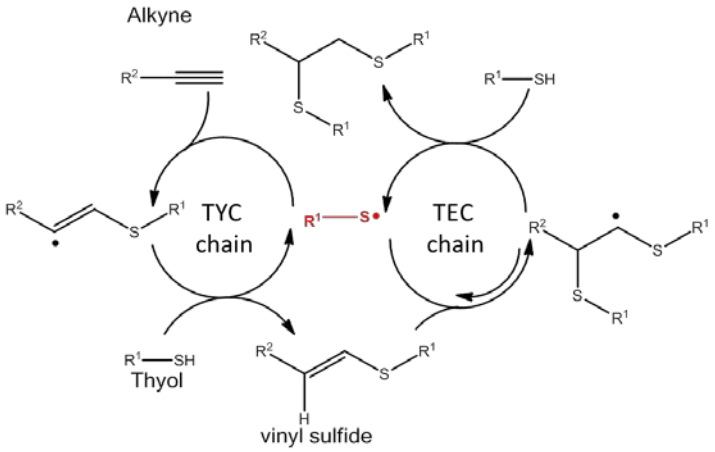

Scheme 1.7 Mechanism of TYC and TEC radical chains.

The experimental conditions plays indeed an important role on this reaction: factors such as thiol-alkyne molar ratio, temperature, solvent and a proper choice of them all can bring to TYC or TYC/TEC chains, with the possibility to perform sequential radical chains with formation of non-symmetric bis-disulfide products, an important tool in bio-conjugations.[77a]

In the realm of materials science, however, the usual attractive target is to obtain highly functionalized materials (e.g. hyperbranched polymers/dendrimers) and the reaction is normally carried out by adding two equivalents of the same thiol to the alkyne of interest (TYC-TEC homosequence), so that the reaction does not stop to the vinyl sulfide step. Concentration is however very important even in this kind of reaction, since high dilutions might result in appreciable side reactions, for example dimerisation of sulfanyl radicals to give the corresponding disulfide. In recent times many articles on this click process can be found in the literature and application range from supramolecular chemistry to surface modifications, from post-polymerization techniques to nanoparticles functionalization.[77]

The use of TYC in the field of gold nanoparticles is a novelty: in the literature we could find only one paper[79] dealing with that topic, particularly with grafting of polymeric monolytes (Fig. 1.16) with alkyne groups and then their functionalization with primary-amine- and sulfide-moiety containing branches, capable of trapping preformed gold nanoparticles. In that example, bis-cysteamine addition onto the alkyne units is assumed to be the only reaction mechanism and no occurrence of vinyl sulfide moieties was observed. No examples of this procedure were found in the literature involving silica-based systems.

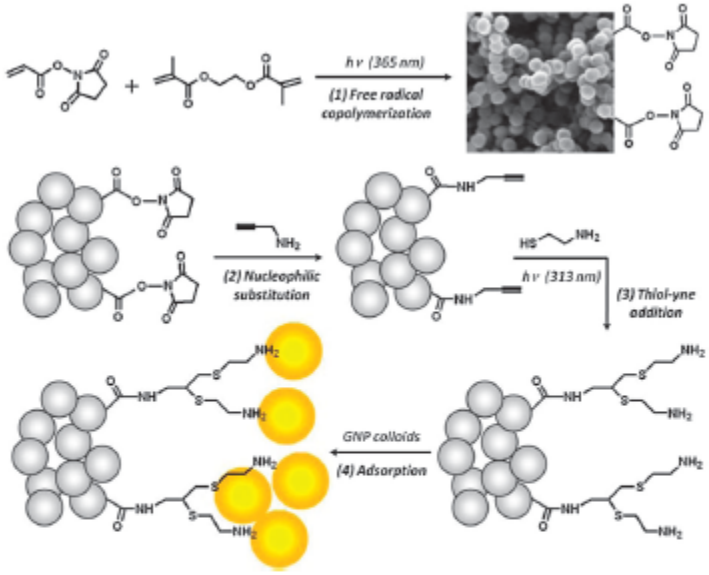

Figure 1.16 Reaction scheme for the surface immobilization of Au_{NPs} (yellow balls) on functionalized poly(NAS-co-EDMA).

1.5 Characterization Techniques

Characterization of the supported gold nanoparticles requires combination of different techniques, each of them providing specific information that complements the data obtained from the others. TEM analysis allows determining the shape and particles size distribution and their location; XAS analysis serve to establish the oxidation number and geometry environment of the nanoparticles; FT-IR and XPS analysis serve to establish the Au oxidation states and the strength of the interaction with probe molecules.

1.5.1 X-ray absorption spectroscopy (XAS)

X-ray absorption spectroscopy (XAS) is an element specific spectroscopy sensitive to the local chemical and structural order of the absorber element. XAS is nowadays increasingly used for the speciation analysis of chemical elements owing to the development of new synchrotron radiation facilities worldwide. This technique, in fact, requires an intense, polychromatic source and for this reason the synchrotron radiation (SR), which is an electromagnetic field radiated by relativistic accelerated charged particles (electron in general), can be conveniently used. When the trajectory is subject to a steady acceleration perpendicular to its velocity, as is the case of a bending magnet,radiation is emitted tangentially along the particle's trajectory (Fig. 1. 17).[80] This radiation is indeed extremely intense over a broad range of wavelengths extending from the infrared through visible light and ultraviolet into the soft and hard X-rays of the electromagnetic spectrum.[81]

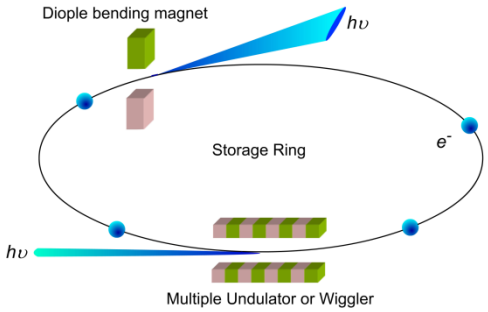

Figure 1.17 A schematic diagram of a synchrotron radiation accelerator. hν: photon source, e^-: electrons.

The main advantages of the XAS method are its subatomic (angstrom) resolution, the ability to analyse almost any type of samples including amorphous (non-crystalline) materials, and the possibility to analyse such materials *in situ* requiring minor or no sample preparation.

A general experimental set-up of the optics and instrumentation used in XAS is shown in Fig. 1.18. A monochromator is used to select and vary the incident energy around the threshold energy of the probed element (11919 eV in the case of Gold). A double crystal monochromator is commonly used to keep the beam propagating parallel to the initial direction following two reflections. Usually XAS beamlines are installed on a bending magnet which provides a divergent flux. Thus, to increase the photon flux on the sample and decrease the beam size, the second crystal of the monochromator is usually cylindrical in order to perform a dynamic sagittal focalization of the beam on the sample. The higher harmonic reflections are suppressed by the reflection on 2 curved mirrors on either side of the monochromator which are also used to collimate the X-ray beam on the monochromator (1^{st} mirror) and to focus it on the sample (2^{nd} mirror). The beam size can be controlled in between 0.1 and 1 mm, depending on the size of the sample.

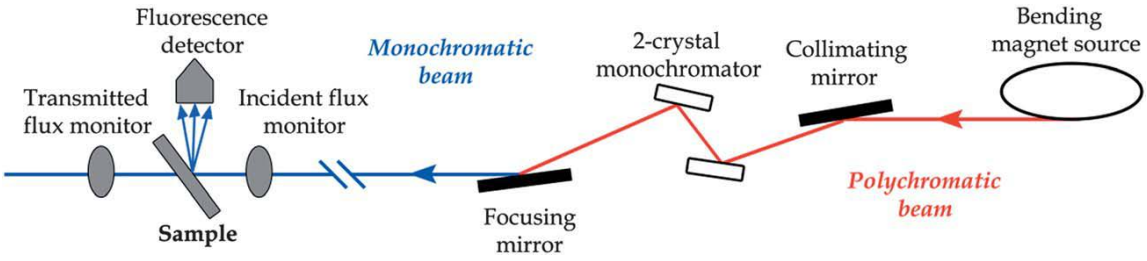

Figure 1.18 Sketch of a generic X-ray absorption experiment using synchrotron radiation.

In a standard XAS experiment in transmission mode (in general for concentrated samples) the linear absorption coefficient μ(E), conventionally in cm^{-1}, varies with the sample thickness (x) and is determined according to the Lambert–Beer law,

$$\mu(E)x = \ln(I_0/I_1) \quad (1.1)$$

by measuring the incident (I_0) and transmitted X-ray flux (I_1) with two different intensity monitors, usually ion chambers. In the case of diluted system (in the order of 100 μg g^{-1}, resulting in weak X-ray absorption in transmission) the data collection is carried out in fluorescence mode by using an X-ray detector positioned at 90° respect to the incoming beam (Fig. 1.18). In this case, for a diluted sample, the absorption coefficient is measured as a function of the fluorescence yield normalized by I_0, where I_f is the detected intensity of a fluorescence line associated with the absorption process.

$$(E) = I_f/I_0 \quad (1.2)$$

The XAS technique measures the variations of μ(E) by scanning the incident beam energy E (Fig. 1.19). When an incident monochromatic X-ray beam impinging on a sample is scanned in energy, one can observe an abrupt increase in the measured absorption coefficient, the so-called *absorption edge* (or white line) of the element. This corresponds to X-rays that have sufficient energy to eject a core electron from an atom via the photo-electric effect. Each electron has a well-defined binding energy for which corresponding absorption edges are observed (K, L, M. edges).[82]

XAS spectra can be divided into *X-ray absorption near edge structure* (XANES), providing information about oxidation state and molecular geometry, and *extended X-ray absorption fine structure* (EXAFS), providing structural information about metal site ligation, i.e. type of neighbouring atoms, coordination numbers, and bond distances (Fig. 1.19). The molecular order information is given mostly by the EXAFS oscillations after the edge. Indeed, it is seen from theory that EXAFS oscillations come from the interferences between the outgoing photoelectron waves from the absorbing atom and the backscattered photoelectron waves from the neighbouring atoms.
In this technique when an incident monochromatic X-ray beam impinging on a sample is scanned in energy, one can observe an abrupt increase in the measured absorption coefficient, the so-called *absorption edge* (or white line) of the element.

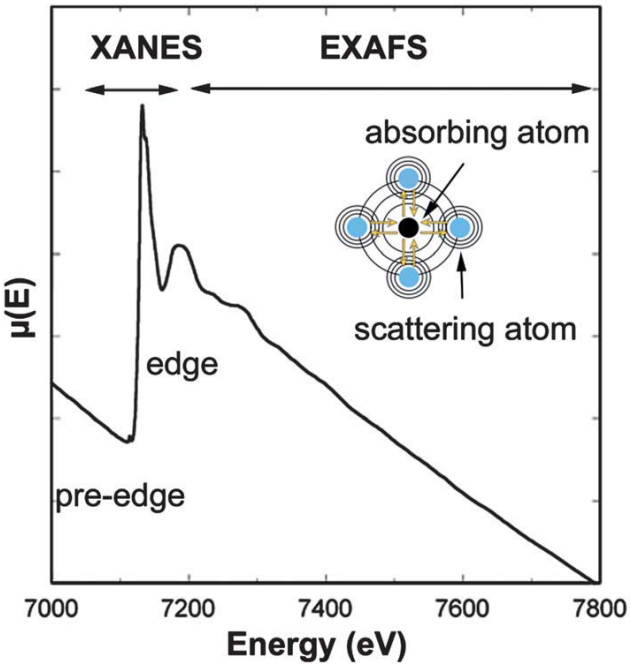

Figure 1.19 Variation of the linear absorption coefficient μ(E) as a function of the incident X-ray energy.

1.5.2 X-ray photoelectron spectroscopy (XPS)

Photoelectron spectroscopy (XPS) is a technique that can produce *in situ* chemical state information without almost any sample preparation, similarly to XAS. In XPS, the sample is irradiated with low-energy X-rays in order to trigger the photoelectric effect, and the energy spectrum of the emitted photoelectrons is determined by means of a high-resolution electron spectrometer. XPS is a surface analysis method limited to the first 10 nm of the sample. By this technique we obtained useful information about composition of our materials.

Figure 1.20 AXIS Ultra XPS Instrument.

The system (Fig.1.20) is made of:

i) a source of X-rays;

ii) an ultra-high vacuum (UHV) stainless steel chamber with UHV pumps (the technique requires ultra-high vacuum conditions);

iii) an electron collection lens;

iv) an electron energy analyzer;

v) metal (nickel-iron alloy) magnetic field shielding;

vi) an electron detector system;

vii) a moderate vacuum sample introduction chamber;

vii) sample mounts;

viii) a sample stage;

ix) a set of stage manipulators.

X-Rays irradiate the sample surface, hitting the core electrons of the atoms and penetrating the sample to a depth of the order of magnitude of a micrometer. Useful electron signal is obtained only from a depth of around 10 to 100 Å on the surface. The instrument uses different pump systems to reach the goal of an ultra-high vacuum. The X-Ray source produces photons with certain energies: MgKα photon with energy of 1253.6 eV or AlKα photon with energy of 1486.6 eV. Normally, the sample will be radiated with photons of a single energy (MgKα or AlKα). The core electrons are close to the nucleus and have binding energies characteristic of their particular element. They have a higher probability of matching the energies of AlKα and MgKα. The Binding Energy (BE) is characteristic of the core electrons for each element. The BE is determined by the attraction of the electrons to the nucleus. If an electron with energy x is pulled away from the nucleus, the attraction between the electron and the nucleus decreases and the BE decreases. Eventually, there will be a point when the electron will be free of the nucleus.

1.5.3 XRF spectrometers

A spectrometer at wavelength dispersive systems (WDXRF)XRF technique has been used to measure the amount of gold on silica. The XRF spectroscopy consists in irradiation of the sample with X-rays: the incident radiation leads to expulsion of an electron from an inner shell, creating an electronic vacancy. When an electron of the outer shells fills that vacancy the energy surplus is emitted as an X-ray photon, with a characteristic energy, specific for each elements, that is related to the involved electronic shells.

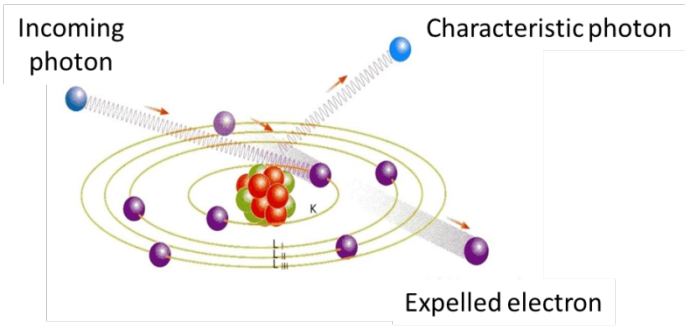

Figure 1.21 XRF production of a characteristic radiation.

X-ray fluorescence is one of the most powerful techniques for identification and (semi) quantitative elements determination in complex matrices. All the chemical elements can be detected in the range between boron and uranium, regardless of their state of oxidation. The qualitative analysis is possible by the identification of the emission lines characteristic of each chemical element, while the quantitative analysis requires calibrations with standards containing known amounts of the element to be estimated, in order to correlate the intensity of the signal with the concentration of the analyte.

1.5.4 Field emission gun scanning electron microscopy (SEM-FEG)

By SEM-FEG is it possible to obtain information about supported nanoparticles (see Chapter 2 for the case of SiO_2-PEI materials) and about morphology (texture) and dimensions of the nanoparticles. The fundamental difference between SEM-FEG and a conventional SEM is the higher resolution of the instrument, the ability to work at a lower voltage, and the higher gloss of the source of electrons emitted from a tungsten filament with a nanometer-sized tip. The SEM-FEG microscope uses a beam of high energy electrons directed onto the sample. The interaction between the incident beam (primary beam) and the sample surface generates different types of signals including secondary electrons (SE) and backscattered electrons (BSE), which, properly processed and amplified, give images with high resolution and depth of field.

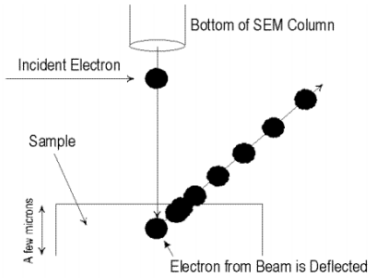

Figure 1.22 Back-scattered electron formation.

The secondary electrons generated by interaction with the primary beam derive from the first nanometers of the surface and provide information related to the morphology and topography of the sample. The backscattered electrons (Fig. 1.22), however, having much higher energy than the secondary ones, can emphasize contrasts in the composition of multiphase samples: in fact, elements having greater atomic numbers appear as bright areas.

The essential components of all SEMs include the following: i) electron lenses; ii) sample stage; iii) detectors for all signals of interest; iv) display / data output devices; v) infrastructure requirements: power supply, vacuum system, cooling system, vibration-free floor, and absence of electric fields in the ambient.

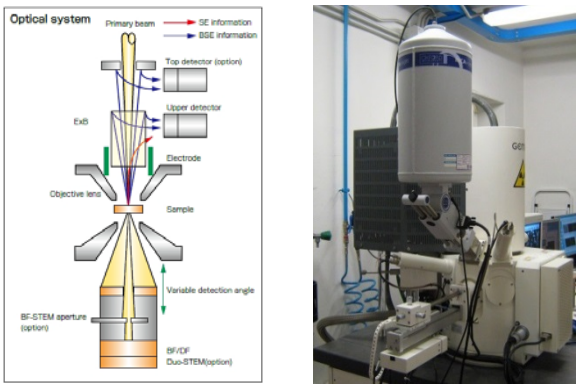

Figure 1.23 SEM-FEG instrument.

1.5.5 Transmission electron microscopy (TEM)

Transmission electron microscopy (TEM) is a microscopy technique whereby a beam of electrons is transmitted through an ultra-thin sample. An image is formed from the interaction of the electrons transmitted through the specimen. For lower magnification this is mainly due to absorbance of electrons, for higher magnification more complex interactions between electrons and sample occur. The image is magnified and detected by CCD camera.

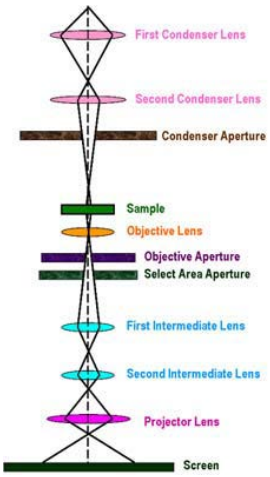

Figure 1.24 Scheme of a generic TEM instrument.

The instrument is composed by:

i) the electron gun (top), which produces a stream of monochromatic electrons;

ii) the double condenser lenses, which focus the electron beam onto the specimen;

iii) a condenser aperture that constrains the beam taking out high angle electrons (those far from the optic axis);

iv) the sample, which is stroked by the beam and, depending on the density of the material, causes some of the electrons to be scattered and to disappear from the beam and parts of them to be transmitted;

v) the objective lens, which focus the transmitted electrons into an image.

vi) the objective aperture, which blocks the electrons, resulting in an enhancement of the image contrast;

vii) the intermediate and projector lenses, which enlarge the image down the column;

viii) the image screen, where the unscattered electrons at the bottom of the microscope hit the phosphors, allowing the user to see a "shadow image" of the specimen with its different parts displayed in varied darkness according to their density. The darker areas of the image represent those areas of the sample where fewer electrons were transmitted, hence thicker or denser areas; the lighter ones represent zones were more electrons were transmitted through. It is worth emphasizing that, although electron microscopy is an important improvement over optical microscopy, nevertheless the produced image is however bydimensional.

1.6 Purpose of the work

The aim of this work was to project new materials involving silica particles functionalized with moieties (amine, sulfide, and alkyne groups) possessing a notable affinity with gold, so that they could be able to capture the gold precursor, to spontaneously reduce it (possibily at room temeperature), and to stabilize the resulting gold nanoparticles. These new materials, potentially suitable for heterogeneous catalysis applications, could represent a breakthrough among the "green" syntheses of supported gold nanoparticles, since they would circumvent the addition of extra reducing agents and stabilizers, also allowing concomitant absorption of the active catalyst particles on the support immediately after spontaneous formation of Au_{NPs}. In the literature only few works are reported dealing with analogous techniques. It will be also presented part of the work developed at the University of Lille (France) concerning in situ characterization by XAS spectroscopy of nanoparticles generated in a microfluidic system: that technique allowed formulation of some hypotheses about the mechanism of particles nucleation and growth under that conditions.

References

[1] The Royal Society & The Royal Academy of Engineering; *Nanoscience and nanotechnologies. Opportunities and uncertaintiess*, Ed.; Royal Society: London, **2004.**

[2] L.M. Liz-Marzan, P. V. Kamat, *Nanoscale Materials*, Kluwer Academic Publishers, New York, 2003. C. Burda, X. Chen, R. Narayanan, M. A. El-Sayed, *Chem. Rev.* **2005**, *105*, 1025.

[3] F. Caruso, Colloids and Colloid Assemblies, Wiley-VCH, Weinheim, **2004.**

[4] L.M. Liz-Marzan, P.V. Kamat, *Nanoscale Materials*, Kluwer Academic Publishers, New York, 2003.

[5] P. Zhao, N. Li, D. Astruc, *Coord. Chem. Rev.* **2013**, *257*, 638.

[6] V. Myroshnychenko, J. Rodriguez-Fernandez, I. Pastoriza-Santos, A. M. Funstn, C. Novo, P. Mulvaney, L. M. Liz-Marzan, F. J. Garcia de Abajo, *Chem. Soc. Rev.* **2008**, *37*, 1792.

[7] M. C. Daniel, D. Astruc, *Chem. Rev.* **2004**, *104*, 293.

[8] S. Eustis, M. A. El-Sayed, *Chem. Soc. Rev.* **2006**, *35*, 209.

[9]P. K. Jain, X. Huang, I. H. El-Sayed, M. A. El-Sayed, *Acc. Chem. Res.*, **2008**, *41*, 1578.

[10] M. Haruta, N. Yamada, T. Kobayashi, S. Lijima, *J. Catal*. **1989**, *115*, 301.

[11] M. Haruta, S. Tsuboda, T. Kobayashi, H. Kagehiama, M. J. Genet, B. Demon, *J. Catal*. **1993**, *144*, 175.

[12] T. V. Choudary, D. W. Goodman, *Top. Catal*. **2002**, *21*, 25.

[13] A. S. K. Hashmi, G. J. Hutchings, *Angew. Chem. Int. Ed.* **2006**, *45*, 7896.

[14] D. Astruc, F. Lu, J. R. Aranzaes, *Angew. Chem. Int. Ed.* **2005**, *44*, 7852.

[15] M. Faraday, *Philos. Trans*. **1857,** 147-145.

[16]*Surface Plasmon Nanophotonics*, ed. Brongersma M.L., LSPRinger, Dodrecht, **2007**.

[17] B Sepúlveda., P. C. Angelomé, L. M Lechuga, L. M. Liz-Marzán, *Nano Today* **2009**, *4*, 244.

[18] M. C. Daniel, D. Astruc, *Chem. Rev*., **2004**, 104, 293.

[19] B. Nikoobakht, M. A. E. I. Sayed, *Chem. Mater.*, **2003**, 15, 1957.

[20] J. Perez-Juste, L.M. Liz-Marzan, S. Carnie, D.Y.C. Chan, P. Mulvaney, *Adv. Funct. Mater*. **2004**, *101*, 571

[21] J. Rodriguez-Fernandez, J. Perez-Juste, F.J. Garcia, L.M. Liz-Marzan, *Langmuir* **2006**, *22*, 7007.

[22] S.D. Perrault, W.C.W. Chan, J. Am. Chem. Soc. **2009**, 131, 17042

[23] N.G. Bastus, J. Comenge, V. Puntes, *Langmuir* **2011**, 27, 11098.

[24] Royal Society of Chemistry, *Basic Principles of Colloid Science*, D. H. Everett, **1994.**

[25] J. Turkevitch, P. C. Stevenson, J. Hiller, *Discuss. Faraday Soc.* **1951**, *11*, 55.

[26] M. Brust, M. Walker, D. Bethell, D.J. Schiffrin, R.J. Whyman, *J. Chem. Soc., Chem. Commun*. **1994**, 801.

[27] G. Frens, *Nature: Phys. Sci.* **1973**, *241*, 20.

[28] S.K. Sivaraman, S. Kumar, V. Santhanam, *J. Colloid Interface Sci.* **2011**, 361, 543.

[29] X. Ji,X. Song,J. Li, Y. Bai, W. Yang, X. Peng, *J. Am. Chem. Soc* **2007**, *129*, 13939.

[30] M. Giersig, P. Mulvaney, *Langmuir* **1993**, *9*, 3408

[31] M. Brust, J. Fink, D. Bethell, D.J. Schiffrin, C.J. Kiely, J. Chem. Soc., *Chem. Commun.* **1995**, 1655.

[32] C. Xu, L. Sun, L.J. Kepley, R.M. Crooks, *Anal. Chem.* **1993**, 65, 2102.

[33] M. C. Daniel, D. Astruc, *Chem. Rev.* **2004**, *104*, 293.

[34] J.J. Chiu, B.J. Kim, E.J. Kramer, D.J. Pine, J. Am. Chem. Soc. **2005,** 127, 5036;

J. Shan, H. Tenhu, *Chem. Commun*. **2007**, 4580.

[35] K.R. Brown, M.J. Natan, *Langmuir* **1998,** 14, 726.

[36] M. Grzelczak, J. Perez-Juste, P. Mulvaney, L.M. Liz-Marzan, *Chem. Soc. Rev.* **2008**, *37*, 1783.

[37] N. R Jana, L. Gearheart, C. J. Mutphy, *Adv. Mater*. **2001**, *13*, 1389.

[38] B. Nikoobakht, M. A. El-Sayed, *Chem. Mater.* **2003**, 15, 1957.

[39] X. Huang, P. K. Jain, I. H. El-Sayed, M. A El-Sayed, *Lasers Med Sci.* **2008**, *23*, 217.

[40] M. C. Daniel, D. Astruc, *Chem. Rev.* **2004**, *104*, 293.

[41] Jana, N. R.; Gearheart, L.; Murphy, C. J. *Langmuir* **2001**, *17*, 6782

[42] M. J. Hostetler, J. E. Wingate, C. J. Zhong, J. E. Harris, R. W. Vachet, M. R. Clark, J. D. Londono, S. J Green, J. J. Stokes, G. D. Wignall, G. L. Glish, M. D. Porter, N. D. Evans, R. W. Murray, *Langmuir* **1998**, *14*, 17.

[43] X. Ji, X. Song, J. Li, Y. Bai, W. Yang, X. Peng, *J. Am. Chem. Soc*., **2007**, *129*, 13939.

[44] Rodriguez-Gonzalez, B., P. Mulvaney, L.M. Liz-Marzan, Z. *Phys. Chem* **2007**, *221*, 415.

[45] I. Ojea-Jimenez, F. M. Romero, N. G. Bastùs, F. Puntes,. *J. Phys. Chem*. C **2010,** *114*, 1800.

[46] B. Rodrıgez-Gonzalez, P. Mulvaney, L. M. Z Liz-Marzan, *Phys.Chem.Lett.* **2007**, *221*, 415.

[47] K. Angermund, M. Bhl, E. Dinjus, U. Endruschat, F. Gossner, H. Gnter Haubold, J. Hormes, G. Kohl,F. T. Mauschick, H. Modrow, R. Martel, R.Mynott, B. Tesche, T. Vad, N. Waldafner, Helmut Bonnemann, *Angew. Chem. Int. Ed.* **2002**, *41*, 4041

[48] J. Polte, T. T. Ahner, F. Delissen, S. Sokolov, F. Emmerling, A. F. Thunemann, R. Kraehnert, *J. Am. Chem. Soc*., **2010**, *132*, 1296.

[49] A. Plech, V. Kotaidis, K. Istomin, M. Wulff, *J. Synchrotron Radiation* **2007**, *14*, 288.

[50] S. Marre, F. Klavs, K. F. Jensen, *Chem. Soc. Rev*. **2010**, *39*, 1183.

[51] J. Wagner, T. Kirner, G. Mayer, J. Albert, J. M. Kohler, *Chem. Eng. J.*, **2004**, *101*, 251.

[52] J. Ftouni, M. Penhoat, A. Addad, E. Payen, C. Rolando, J. S. Girardon, *Nanoscale* **2012**, *4*, 4450.

[53] Corma A., Garcia H., *Chem. Soc. Rev.*, **2008**, *37*, 2096.

[54] R. Zanella, S. Giorgio, C. R. Henry, C. Louis, J. *Phys. Chem.* B **2002**, *106*, 7634.

[55] S. J. Lee and A. Gavriilidis, *J. Catal*. **2002**, *206*, 305.

[56] M. Haruta, *Gold Bull.* **2004**, *37*, 27.

[57] J. W. Geus and J. A. R. van Veen, *Catalysis: An Integrated Approach II, Stud. Surf. Sci. Catal*., **1999**, *123*, 459.

[58] A. Corma, P. Concepcion, I. Dominguez, V. Forne, M. J.Sabater, *J. Catal*. **2007**, *251*, 39.

[59] D. Astruc, F. Lu, J. R. Aranzaes, *Angew. Chem., Int. Ed*., **2005**, *44*, 7852.

[60] K. Esumi, A. Suzuki, A. Yamahira, K. Torigoe, *Langmuir* **2000**, *16*, 2604.

[61] I.T. Horvath, P.T. Anastus, *Chem. Rev*. **2007**, 107, 2169–2173.

[62] Calvert, J. B. Silicon. http://www.du.edu/~jcalvert/phys/silicon.htm, Date accessed 17/01/2014.

[63] C. H. Byers, M. T. Harris, D. F. Williams, *Ind. Eng. Chem Res*. **1987**, 26, 1916.

[64] A. M. Buckley, M. Greenblatt, P. G. Allen, and G. C. Lisensky, Experiment 15 in *Teaching General Chemistry: A Materials Science Companion*, A. B. Ellis, M. J. Geselbracht, B. J. Johnson, G. C. Lisensky, and W. R. Robinson, ACS Books: Washington, DC, 1993.

[65] W. Stober, A. Fink, E. Bohn, *J. Colloid Interface Sci*., **1968**, 26, 62

[66] J. Shen, Y. Zhu, X. Yang, J. Zong, C. Li, *Langmuir* **2013** 29 690

[67] S. Sacanna, A.P. Philipse, *Advanced Mat*., **2007**, 19, 22, 3824.

[68] A. P. Philipse, A. Vrij, *J. Colloid Interface Sci*., **1989**, *128*, 121.

[69] A. Van Blaaderen, A. Vrij, *J. Colloid Interface Sci.*, **1993**, *156*, 1.

[70] A. Van Blaaderen, A. Vrij, *Langmuir*, **1992**, *8*, 2921.

[71] A. Peled, V. Kotlyar and J.-P. Lellouche, *J. Mater. Chem.* **2009**, *19*, 268.

[72] X. Lu, F. Sun, J. Wang, J. Zhong and Q. Dong, *Macromol. Rapid Commun*., **2009**, *30*, 2116.

[73] L. F. Gutiérrez, S. Hamoudi, K. Belkacemi, *Catalysis* **2011**, *1*, 97.

[74] H. C. Kolb, M. G. Finn, K. B. Sharpless, *Angew. Chem., Int. Ed.*, **2001**, *40*, 2004.

[75] J. W. Chan, H. Zhou, C. E. Hoyle and A. B. Lowe, *Chem. Mater.*, 2009, 21, 1579.

[76] H. Y. Shiu, T. C. Chan, C. M. Ho, Y. Liu, M.-K. Wong, C. M. Che, *Chem. Eur. J.* **2009**, *15*, 3839.

[77] M. Minozzi, A. Monesi, D. Nanni, P. Spagnolo, N. Marchetti, A. Massi, *J. Org. Chem.*, **2011**, *76*, 450.

[78] A. Massi, D. Nanni, *Org. Biomol. Chem.*, **2012**, *10*, 3791.

[79] M. Guerrouche, S. M. Chergui, M. M. Chehimi, B. Carbonnier, *Chem. Comm*. **2012**, *48*, 7486.

[80] H. Winick, *Sci. Am.*, **1987**, 257, 88.

[81] H. Winick, S. Doniach, *Synchrotron Radiation Research*, Plenum, New York, 1980.

[82] Tabulated values of each element's absorption edge energies are reported in Advanced Light Source (http://xdb.lbl.gov/)

2. SYNTHESIS OF GOLD NANOPARTICLES SUPPORTED ON COMMERCIAL SILICA-POLYETHYLENEIMINE BEADS 35

2.1 Results and Discussion 36

2.1.1 Characterization of SiO_2-PEI 36
2.1.2 Preparation of Au_{NPs}/(SiO_2-PEI) beads 38
2.1.3 X-Ray Absorption Spectroscopy studies 44
2.1.4 Catalytic activity 50

2.2 Experimental Section 55

2.2.1 Materials 55
2.2.2 Instruments 55
2.2.3 Preparation of Au_{NPs}/(SiO_2-PEI) beads 56
2.2.4 XAS Data Collection 57
2.2.5 Catalytic reduction of 4-nitrophenol (4-NP) 58

2.3 Conclusions 60

CHAPTER 2

2. Synthesis of gold nanoparticles supported on commercial silica-polyethyleneimine beads

Stable silica-supported gold nanoparticles (Au_{NPs}) suitable for catalysis applications were conveniently obtained in a straightforward, one step synthesis by simply adding an aqueous solution of $HAuCl_4$ to commercial polyethyleneimine-functionalized silica beads (SiO_2-PEI) as the only reactant without any external reducing agent and/or conventional stabilizing moieties. Six different types of Au_{NPs}/(SiO_2-PEI) beads termed **Au_x-$_y$h**, where *x* is the initial $HAuCl_4$ concentration (1, 5, or 10 mM) and *y* is the reaction time (1 or 24 h), were prepared and characterized by UV-Vis Diffuse Reflectance Spectroscopy, X-Ray Fluorescence, FE-SEM microscopy, and X-ray absorption spectroscopy.

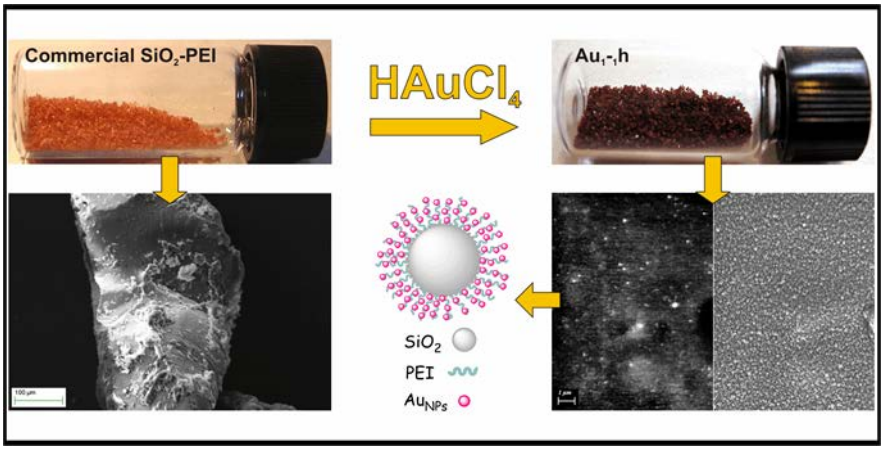

The SEM micrographs of **Au_x-$_y$h** samples showed that the particles size distribution decreases with the increase of the starting gold concentration, i.e. 70-100 nm for **Au_1-$_x$h**, 40-70 nm for **Au_5-$_x$h** and **Au_{10}-$_x$h,** whereas on passing from 1 to 24 h the aggregation phenomena overcome the nucleation ones, promoting the formation of bigger aggregates at expense of small Au_{NPs}.

The XAS analysis as a combination of XANES and EXAFS studies provided detailed structural information regarding the coordination geometry and oxidation state of the gold atoms present on the beads. Moreover the catalytic activity of the modified silica beads in the reduction of 4-nitrophenol to 4-aminophenol by $NaBH_4$ was investigated and in one case the XAS analysis was repeated after recovery of the catalyst, demonstrating further reduction of the Au site to Au(0).

2.1 Results and Discussion

2.1.1 Characterization of SiO_2-PEI

Since colour and granulometry were the only information provided by the vendor, first the commercial polyethyleneimine-functionalized silica beads (SiO_2-PEI), a material normally used as a cationic ion-exchange resin, were fully characterized in house by the following techniques: simultaneous Thermogravimetry-Differential Scanning Calorimetry (TG-DSC), acid-base titration analyses, FTIR and ATR-FTIR spectroscopy, SEM microscopy, surface area and porosimetry.

The TGA-DSC thermogram of SiO_2-PEI (continuous line), reported in Fig. 2.1, shows in the range 30÷140 °C a weight loss of 2.4 wt%, ascribed to desorption of water from the sample, confirmed by the presence of an endothermic process in the DSC analysis (dotted line). The decomposition of the organic material started at 180 °C and terminated at ca. 600 °C: in the same interval the DSC curve showed two exothermic processes at 354 °C and 500 °C, respectively. The former is ascribable to PEI combustion, which has been reported to be between 280 °C and 350 °C,[1,2] whilst the latter is probably due to combustion of *"coupling agent"* molecules, such as (3-chloropropyl)trimethoxysilane, used to anchor PEI to the silica substrate.[3] The total weight loss for the organic material was 12 wt%.

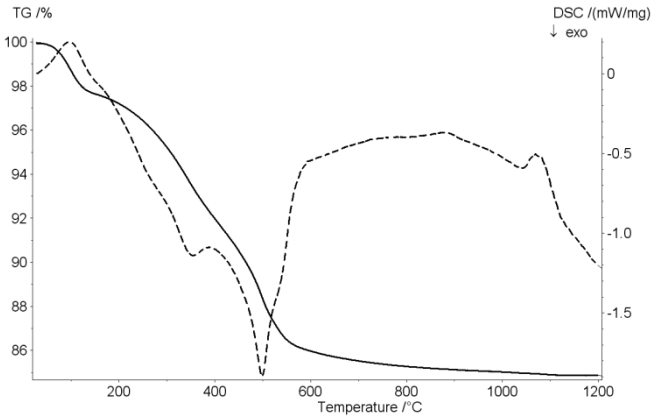

Figure 2.1 TGA (continuous line) and DSC (dotted line) of SiO_2-PEI commercial sample.

The concentration of the amino groups on SiO_2-PEI was evaluated by acid-base titration analyses [3] with a value equal to 0.103 ± 0.005 mmol g^{-1}.

The specific surface of the beads was measured by N_2 adsorption/desorption giving a value of 335 m^2 $g^{-1}$and the total pore volume of 0.347 cm^3 g^{-1}, with a narrow pore size distribution with an average pore size (the distance between two opposite walls of the pore) of 31.9 Å, in the range of the mesoporous materials (Fig. 2.2).[4]

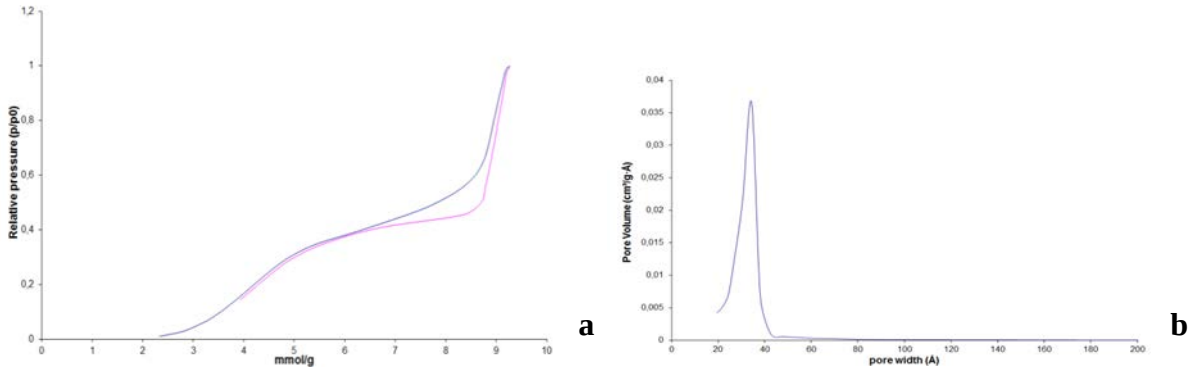

a b

Figure 2.2 a) Isotherm of N_2 adsorption-desorption for SiO_2-PEI; **b)** average pore size distribution of SiO_2-PEI.

The FTIR spectrum of SiO_2-PEI (Fig. 2.3) showed the strong absorption bands expected for the stretching and bending vibrations of the Si-O-Si (1090 cm^{-1}), SiOH (3437 and 709 cm^{-1}), and hydrogen-bonded SiOH groups (1644 cm^{-1}). The weak peaks at 2944 cm^{-1} e 2864 cm^{-1} are ascribable to the ν_s and ν_{as} CH stretching modes of PEI, while the peaks at 1559 cm^{-1} and 1458 cm^{-1} are associated to the ν_s and ν_{as} bending vibrations of the primary amines. The band at 864 cm^{-1} is the wagging vibration of the primary amine.[5,6,7]

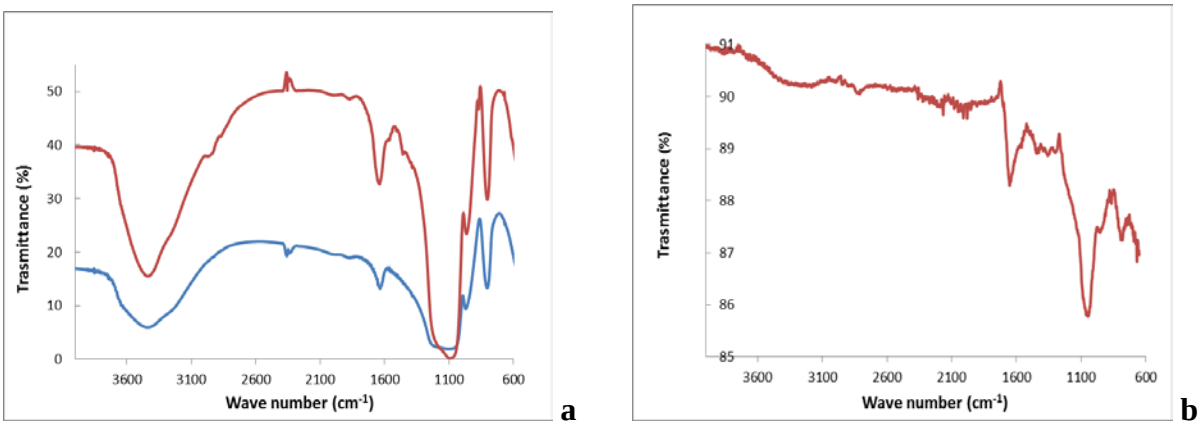

a b

Figure 2.3 a) FT-IR spectra of SiO_2-PEI (red line) compared to SiO_2 (blue line); **b)** ATR-IR spectra of SiO_2-PEI.

In the ATR spectrum (Fig.2.3 a) signals related to PEI are much more distinguishable, because the sample was analyzed without being reduced to a powder and the surface of the beads was directly investigated.

SiO_2-PEI was also investigated by SEM where it was visible the irregular shape of the material (in the order of the micrometres) and the polymer on the surface.

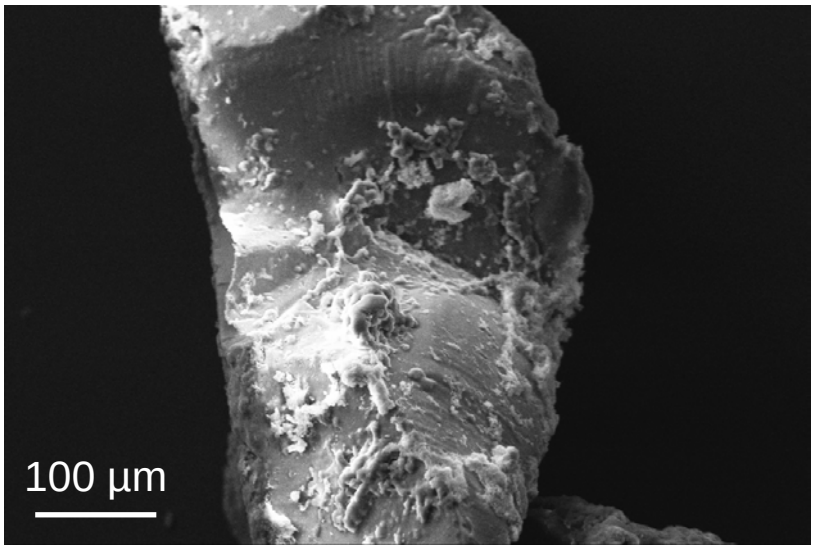

Figure 2.4: SEM image of SiO_2-PEI

2.1.2 Preparation of Au_{NPs}/(SiO_2-PEI) beads

The preparation of silica-supported Au_{NPs} was particularly straightforward and was performed in just one step by simply adding the silica-polyethylenimine beads to an aqueous solution of $HAuCl_4$ kept at 25 °C on an orbital shaker. After few minutes the yellow colour of the solution faded completely, due to adsorption of chloroauric acid on the SiO_2-PEI beads, with a concomitant variation in color of the latter (the change in colour of the supernatant solution was monitored by UV-Vis spectroscopy measuring the decrease in absorbance of λ_{max} at 300 nm of $HAuCl_4$, (Fig. 2.5 a and b).

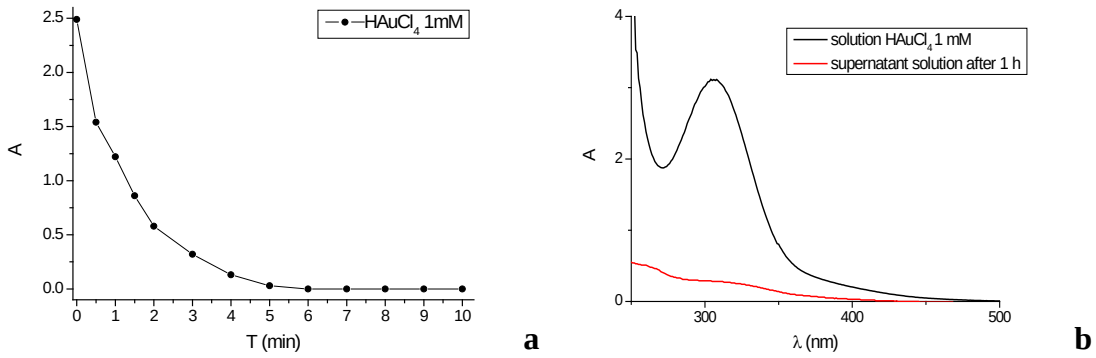

Figure 2.5 a) Absorbance vs. time after the addition of SiO_2/PEI to a solution of $HAuCl_4$ 1 mM**; b)** UV-Vis spectra of $HAuCl_4$ solution (1 mM) and of the supernatant solution after 1 h since the addition of SiO_2-PEI.

The resulting brownish-red colour of the beads, whose hue and intensity depended on both reaction times and initial concentrations of $HAuCl_4$, indicated the formation of supported Au_{NPs} by *in situ* post position reduction of Au(III) to Au(0) operated by PEI.[8,9] The six different types of

Au_{NPs}/(SiO_2-PEI) beads, hereafter also termed **Au_x-$_y$h**, where *x* is the initial $HAuCl_4$ concentration (1, 5, or 10 mM) and *y* is the reaction time (1 or 24 h), shown in Fig. 2.6 were obtained from the corresponding reaction mixtures after filtration, washing with deionized water, and drying under vacuum.

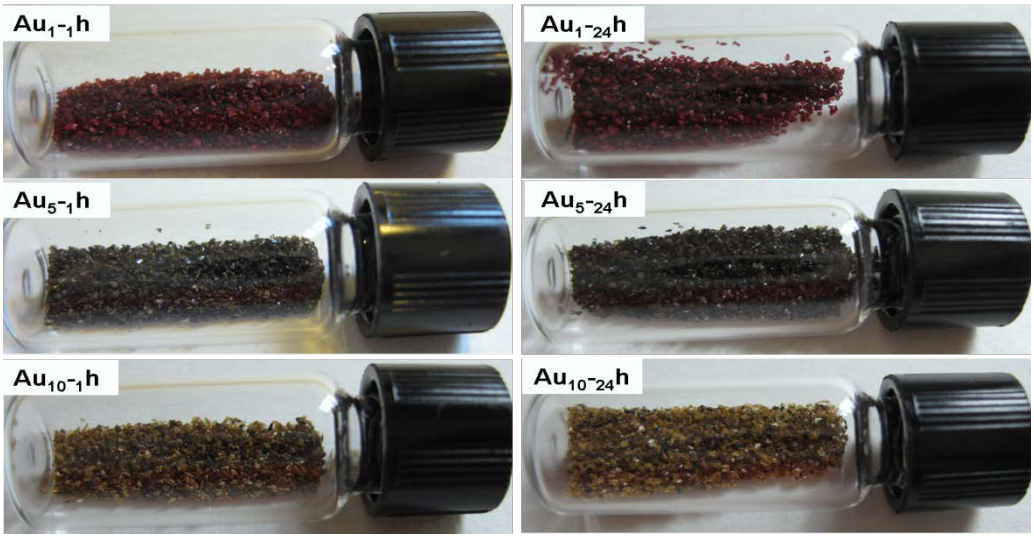

Figure 2.6 Photographs of Au_{NPs}/(SiO_2-PEI) samples.

The characterization of the beads by DR-UV-Vis spectroscopy (Fig. 2.7) showed that all the prepared materials exhibited three broad absorption bands with maxima in the range 400-800 nm, characteristic of the Plasmon resonance of Au_{NPs} (see also in the Introduction). [10,11]

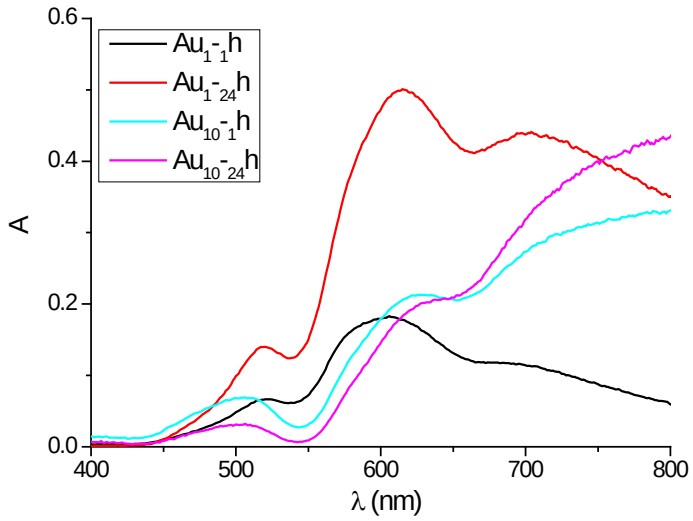

Figure 2.7 UV-Vis Diffuse Reflectance spectra of Au_1-$_y$h and Au_{10}-$_y$h.

The total amount of gold present on the SiO_2-PEI beads was indirectly estimated by analyzing the supernatant solution immediately after reaction completion with a Wavelengths Dispersive XRF instrument. In Table 2.1 the initial supernatant gold concentration ($[Au]_i$), the final one ($[Au]_f$), and

the amount of gold in each **Au_x-$_y$h** sample obtained by the difference ($[Au]_i$ - $[Au]_f$) divided by the quantity of SiO_2-PEI

.

Table 2.1 Amount of gold in the supernatant solution at the end of the reaction $[Au]_f$ and in each Au_x-$_y$h sample.[a]

Entry	Sample	$[Au]_i$ (mM)	Time (h)	$[Au]_f$ (mM)	$[Au]_{theoretical}$ (mmol g^{-1})	$[Au]_{effective}$ (mmol g^{-1})
1	Au_1-$_1$h	1	1	-	$2.50\cdot10^{-2}$	$2.50\cdot10^{-2}$
2	Au_1-$_{24}$h	1	24	-	$2.50\cdot10^{-2}$	$2.50\cdot10^{-2}$
3	Au_5-$_1$h	5	1	$3.38\cdot10^{-2}$	$1.25\cdot10^{-1}$	$1.24\cdot10^{-1}$
4	Au_5-$_{24}$h	5	24	$5.08\cdot10^{-2}$	$1.25\cdot10^{-1}$	$1.24\cdot10^{-1}$
5	Au_{10}-$_1$h	10	1	$7.61\cdot10^{-2}$	$2.50\cdot10^{-1}$	$2.48\cdot10^{-1}$
6	Au_{10}-$_{24}$h	10	24	$8.46\cdot10^{-2}$	$2.50\cdot10^{-1}$	$2.48\cdot10^{-1}$

[a] The measurements are subjected to an relative error of 5%.

The morphology of the Au_{NPs} pertaining to different **Au_x-$_y$h** samples was investigated by Field Emission-Scanning microscopy (FE-SEM); due to the non-conductive nature of the Au_{NPs}/(SiO_2-PEI) beads and in order to reduce charging effects, prior to FE-SEM measurements the samples were coated with a 10 nm thick carbon films. The images reported in Fig. 2.14 were obtained collecting both the secondary (SE) and backscattered (BSE) electron signals. The BSE micrographs clearly reveal the presence of metallic NPs with a near-spherical shape; while the SE ones (Figs. 2.8 – 2.13) show the porous structure of SiO_2-PEI materials in which the Au_{NPs} are distributed.

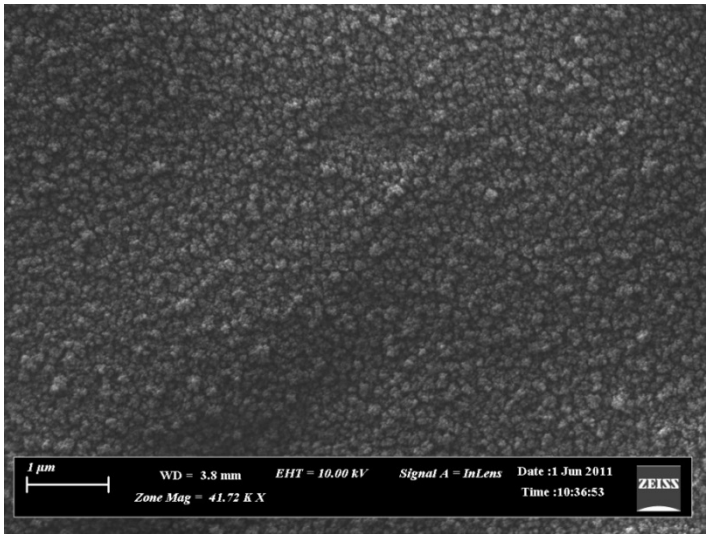

Figure 2.8: SEM-FE image of Au_1-$_1$h in SE modality.

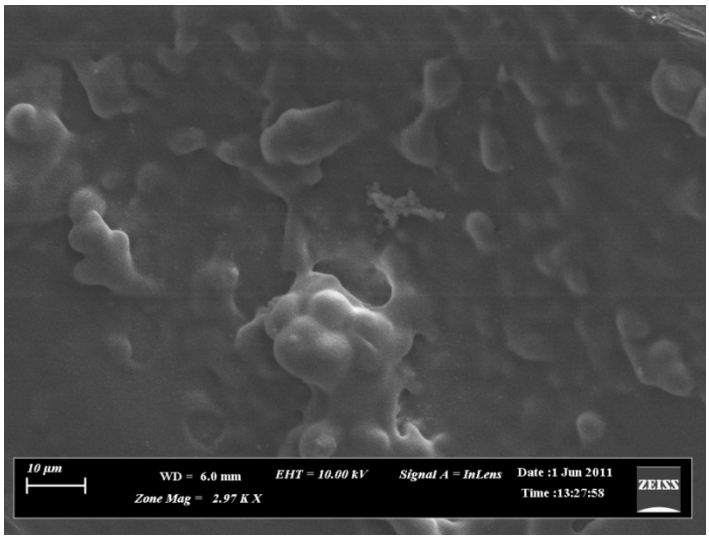

Figure 2.9 SEM-FE image of Au_{1}-$_{24}$h in SE modality.

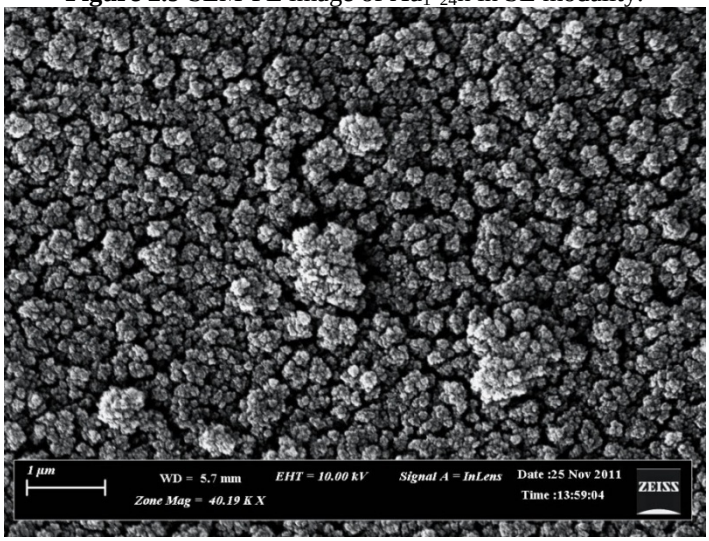

Figure 2.10 SEM-FE image of Au_{5}-$_{1}$h in SE modality.

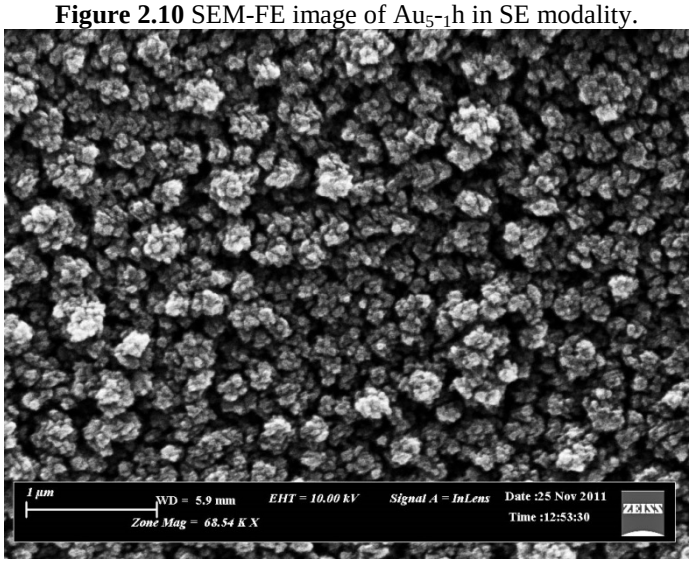

Figure 2.11 SEM-FE image of Au_{5}-$_{24}$h in SE modality.

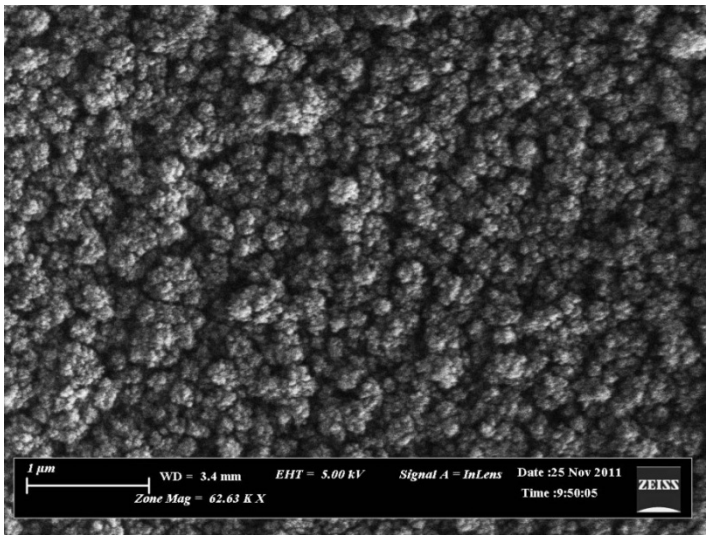

Figure 2.12 SEM-FE image of Au_{10}-$_1$h in SE modality.

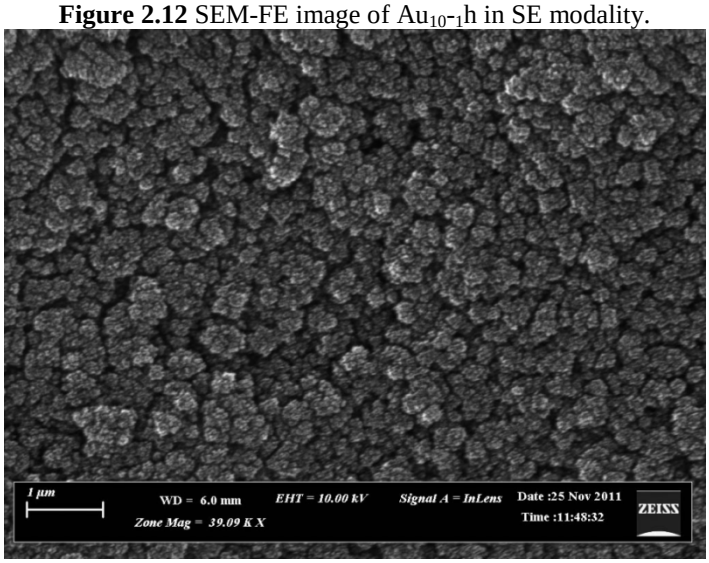

Figure 2.13: SEM-FE image of Au_{10}-$_{24}$h in SE modality.

The SEM micrographs of **Au_x-$_y$h** samples (Figs. 2.8-2.13) analyzed by the Image-J software [12] revealed what follows: *i*) the particles size distribution decreases with the increase of the starting gold concentration, i.e. 70-100 nm for **Au_1-$_x$h**, 40-70 nm for **Au_5-$_x$h** and **Au_{10}-$_x$h** with the exception of **Au_{10}-$_{24}$h** (ca. 140-220 nm); ii) on passing from 1 to 24 h the aggregation phenomena overcome the nucleation ones, promoting the formation of bigger aggregates at expense of small Au_{NPs}: this trend is particularly striking for **Au_{10}-$_{24}$h**. In all cases we observed an homogeneous Au delivery, confirmed by the bright spots distribution in BSE-SEM mode.

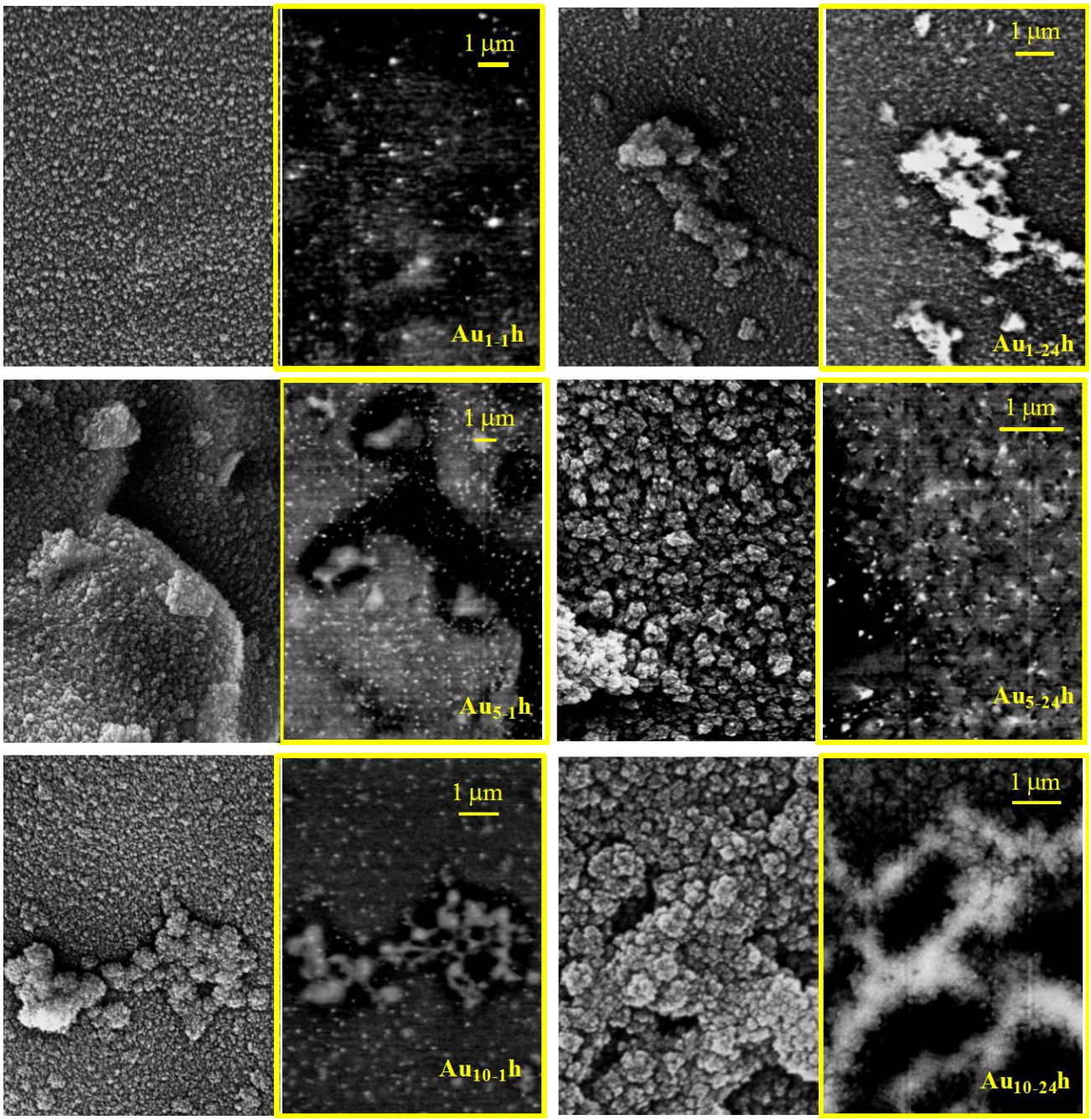

Figure 2.14 SEM micrographs pertaining to samples having three different Au_{NPs}/(SiO_2-PEI) concentration levels (1, 5 and 10 mM) and reaction times (1 or 24 h): All the reported images were collected in SE and BSE (in yellow boxes) mode.

2.1.3 X-Ray Absorption Spectroscopy studies

The SEM characterization gave no information about the degree of reduction that corresponds to the quantity of gold actually reduced by PEI; therefore, in order to obtain useful structural information regarding the coordination geometry and oxidation state of gold on the beads, XANES (X-ray Absorption Near-Edge Structure) and EXAFS (Extended X-Ray Absorption Spectroscopy) spectra were taken at the L_{III} edge of Au of several **Au$_{x}$-$_{y}$h** samples.[13, 14]

Typically, XANES spectra are very sensitive to both local geometry and charge associated to the photo-absorbing atom, Au in this case. As seen in Fig 2.15, the XANES spectrum of the precursor, $HAuCl_4$, was characterized by a sharp peak on the rising edge at about 11920 eV (peak A), which is absent in the case of bulk Au(0). This peak, called *white line*, is assigned to a *2p-5d* transition and has been used as an optimal probes of the unfilled *5d* states.[15] As expected, the white line is present in the case of Au(III) precursor being the Au electronic configuration $5d^8 6s^0$, but not in the case of bulk Au, where the electronic configuration is $5d^{10} 6s^1$. On the contrary, two broad peaks C and D at about 11945 and 11967 eV are not only characteristics of bulk Au(0) but are missing in the case of $HAuCl_4$. Therefore, the intensity of these features, highlighted by dash lines in Fig. 2.15, could be used as an indicator of the Au oxidation state in our catalytic samples.[16]

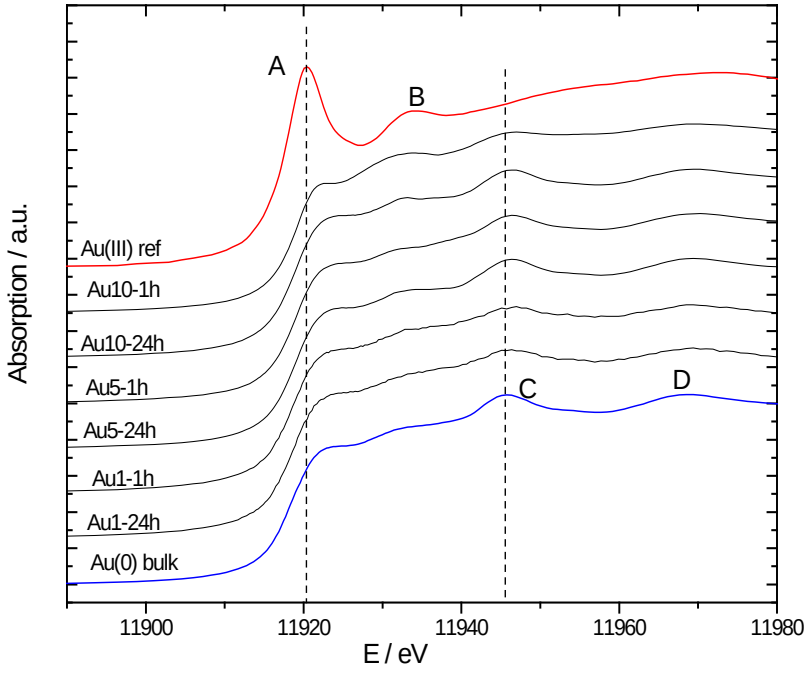

Figure 2.15 XANES spectra taken at the L_{III} edge of Au of the **Au$_{x}$-$_{y}$h** samples, together with the references ones: Au(0) bulk and $HAuCl_4$.

A first look to the XANES spectra suggests a close similarity of all **Au$_{x}$-$_{y}$h** samples to that of bulk Au(0), except for **Au$_{10}$-$_{1}$h**. In fact, peak A was almost completely absent and two broad peaks

C and D are present in the edge region in all **Au_x-$_y$h** samples. The only detectable difference comes out by the **Au_{10}-$_1$h** spectrum, which seems to lie in an intermediate situation between the two reference curves: peak A is suppressed, peak B is present but shifted in energy, and peaks C and D are suppressed. These findings suggest a formal oxidation state close to zero for the all investigated **Au_x-$_y$h** samples with the exclusion of the **Au_{10}-$_1$h**.

To gain a more quantitative understanding of the Au oxidation state and of the atomic environment in the different **Au_x-$_y$h** samples, the XANES spectra were examined by means of a Linear Combination Fitting (LCF) of standard spectra of the Au(III) precursor and Au(0) in order to give the relative abundance in terms of these two reference materials. The LCF was performed with the ATHENA program using the calibrated, aligned, and normalized XANES spectra of **Au_x-$_y$h**.

The LCF results, reported in Table 2.1, indicate a very large degree of conversion to Au(0) for all **Au_x-$_y$h** samples, with values in the range of 93-99%, with the exception of **Au_{10}-$_1$h**, where 1/3 of the sample is still in the Au(III) oxidation state, thus confirming the suggestions of Fig. 2.15 about the oxidation state of Au in the various samples.

Table 2.2 Linear Combination Fitting Results of the XANES spectra of Au_x-$_y$h samples with standard spectra of the Au(III) precursor and Au(0). The relative composition (wt %) of Au(III) and Au(0) for each sample is reported.

Sample	E_0 of sample	**Norm(E), 20 to 100 eV**			
		wt% Au(0)	**wt% Au(III)**	err	FIT χ^2
Au_1-$_1$h	11919	**94.5**	**5.5**	0.034	0.027
Au_5-$_1$h	11919	**96.7**	**3.3**	0.02	0.0095
Au_{10}-$_1$h	11919	**67.1**	**32.9**	0.024	0.014
Au_1-$_{24}$h	11919	**93.1**	**6.9**	0.021	0.0073
Au_5-$_{24}$h	11919	**99.2**	**0.8**	0.016	0.0061
Au_{10}-$_{24}$h	11919	**96.8**	**3.2**	0.013	0.0037
Au_{10}-$_1$h recycled	11919	**90.9**	**9.1**	0.025	0.044

From the graphical point of view the present LCF analysis is rather good. As depicted in Fig 2.16 there are good matches between the fit and experimental curves in all panels, with the exception of data around the edge position (11919 eV), where there are difficulty to correlate the chemical oxidation state of the peaks A and B of the XANES. because they a. In fact, as seen in the literature[17] those peaks are not only dependent on the formal oxidation state of Au (i.e. Au(III)) but

also from the local geometry around the metal. For this reason the energy region concerning peaks A and B was excluded from the fitting, including only the interval of energies from 20 to 100 eV after the *white line*.

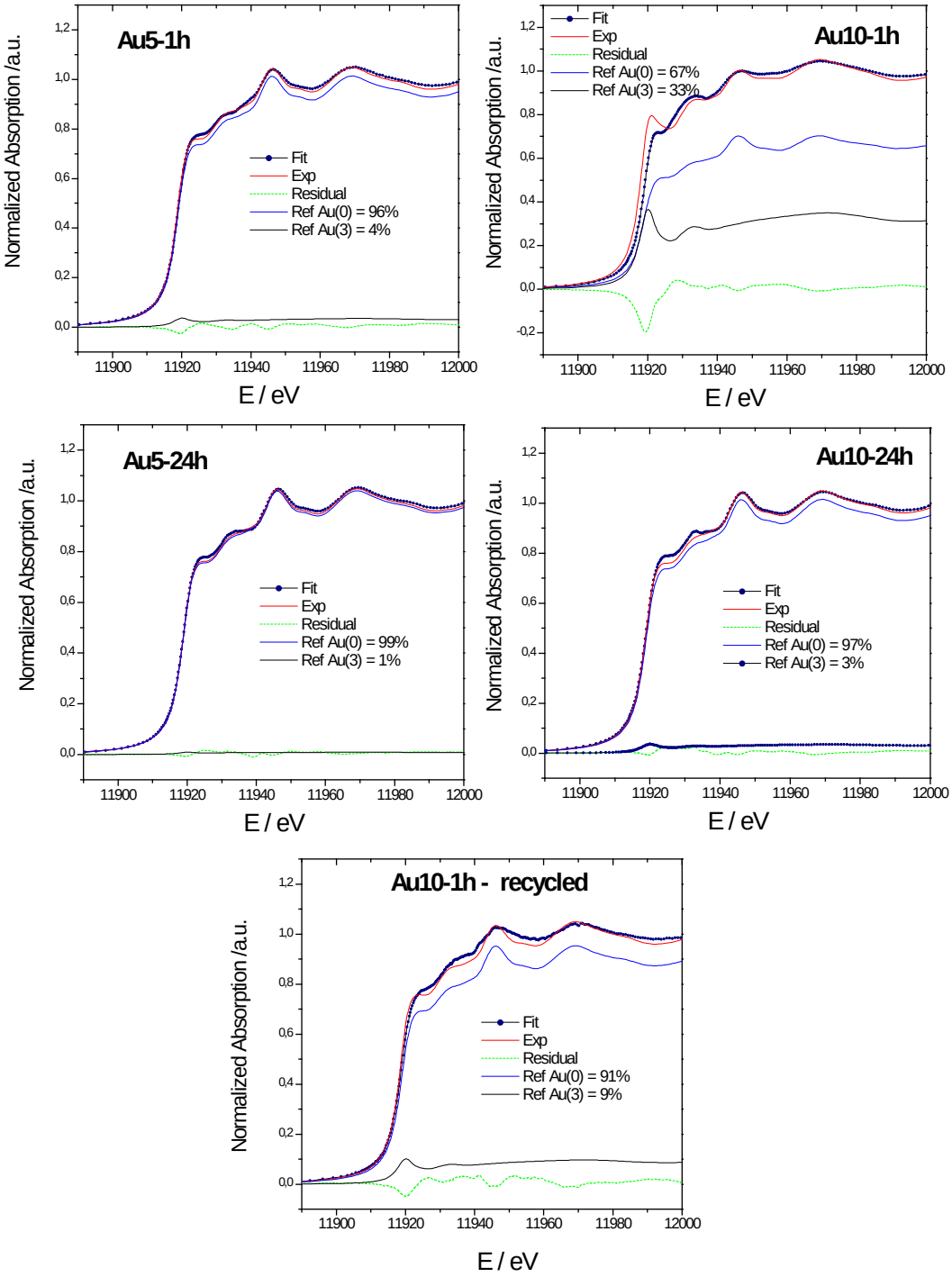

Figure 2.16 LCF analysis of the XANES spectra for some selected Au_x-$_y$h samples. Each panel reports the experimental, the fitting curve, the component of the references spectra (Au(III) and Au(0)), and the residual curve. The residual curves may appear large around the 11900 eV in the case of **Au_{10}-$_1$h** sample.

It is also worth to point out that only two components were used for the fitting, which are Au(0) and Au(III). This automatically excludes the occurrence of others Au oxidation state, like the Au(I), in the investigated samples.

The obtained result is of great importance because the XAS technique probes actually the bulk structure; hence, the information is not only related to the surface of the catalyst but also concerns the overall portion of the material.

Fig. 2.17 shows the degree of conversion (%) of Au(III) to Au(0) for the all investigated samples, as comes out from the XANES LCF analysis. Besides the facts that the values are nearly 100% with the exception of **Au_{10}-$_1$h**, where 1/3 of the sample is still in the Au(III) oxidation state (as already seen in Table 2.2), there is a new datum concerning the **Au_{10}-$_1$h** sample, recorded after been recycled one time from a catalytic test: in such a case the degree of conversion to Au(0) reaches the typical value found for the other samples, as indicated by the arrow in the figure. This result, although not surprising as the recovered sample was obtained from the catalytic test which uses an excess of $NaBH_4$ for the 4-NP to 4-AP reaction (see paragraph 2.1.4), underlines once again the suitability of the XAS approach for the study of these materials.

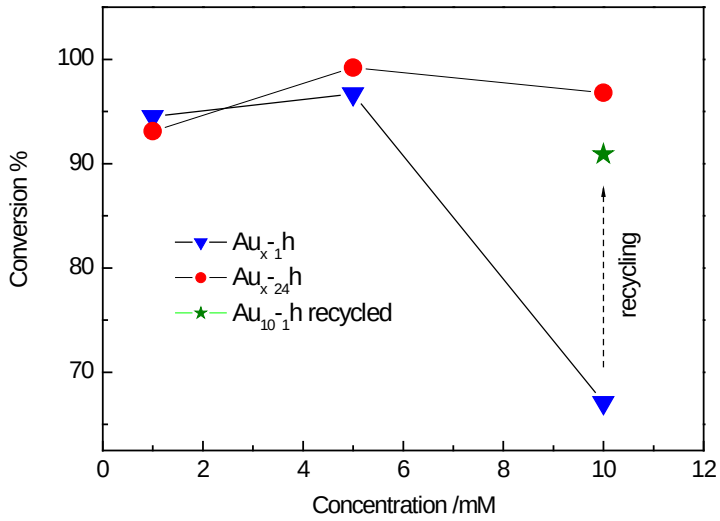

Figure 2.17 Plot of the degree of conversion (%) of Au(III) to Au(0) for all Au_x-$_y$h samples.

In order to investigate in depth the local structure of Au in the various samples, an EXAFS analysis was carried out. As a customary while analysing the EXAFS data, a structural model must be chosen for the theoretical signals calculations. As specified in the Experimental section, the fitting procedure was conducted using the structure of bulk Au(0), also taking into account the suggestion of the XANES LCF analysis which anticipates the occurrence of the bulk Au in most of

our samples. The results of the fitting procedures, in terms of first shell distances of Au and the corresponding EXAFS bond variance, are presented in Table 2.3. Figure 2.18 reports the best fit results for some selected samples (**Au_{5}-$_{1}$h** and **Au_{5}-$_{24}$h)** in comparison with the Au(0) bulk as a reference. Concerning the Au(0) bulk, not only the Au-Au first shell bond distance, listed in Table 2.3, agrees with previous studies[13,18,19] but also the perfect match between the experimental and theoretical curves of Fig. 2.18 demonstrated the reliability of the present data analysis. Furthermore, Au_{NPs}/SiO_2-PEI samples fit well with a structural model typical of bulk Au, except for the **Au_{10}-$_{1}$h** sample, where a large unaccounted signal was found, demonstrating the appropriateness of the chosen structural model for Au.

Table 2.3 Atomic first shell distance (Au-Au), and coordination number (CN) concerning the investigated samples, and bulk Au for comparison.

Sample	CN	Au-Au distance/Å	σ^2/Å^2
Au(0) bulk	12	2.87(1)	0.008(3)
Au_{1}-$_{1}$h	12	2.81(2)	0.011(2)
Au_{1}-$_{24}$h	12	2.81(2)	0.010(2)
Au_{5}-$_{1}$h	12	2.883(7)	0.009(1)
Au_{5}-$_{24}$h	12	2.86(1)	0.009(1)
Au_{10}-$_{1}$h	12	2.80*	0.019*
Au_{10}-$_{1}$h (recycled)	12	2.88(3)	0.018(4)
Au_{10}-$_{24}$h	12	2.863(8)	0.009(2)

*Data for the **Au_{10}-$_{1}$h** sample are considered unreliable, due to the presence of Au(III) that leads to poor fitting results.

As displayed in Table 2.3, all the **Au_{1}-$_{y}$h** samples are characterized by Au-Au distances which are slightly shorter than in bulk Au and in several cases the structural disorder (EXAFS bond variance) is higher compared to that of bulk Au. The best agreement to Au bulk was found for **Au_{5}-$_{y}$h** and **Au_{10}-$_{24}$h** samples, thus confirming the XANES LCF analysis. In both cases, a perfect agreement of the theoretical signals to the experimental ones (Fig. 2.18) was observed.

The coordination number of the first shell is 12, as expected for a *ccp* structure. Concerning this value, it is worth to consider that the size range of the obtained Au_{NPs} (40-100 nm, as indicated by FE-SEM) is large enough to avoid any grain boundary effects, which would have produced the consequence of reducing the mean coordination number of the nanoparticles.[20] A combined XANES/EXAFS analysis on an extended variety of $Au_{NPs}/(SiO_2$-PEI) catalytic samples prepared under different reaction conditions is currently in progress.

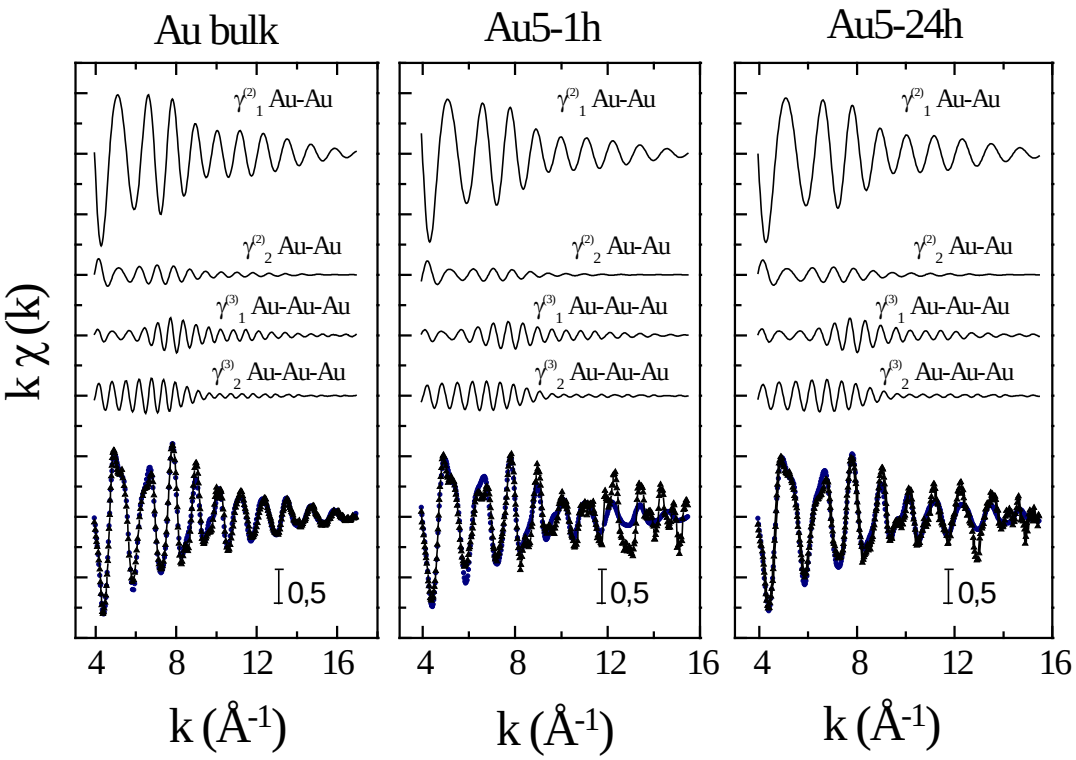

Figure 2.18 Details of the EXAFS analysis of the Au L_{III}-edge of Au(0) foil and of some selected Au_x-$_y$h samples. The figure shows the individual EXAFS contributions, in terms of two-body and three-body signals, to the total theoretical signal. The comparison of the total theoretical signal (…) with the experimental one (-) is also reported.

2.1.4 Catalytic activity

For an easy, rapid evaluation of the catalytic performances of the **Au_x-$_y$h** samples, the catalytic reduction of 4-nitrophenol (4-NP) to 4-aminophenol (4-AP) with an excess amount of $NaBH_4$ was chosen as a model reaction.[21,22,23,24,25,26,27,28,29] The reduction, neither achievable in the absence of the catalyst nor with SiO_2-PEI only (Fig. 2.20), was performed in a quartz cuvette, without stirring the slurry reaction and with different Au/4-NP ratios, fallowing directly the reaction by UV-Vis spectroscopy in function of the time.

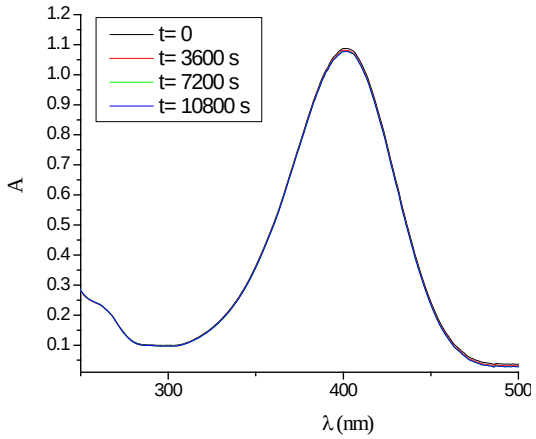

Figure 2.19: Reduction of 4-NP in aqueous solution recorded every hour using SiO_2-PEI only.

As shown in Table 2.4 and Fig. 2.20, for a Au/4-NP ratio of 1/0.44 the samples **Au_{1}-$_{1}$h** and **Au_{1}-$_{24}$h** gave the best catalytic performances (entry 1 and 2) with rate constants in the range of previously reported literature data. These values are not considerably different from the ones reported for entries 3-6 and reflect the observed minor differences between the corresponding particle sizes and morphology. Moreover, the present data show that the higher catalytic activity does not correspond to the lower particles size; this is not surprising since the size range of our systems is beyond the range in which the effect of particle size on the rate of reduction is prominent.[30]

Table 2.4 Kinetic constants (k) of 4-NP reduction using different catalysts.

Entry	Sample	wt Au (%)	Au/4-NP/$NaBH_4$ (mol/mol/mol)	k (s^{-1})	R^2
1	**Au_{1}-$_{1}$h**	0.5	1/0.44/711	6.84 x 10^{-4}	0.999
2	**Au_{1}-$_{24}$h**	0.5	1/0.44/711	5.98 x 10^{-4}	0.997
3	**Au_{5}-$_{1}$h**	2.4	1/0.44/711	1.33 x 10^{-4}	0.998
4	**Au_{5}-$_{24}$h**	2.4	1/0.44/711	1.02 x 10^{-4}	0.988
5	**Au_{10}-$_{1}$h**	4.9	1/0.44/711	3.39 x 10^{-4}	0.986
6	**Au_{10}-$_{24}$h**	4.9	1/0.44/711	1.06 x 10^{-4}	0.987

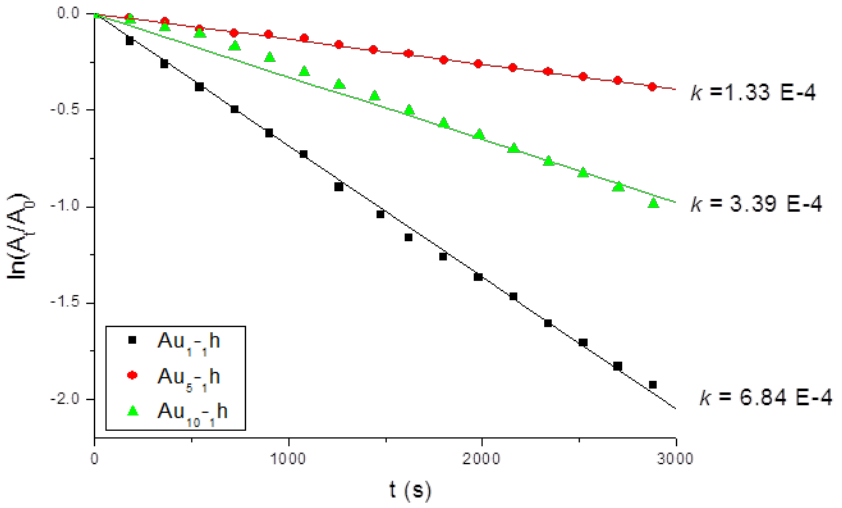

a

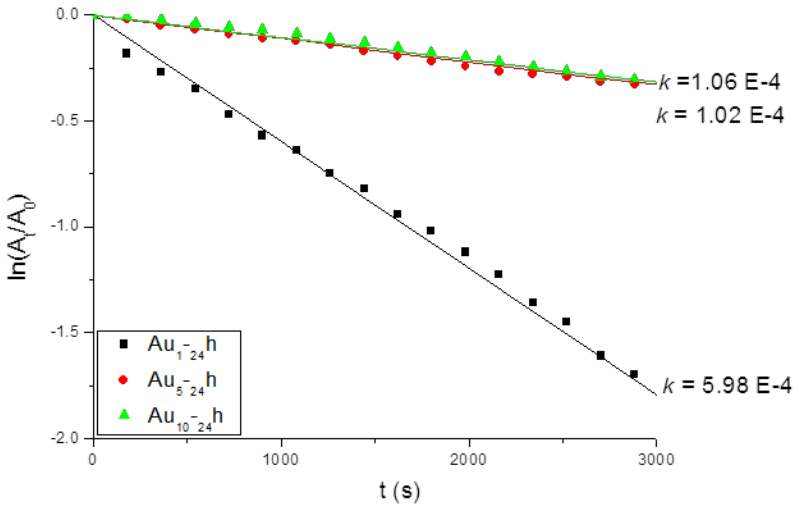

b

Figure 2.20 Plots of $\ln(A_t/A_0)$ *vs* time for the reduction of 4-NP catalyzed by different $Au_{NPs}/(SiO_2$-PEI) beads with Au/4-NP/$NaBH_4$ ratios as reported in Table 4. **a) Au_{x}-$_{1}$h**; **b) Au_{x}-$_{24}$h**. Reaction conditions: aqueous media at 295 K, [4-NP] = 5.19 × 10^{-2} mM, [$NaBH_4$] = 83 mM, Au = 0.34 µmol.

The values of rate constants for 4-NP ratio of 1/1 for $Au_{x-y}h$ are reported in Table 2.5 and Fig. 2.21, in this case a slight decrease in these values values is observed.[31]

Table 2.5 Kinetic constants (k) of 4-NP reduction using different catalysts.

Entry	Sample	wt Au (%)	Au/4-NP/ $NaBH_4$ (mol/mol/mol)	k (s^{-1})
1	Au_{1}-$_{1}$h	0.5	**1/1/1660**	2.29 10^{-4}
2	Au_{1}-$_{24}$h	0.5	**1/1/1660**	1.31 10^{-4}
3	Au_{5}-$_{1}$h	2.4	**1/1/1660**	0.96 10^{-4}
4	Au_{5}-$_{24}$h	2.4	**1/1/1660**	0.48 10^{-4}
5	Au_{10}-$_{1}$h	4.9	**1/1/1660**	1.24 10^{-4}
6	Au_{10}-$_{24}$h	4.9	**1/1/1660**	0.43 10^{-5}

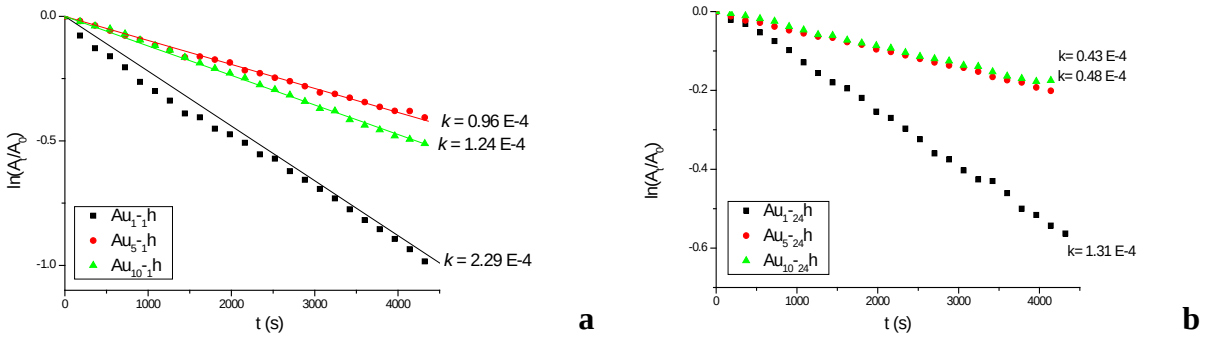

Figure 2.21 Plots of ln(A_t/A_0) versus time for the catalyzed reduction of 4-NP. Reaction conditions: aqueous media at 295 K, with a ratio Au/4-NP/$NaBH_4$ as reported in Table 1S; **a) Au_{x}-$_{1}$h; b) Au_{x}-$_{24}$h.**

Table 2.6 Kinetic constants (k) using fresh (first cycle) and recycled (second to fifth cycles) **Au_{x}-$_{1}$h** catalysts.

use	*first*	*second*	*third*	*fourth*	*fifth*
k (s^{-1}) **Au_{1}-$_{1}$h**	6.84 x 10^{-4}	3.33 x 10^{-4}	2.59 x 10^{-4}	2.50 x 10^{-4}	2.29 x 10^{-4}
k (s^{-1}) **Au_{5}-$_{1}$h**	1.33 x 10^{-4}	0.89 x 10^{-4}	0.86 x 10^{-4}	0.78 x 10^{-4}	0.60 x 10^{-4}
k (s^{-1}) **Au_{10}-$_{1}$h**	3.39 x 10^{-4}	1.14 x 10^{-4}	0.547 x 10^{-4}	0.526 x 10^{-4}	0.343 x 10^{-4}

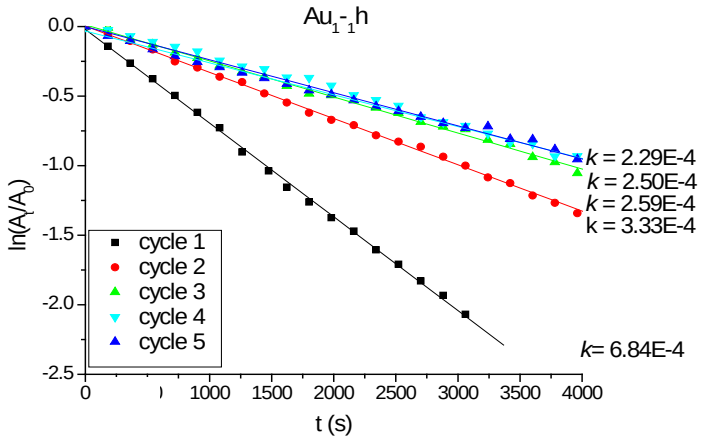

a

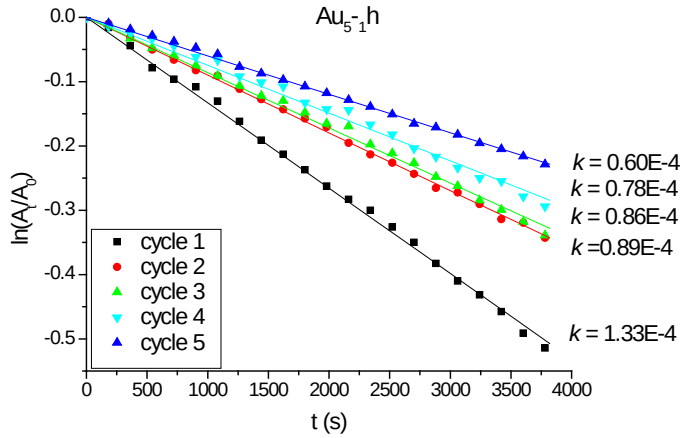

b

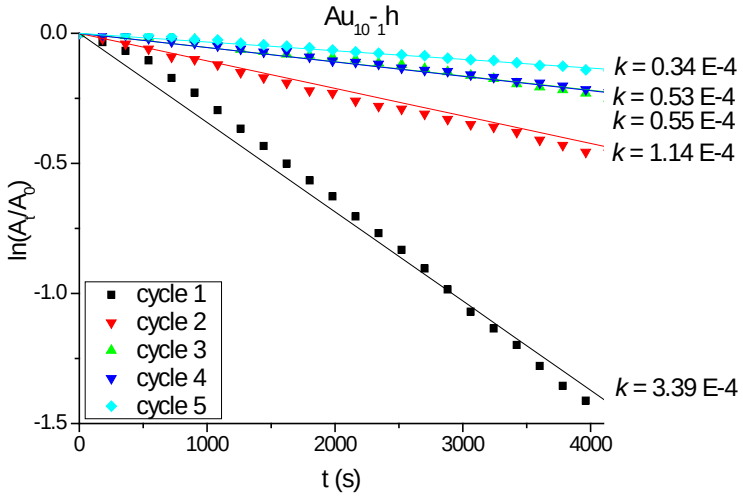

c

Figure 2.22 Plots of ln(A_t/A_0) versus time for the reduction of 4-NP catalyzed by different Au_{NPs}/(SiO_2-PEI) beads after different cycles, as reported in Table 5; **a) Au_1-$_1$h; b) Au_5-$_1$h; c) Au_{10}-$_1$h**. Reaction conditions: aqueous media at 295 K, [4-NP] = 5.19 10^{-2} mM; [$NaBH_4$] = 83 mM, Au = 0.34 µmol.

Furthermore, as reported in Tables 2.2 and 2.3 and Fig. 2.17 of the previous section, the LCF XANES data obtained for **Au_{10}-$_1$h** after the first recycle indicated that in this sample, containing in the pristine form 1/3 of Au(III), the first catalytic cycle in the presence of $NaBH_4$ afforded a 91% conversion (from 67%) of Au(III) to Au(0). This data was also confirmed by the EXAFS analysis which, this time, was successfully fitted with a bulk Au structural model.

2.2 Experimental Section

2.2.1 Materials

$HAuCl_4 \cdot 3H_2O$ was prepared as reported in the literature;[32] ultrapure water purified with the Milli-Q plus system (Millipore Co., resistivity over 18 MΩ cm) was used in all cases. The commercial silica functionalized with polyethylenimine (M_w 75000 – 50000) was purchased from Sigma-Aldrich as orange, 20-60 mesh beads (Figure 1). Sodium borohydride (98%) and 4-nitrophenol (4-NP) are of analytical grade and were purchased from Sigma-Aldrich.

Figure 2.23 Image of a PEI-functionalized SiO_2 commercial sample.

2.2.2 Instruments

2.2.2.1 Characterization of SiO_2-PEI

Thermogravimetric (TGA) measurements coupled with DSC (TG-DSC) were carried out using a Simultaneous Thermal Analyzer, STA 449 C Netzsch Instrument (Selb, Germany). Samples were heated in a platinum crucible in air flow (30 mL min^{-1}) from 20 °C to 1200 °C at a rate of 10 °C/min. The samples weights were in the range 10 mg. Acid-base titration analyses of the amino groups. 0.300 g of SiO_2-PEI were placed in a 20 mL Erlenmayer flask and, after adding 10 mL of 0.05 M solution of HCl, the suspension was stirred for 1 h at room temperature.[33] Then 3 mL of the supernatant were titrated with NaOH 0.05 M to a phenolphtalein endpoint; the analyses were carried out on three different SiO_2-PEI aliquots and repeated twice for each sample. The specific surface area of SiO_2-PEI was analyzed by N_2 adorption/desorption using a Micromeritics ASAP 2020 surface area and porosity analyzer. Surface areas were calculated using the BET equation over the pressure range P/P_0 = 0.02–0.2, where a linear relationship was maintained, while pore-size distributions were calculated using the BJH model up to P/P_0 = 0.95. Sample was degassed under vacuum at 120 °C for at least 2 h prior to analysis.

2.2.2.2 Characterization of Au_{NPs}/(SiO_2-PEI) beads

UV-Vis Diffuse Reflectance Spectroscopy (DR-UV-Vis) analyses of the solid samples were performed on a Perkin Elmer Lambda 19 UV-Vis-Nir spectrometer equipped with a Labsphere diffuse reflectance accessory in the range 400÷800 nm with a scan speed of 240 nm min^{-1} and

treated with the Kubelka-Munk function.[34,35] The respective support of each catalyst was used as a reference.[36]

The amount of gold present on the different samples was determined with a Wavelenghts Dispersive X-Ray Fluorescence (XRF) instrument (Panalytical Axios Advanced) in helium atmosphere by comparison with calibration lines in two ways: i) an indirect method that consist in the analysis of the supernatant solution immediately after the end of the reaction and ii) a direct method in which the solid samples are analyzed after work-up. In the indirect method the calibration lines were prepared making use of aqueous solution containing different amounts of Au(III) salt while the samples were prepared as follows: 3 mL of the supernatant solution were diluted to 10 mL and introduced in a sample cell with a mylar window film of 6 μm in thickness. In the direct method the calibration lines were prepared by incipient impregnation adding aqueous solutions of $KAuCl_4$ to 500 mg of SiO_2-PEI matrix. Successively ca. 200 mg of either calibration or **Au_x-$_y$h** samples were mixed with 0,15 mL of the acrylic resin Elvacite (25 wt% in acetone). After evaporation of acetone the resulting solid was grinded into a fine powder and pelletized into a 13 mm diameter disk. Each analysis is repeated five times. The data obtained with the two methods were identical within the experimental errors however due its ease and speed of execution the indirect method has become the routine method for the determination of the gold loading.

Field Emission-Scanning (FE-SEM) measurements were carried out with a Zeiss SUPRA 40VP instrument at a primary beam acceleration voltage of 10 kV located at the University of Padova; micrographs were collected with an InLens detector. Prior to FE-SEM measurements, samples were coated with 10 nm thick carbon films by a Sputter-Coater (EDWARDS) to avoid charging effects during FE-SEM investigations.

2.2.3 Preparation of Au_{NPs}/(SiO_2-PEI) beads

In a typical procedure, in a 8 mL vial 0.200 g of SiO_2-PEI were added to an aqueous solution (5 mL) of $HAuCl_4 \cdot 3H_2O$ (1 mM, 5 mM, 10 mM). The resulting suspension was stirred at 25 °C with an orbital shaker (IKA, KS 130 basic) at 630 rpm speed for 1 or 24 h. In few minutes the yellow solution turned colourless due to the adsorption of chloroauric acid on SiO_2-PEI. The Au_{NPs}/SiO_2-PEI beads were obtained after filtration on a Buchner funnel, washing with water, and drying under vacuum at 50 °C for 20 h.

2.2.4 XAS Data Collection

XAS spectra were recorded at ELETTRA Synchrotron Radiation Laboratory (Basovizza, Italy). The storage ring was operated at 2.0 GeV in top up mode with a typical current of 300 mA. The data were recorded at Au L_{III} edge in transmission mode using ionization chamber filled with a mixture of Ar, N_2 and He in order to have 10%, 70%, and 95% of absorption in the I_0, I_1, and I_2 chambers, respectively. The white beam was monochromatized using a fixed exit monochromator equipped with a pair of Si(111) crystals. Harmonics were rejected by using the cutoff of the reflectivity of the Platinum mirror placed at 3 mrad with respect to the beam upstream the monochromator. The precursor Au(III) sample was recorded on a 10 mM solution of $HAuCl_4$ using a suitable cell for liquids, whereas Au_{NPs}/SiO_2-PEI catalysts samples were solid pellets, prepared by mixing the material with cellulose filler. The energies were defined by assigning to 11919 eV the first inflection point of the spectrum of the gold foil. Spectra were collected in sequence and recording Au reference foil before each sample. This allowed a continuous monitoring of the energy during consecutive scans. No energy drifts of the monochromator were observed during the experiments. Spectra were collected with a constant k-step of 0.03 $Å.^{-1}$ with 3 s/point acquisition time from 11730 eV to 12900 eV.

2.2.4.1 XAS Data Analysis

X-Ray Absorption Spectroscopy spectra were calibrated using the Athena program.[37] The pre-edge background was removed by subtraction of a linear function extrapolated from the pre-edge region, and the X-Ray Absorption Near Edge Structure (XANES) spectra were normalized at the unity by extrapolation of the atomic background as it is comes out from the Extended X-Ray Absorption Spectroscopy (EXAFS) analysis (evaluated using a polynomial function).

The EXAFS analysis was performed by using the GNXAS package that takes into account Multiple Scattering (MS) theory.[38,39] The method is based on the decomposition of the EXAFS signals into a sum of several contributions, that are the n-body terms. The theoretical signal is calculated *ab-initio* and contains the relevant two-body $\gamma(2)$ and three-body $\gamma(3)$ multiple scattering (MS) terms. The contribution from the four-body $\gamma(4)$ terms[40] was checked out, but it was found to be negligible. The structural model has been chosen to be the Au(0) bulk.[41] The Hedin-Lundqvist complex potential was used for the exchange-correlation potential of the excited state.[42] The core whole lifetime, Γ_c, was fixed to the tabulated value and included in the phase shift calculation.[43] The experimental resolution used in the fitting analysis was about 2 eV, in agreement with the stated value for the beam line used. The relevant E_0 values were found to be displaced by several

eV with respect to the edge inflection point. The fitting was done by keeping fixed the value of the S_0^2 to 0.85.

2.2.5 Catalytic reduction of 4-nitrophenol (4-NP)

The catalytic activity of the six Au_{NPs}/SiO_2-PEI samples was examined in the reduction of 4-NP to 4-AP in the presence of an excess of $NaBH_4$ at 25 °C. As showed in Figure 18Sa, the absorption of 4-NP occurs at λ_{max} 317 nm and, after addition of $NaBH_4$, undergoes a red shift to 400 nm corresponding to the formation of the 4-nitrophenolate anion. In the absence of catalyst this peak remained unaltered whereas the addition of an aliquot of Au_{NPs}/SiO_2-PEI to the reaction system caused a fading and ultimate bleaching of the yellow-green colour of the 4-nitrophenolate ion, with a decrease of the absorption at 400 nm and the concomitant appearance of a new peak at 295 nm attributed to the generation of 4-aminophenolate ion (Figure 2.24).[44,45,46]

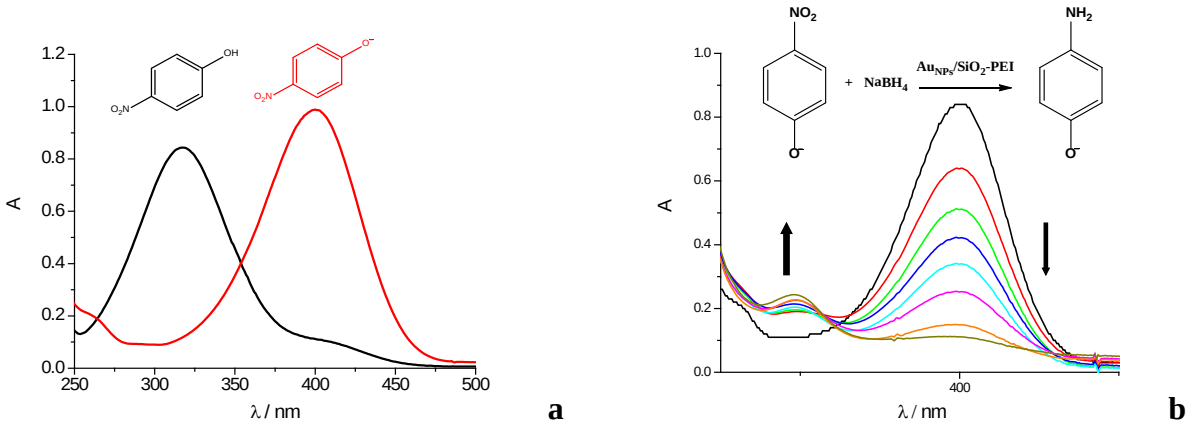

Figure 2.24 a) UV-Vis spectra of 4-NP before (black line) and after (red line) adding the $NaBH_4$ solution; **b)** UV-Vis spectra of 4-NP reduction in the presence of excess $NaBH_4$ over catalyst Au_{NPs}/SiO_2-PEI.

Typically, in a 50 mL pyrex glass vial 15 mL of a $9.0 \cdot 10^{-2}$ mM aqueous solution of 4-NP were mixed with 8 mL of water and 3 mL of a freshly prepared $NaBH_4$ solution (0.72 M). The catalytic reduction was carried out by putting 3 mL of the resulting solution (containing 0.15 µmol of 4-NP and 200 µmol of $NaBH_4$) and an appropriate amount of catalyst in a standard quartz cuvette (1 cm path length). The optical spectra of the suspensions were recorded with a single beam Hewlett-Packard 8453 diode array spectrophotometer in the spectral range 250÷500 nm. The rate constants *k* of the reduction process were determined through measuring the change in absorbance at 400 nm. Since the absorbance of 4-NP is proportional to its concentration in the medium, the ratio of absorbance at time *t* (A_t) to that at *t* = 0 (A_0) can be used as the concentrations ratio. As the concentration of $NaBH_4$ largely exceeds that of 4-NP, the reduction rate can be assumed to be

independent of the concentration of borohydride, with a pseudo-first order rate kinetics with regard to the 4-NP concentration. The plot of $\ln(A_t/A_0)$ *vs* time was obtained as a straight line whose slope, in absolute value, is the kinetic constant *k*. Each catalyst was synthesized twice and the catalytic activity evaluated by repeating the measurements three times. The catalytic performances of recycled **Au_x-$_1$h** samples were tested sequentially for five times. Before reusing it, the recycled catalyst was washed three times with abundant water and a 0.3 M solution of sodium carbonate in order to favour removal of borates and residual reaction products.

2.3 Conclusions

In summary, we have shown that commercially available SiO_2-PEI can be a convenient, cheap support/reagent for preparing supported Au_{NPs} in a very straightforward way and without any need for either external reductants or conventional stabilizing agents. The resulting materials can behave like heterogeneous catalysts that, despite the needed excess of metal, can show activities comparable with those reported in the literature for similar systems and can be efficiently recycled without major loss of their catalytic activity.

References

[1] X. Xu, C. Song, J. M. Andresen, B. Miller, A. W Scarni, *Microporous Mesoporous Mater*. **2003**, *62*, 29.

[2] Bon, P.; Zhitomirsky, I.; Embury, J. D. *Surf. Eng*. **2003**, *20*, 5.

[3] Gergbreiter, D.; Simanek, E. E.; Owsik, I. *J. Polym. Sci. Part A* **2005**, *43*, 46.

[4] K.S.W. Sing, D.H. Everett, R.A.W. Haul, L. Moscou, R.A. Pierotti, J. Rouquérol, T. Siemieniewska, *Pure & Appl. Chem.* **1985**, 57, 603.

[5] Q. Chen, F. Fan, D. Long, X. Liu, X. Liang, W. Qiao, L. Ling, *Ind. Eng. Chem. Res.* **2010**, *49*, 11408.

[6] D. Lin-Vien, N. B. Colthup, W. G. Fateley, J. Grasselli, Eds., *The Handbook of Infrared and Raman Characteristic Frequencies of Organic Molecules*, Academic Press, New York, **1991**.

[7] B. Gao, Y. Li, Z. Chen, *Chem. Eng. J*. **2009**, *150*, 337.

[8] A. B. R Mayer, J. E. Mark, *Angew. Makromol. Chem.* **1999**, *268*, 52.

[9] K. Kim, H. B. Lee, J. W. Lee, K. S. Shin, *J. Colloid Interface Sci.* **2010**, *345*, 103.

[10] Eustis, S.; El-Sayed, M. A. *Chem. Soc. Rev*. **2006**, *35*, 209-217.

[11] Sepúlveda, B.; Angelomé, P. C.; Lechuga, L. M.; Liz-Marzán, L. M. *Nano Today* **2009**, *4*, 244-251.

[12] *ImageJ*, Image processing and analysis in Java: http://rsb.info.nih.gov/ij/.

[13] Benfield, R. E.; Filipponi, A.; Bowron, D. T.; Newport, R. J.; Gurman, S. J. *J. Phys.: Condens. Matter* **1994**, *6*, 8429-8448.

[14] Lu, Z. H.; Sham, T. K.; Vos, M.; Bzowski, A.; Mitchell, I. V.; Norton, P. R. *Phys. Rev. B* **1992**, *45*, 8811.

[15] B. Abécassis, F. Testard, Q. Kong, B. Francois, O. Spalla, *Langmuir* **2010**, *26*, 13847.

[16] J. L. Gardea-Torresdey, K. J. Tiemann, J. P. Parsons, G. Gamez, I. Herrera, M. Jose-Yacaman, *Microchem. J*. **2002**, *71*, 193.

[17] K. Paclawski, D. A. Zajac, M. Borowiec, C. Kapusta, K. Fitzner, *J. Phys. Chem. A* **2010**, *114*, 11943.

[18] R. E. Benfield, D. Grandjean, M. Kröll, R. Pugin, T. Sawitowski, G. Schmid, G. *J. Phys. Chem. B* **2001**, *105*, 1961-1970.

[19] J. L. Gardea-Torresdey, K. J Tiemann, J.P Parsons, G. Gamez, I. Herrera, M. Jose-Yacaman, M. *Microchem. J*. **2002**, *71*, 193-204.

[20] A. I. Frenkel, C. W Hills, R. G. Nuzzo, *J. Phys. Chem. B* **2001**, *105*, 12689.

[21] B. Liu, W. Zhang, H. Feng, X. Yang, *Chem. Commun.* **2011**, *47*, 11727.

[22] S. Panigrahi,; S. Basu, S. Praharaj, S. Pande, S. Jana, S.; Pal, A.; Ghosh, S. K.; Pal, T. *J. Phys. Chem. C* **2007**, *111*, 4596.

[23] B. Ballarin, M. C. Cassani, D. Tonelli, E. Boanini, S. Albonetti, M. Blosi, M. Gazzano, *J. Phys. Chem. C* **2010**, *114*, 9693-9701.

[24] G. Braurer, G. *Handbook of Preparative Inorganic Chemistry*, Academic Press, New York, **1963**, Vol. II, 1058

[25] K. Kuroda, T. Ishida, M. Haruta, *J. Mol. Catal. A* **2009**, *298*, 7-11.

[26] K.S.W. Sing, D.H. Everett, R.A.W. Haul, L. Moscou, R.A. Pierotti, J. Rouquérol, T. Siemieniewska, *Pure & Appl. Chem.* **1985**, 57, 603.

[27] X. Huang, X Liao, B. Shi, *Green Chem.* **2011**, *13*, 2801.

[28] Schrinner, M.; Polzer, F.; Mei, Y.; Lu, Y.; Haupt, B.; Ballauff, M.; Göldel, A.; Drechsler, M.; Preussner, J.; Glatzel, U. *Macromol. Chem. Phys.* **2007**, *208*, 1542-1547.

[29] J. Liu, G. Qin, P. Raveendran, Y. Ikushima, *Chem. Eur. J.* **2006**, *12*, 2131.

[30] S. Panigrahi, S. Basu, S. Praharaj, S. Pande, S. Jana, A. Pal, S. K Ghosh, T. Pal, *J. Phys. Chem. C* **2007**, *111*, 4596.

[31] C. Gao, W. Li, Y. Z. Jin, H. Kong *Nanotechnology* **2006**, *17*, 2882.

[32] G. Braurer, *Handbook of Preparative Inorganic Chemistry*, Academic Press, New York, 1963, Vol. II, 1058.

[33] D. Gergbreiter, E .E Simanek, I. Owsik, *J. Polym. Sci. Part A: Polym Chem.*, **2005**, 43, 46.,54.

[34] M. P. Fuller, P. R. Griffiths, *Anal. Chem.* **1978**, *50*, 1906-1910.

[35] Pere, E.; Cardy, H.; Cairon, O.; Simon, M.; Lacombe, S. *Vib. Spectrosc.* **2001**, *25*, 163-175.

[36] C. L. Peza-Ledesma, L. Escamilla-Perea, R. Nava, B. Pawelec; J. L. G. G. Fierro, *App. Catal. A* **2010**, *375*, 37-48.

[37] B. Ravel, M. Newville, *ATHENA, ARTEMIS, HEPHAESTUS:* Data Analysis for X-ray Absorption Spectroscopy Using IFEFFIT. *J. Synchrotron Radiat.* **2005**, *12*, 537.

[38] A. Filipponi, A. DiCicco, C. R. Natoli, C. R. *Phys. Rev. B* **1995**, *52*, 15122.

[39] A. Filipponi, A., A. DiCicco, *Phys. Rev. B* **1995**, *52*, 15135.

[40] M. Giorgetti, M. Berrettoni, A. Filipponi, P. J Kulesza, R. Marassi, *Chem. Phys. Lett.* **1997**, *275*, 108.

[41] The metallic Au has a typical *ccp* structure with the cell parametes a = 4.0782 Å (Space group: *Fm-3m*, #225).

[42] L. Hedin, B. I. Lundqvist, *J. Phys. C*: *Solid State Phys.* **1971**, *4*, 2064.

[43] M. O. Krause, J. H. Oliver, *J. Phys. Chem. Ref. Data* **1979**, *8*, 329.

[44] B. Ballarin, M. C. Cassani, , D. Tonelli, E. Boanini, S. Albonetti, M. Blosi, M. J. Gazzano, *Phys. Chem. C* **2010**, *114*, 9693.

[45] K. Kuroda, T. Ishida, M. Haruta, *J. Mol. Catal. A* **2009**, *298*, 7-11.

[46] X. Huang, X. Liao, B. Shi, *Green Chem.* **2011**, *13*, 2801.

CHAPTER 3 64

3 SYNTHESIS OF SUPPORTED GOLD NANOPARTICLES BY FUNCTIONALIZED SILICA NANOPARTICLES 64

3.1 Results and Discussion 65

3.1.1 Alkyne-functionalized silica nanoparticles (SiO_2@Yne) 65
3.1.2 Thiol-yne functionalized silica nanoparticles (SiO_2@Thio-Yne) 76
3.1.3 Au_{NPs} supported by SiO_2@Yne (Au-SiO_2@Yne) 87
3.1.4 Au_{NPs} supported by SiO_2@Thio-Yne (Au- SiO_2@Thio-Yne) 95

3.2 Conclusions 102

3.3 Experimental Section 103

3.3.1 Materials 103
3.3.2 Synthesis of [3-(2-Propynylcarbamate)propyl]triethoxysilane 103
3.3.3 General preparation of Alkyne-Functionalized Silica Nanoparticles (SiO_2@Yne) 104
3.3.4 Thiol-yne reaction on with propargyl alcohol and cysteamine hydrochloride 105
3.3.5 General method to prepare SiO_2@Thio-Yne 105
3.3.6 Synthesis of Au-SiO_2@Yne and Au-SiO_2@Thio-yne 106
3.3.7 Characterization 106

3.4 Appendix 108

3.4.1 SiO_2@Thio-Yne Thermograms 108
3.4.2 NMR and ES-MS spectra 110
3.4.3 XPS DATA 111
3.4.4 FT-IR 113

CHAPTER 3

3 Synthesis of supported gold nanoparticles by functionalized silica nanoparticles

This section illustrates a convenient method to prepare functionalized silica nanoparticles for the *in situ* reduction of the $HAuCl_4$ precursor. The silica nanoparticles were prepared by co-condensation of tetraethoxysilane and an alkyne-terminated organosilane (**SiO_2@Yne**), followed by post-functionalization by thiol-yne coupling (TYC) with cysteamine **(SiO_2@Thiol-yne**) (Fig. 3.1).

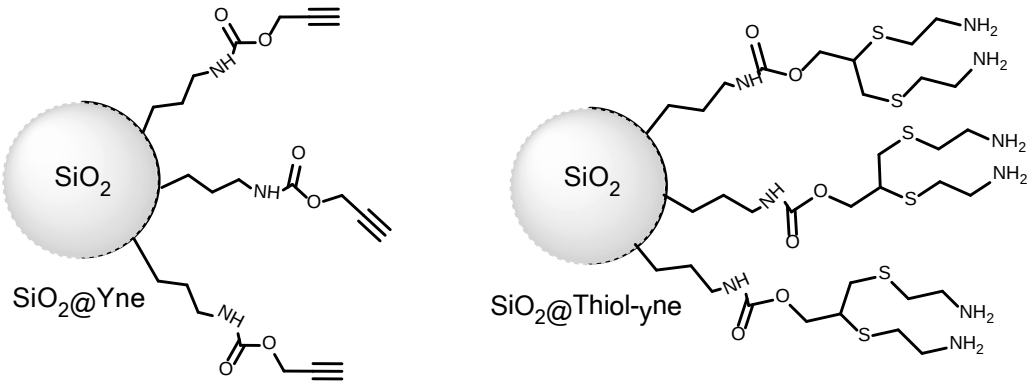

Figure 3.1 Alkyne-modified silica nanoparticles **SiO_2@Yne** and **SiO_2@Thio-Yne**.

The behaviour of these composite-silica nanoparticles will be presented and discussed.

3.1 Results and Discussion

3.1.1 Alkyne-functionalized silica nanoparticles (SiO_2@Yne)

3.1.1.1 Synthesis of SiO_2@Yne

The alkyne-terminated organosilane prop-2-yn-1-yl (3-(triethoxysilyl)propyl)carbamate (PPTEOS) **3** was synthetized following a published procedure[1] by a simple one-step addition of **2** to **1** catalyzed by triethylamine (TEA)[2]. PPTEOS was isolated after elimination of the volatiles under reduced pressure and was used without further purification (Scheme 3.1).

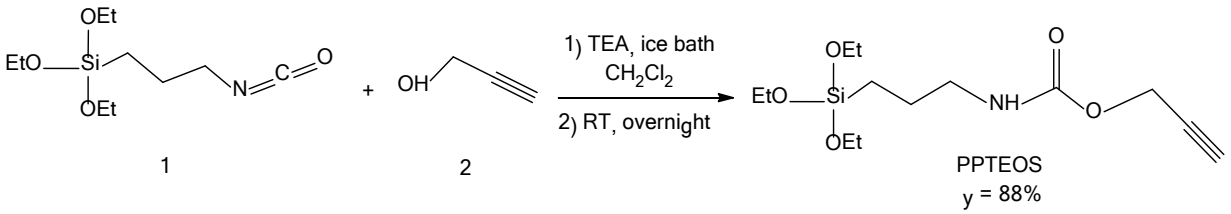

Scheme 3.1 Synthesis of PPTEOS.

PPTEOS is a polyfunctional organosilane with an alkyne moiety at the non-condensable end and three ethoxy groups (linked to the silicon atom) that can be hydrolyzed under basic conditions and undergo a condensation reaction with tetraethoxysilane (TEOS). By one-pot hydrolytic condensation of PPTEOS with TEOS in basic medium (NH_4OH, 28 % v/v) at 40 °C, the alkyne functionality was hence introduced into the SiO_2 network (**SiO_2@Yne**), using a modified reported procedure (Scheme 3.2).[3]

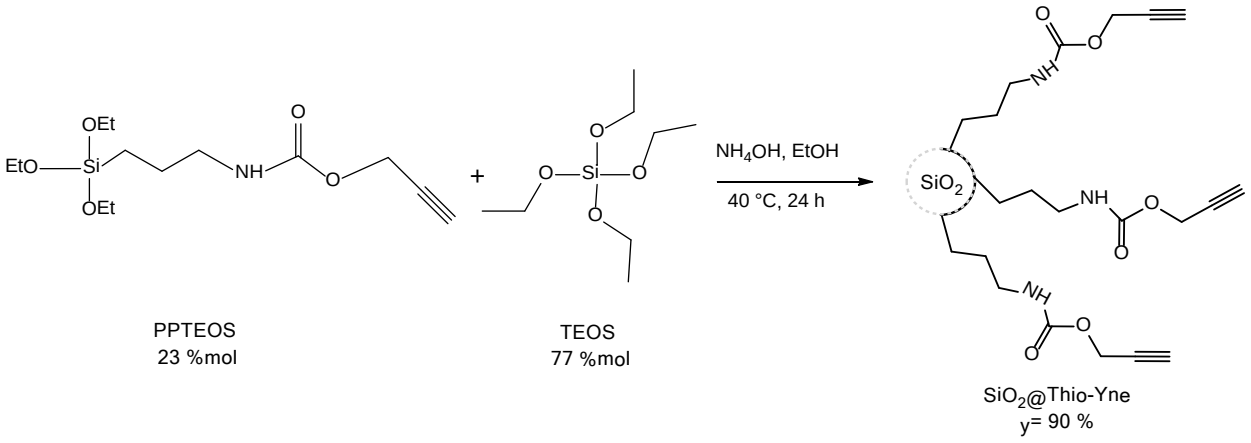

Scheme 3.2 Synthesis of alkyne-modified silica nanoparticles **SiO_2@Yne**.

Two kinds of **SiO_2@Yne** were prepared: **SiO_2@Yne-a** and **SiO_2@Yne-b**. The former was obtained by adding 10 mL of NH_4OH in the sol-gel preparation, leading to a 2.2 M final concentration in NH_4OH. The latter was instead obtained using 3.4 mL of NH_4OH with a final concentration of 0.8 M. After the addition, the mixture becomes gradually milky white, which corresponds to silica nanoparticles formation. In the case of **SiO_2@Yne-a** this phenomenon was evident after 2 minutes, whereas for **SiO_2@Yne-b** it was observed only after two hours. At the end of the reaction the alkyne-modified silica nanoparticles (**SiO_2@Yne-a** or **b**) were isolated by centrifugation, removed from the supernatant, and purified by cycles of re-dispersion, centrifugation, and washing in ethanol (see experimental part). The purified ethanol dispersions of **SiO_2@Yne-a** or **b** were concentrated under reduced pressure and dried at 50 °C, obtaining white powders easily redispersible in ethanol, with a yield of ca. 90 % for both samples. The bare silica nanoparticles (**bare-SiO_2**) were prepared by the same procedure using TEOS without addition of PPTEOS.

The removed supernatant of **SiO_2@Yne-a** and **b** was concentrated under reduced pressure, analyzed and weighed in order to have an indication of the functionalization degree before Thermo Gravimetric Analysis (TGA) results. The presence of unreacted PPTEOS, confirmed by NMR analysis, was always found. In both syntheses, an initial amount of 23 mol % was used (Scheme 3.2) but it was found that only 6 mol % of it reacted with TEOS in the case of **SiO_2@Yne-a,** and 4 mol % for **SiO_2@Yne-b.** These results are in agreement with the percentage of weight losses measured by TGA and the relative composition obtained by X-Ray Photoelectron Spectroscopy (XPS).

In the original publication of *Lu et al.*[3] variable amounts of PPTEOS were added to a mixture of ammonia and TEOS at room temperature after 30 minutes from the addition of TEOS in order to pre-form the silica nuclei and anchor the alkyne functionality in the exterior surface. The effect of the three PPTEOS concentrations (5, 10, and 15 mol %) on the final size of the nanoparticles was studied, leading to nanoparticles having diameters of 160, 150, and 140 nm, respectively. In that article the authors never mentioned that only a partial amount of PPTEOS reacts in the condensation and the characterization was carried out directly on the functionalized silica. Nevertheless, the reported weight percentage (weight of organic material fraction %, measured by TGA) was ca. 4 wt % (without the contribution of silica). This value is clearly indicative of a partial condensation of PPTEOS with TEOS, as a load of 10 mol% PPTEOS would correspond, for a quantitative conversion, to an estimated weight percentage around 20 wt %.It was evident that the changes in size observed in the article are not justified by the total PPTEOS functionalization, and

also the difference of 10 nm between each synthesis is not relevant, considering that systems like those are generally affected by slight polydispersity. [1]

In our studies the reaction was initially performed by adding PPTEOS after 30 minutes at 45 °C. Under these conditions a higher incorporation of the organic fraction was observed (ca. 12 wt %) with the simultaneous formation of a mixture of big aggregates (mainly made of **bare-SiO_2**) and small nanoparticles (mainly **SiO_2@Yne**). Successively, taking into account these results, the two organosilanes were added together at 40 °C, hence obtaining exclusive formation of highly functionalized **SiO_2@Yne** nanoparticles. **SiO_2@Yne** were characterized by dynamic light scattering (DLS), transmission electron microscope (TEM), thermogravimetric analysis (TGA), phoelectron X-ray Spectroscopy (XPS), and UV-Vis spectrophotometric analysis.

3.1.1.2 Characterization of SiO_2@Yne

TEM and DLS characterization

The size of the above alkyne-modified nanoparticles, as well as of that of the **bare–SiO_2**, were determined by TEM and DLS measurements.

TEM images showed a spherical geometry for both samples, with an average size of 79 ± 24 nm for **SiO_2@Yne-a** (higher NH_4OH concentration) (Fig. 3.2 a) and 45 ± 6 nm for **SiO_2@Yne-b** (lower NH_4OH concentration) (Fig. 3.1 b), resepctively, where the average size was measured by counting 100 nanoparticles from TEM images by the ImageJ software.[4] We can observe that by increasing the NH_4OH concentration larger nanoparticles are obtained, according to Stöber results.[5] The ammonia concentration, in fact, directly influences both hydrolysis and condensation rate, which can be easily distinguished because, after hydrolysis, condensation occurs with an increasing opalescence of the mixture. As mentioned before, the appearance of a milky white colour starts for **SiO_2@Yne-a** samples after two minutes, whereas for **SiO_2@Yne-b** only after two hours. In the first case, high ammonia concentration quickly hydrolyses the precursor, with fast formation of silicic acid, and rapid nucleation occurs. When the nucleation process continues with the concomitant growth of the pre-existing nuclei, polydisperse systems are obtained. In **SiO_2@Yne-a**, nanoparticles with an average diameter of 79 nm are present, but the presence of a small population with an average size of ca. 150 nm is also visible (Fig. 3.2 a). Otherwise, more monodispersed systems are

[1] During hydrolysis, PPTEOS replaces three ethoxy groups by OH and, during condensation, it loses an average of two oxygens by condensation with TEOS (with formation of water) with a final molecular weight of ca. 184 g/mol; by condensation, TEOS goes from a molecular weight of 208 to 60 g/mol: assuming that 10 %mol of PPTEOS react, the weight percentage is obtained by the following calculation: g PPTEOS = 10 mmol*184 g/mol = 1.8 g; TEOS 90 mmol*60g/mol = 5.4 g; weight percentage = 1.8/(1.8+5.4) *100 = 23.6 %.

obtained in **SiO_2@Yne-b**. In this sample the slow hydrolysis resulted in smaller nanoparticles with an average diameter of 45 nm (Fig. 3.2 b). In all samples, a raspberry-like structure was found, as shown by the enlargement of one portion of the TEM micrograph in negative mode (Figs. 3.3 a and b). TEM analysis performed on different batches showed a good reproducibility of size and morphology.

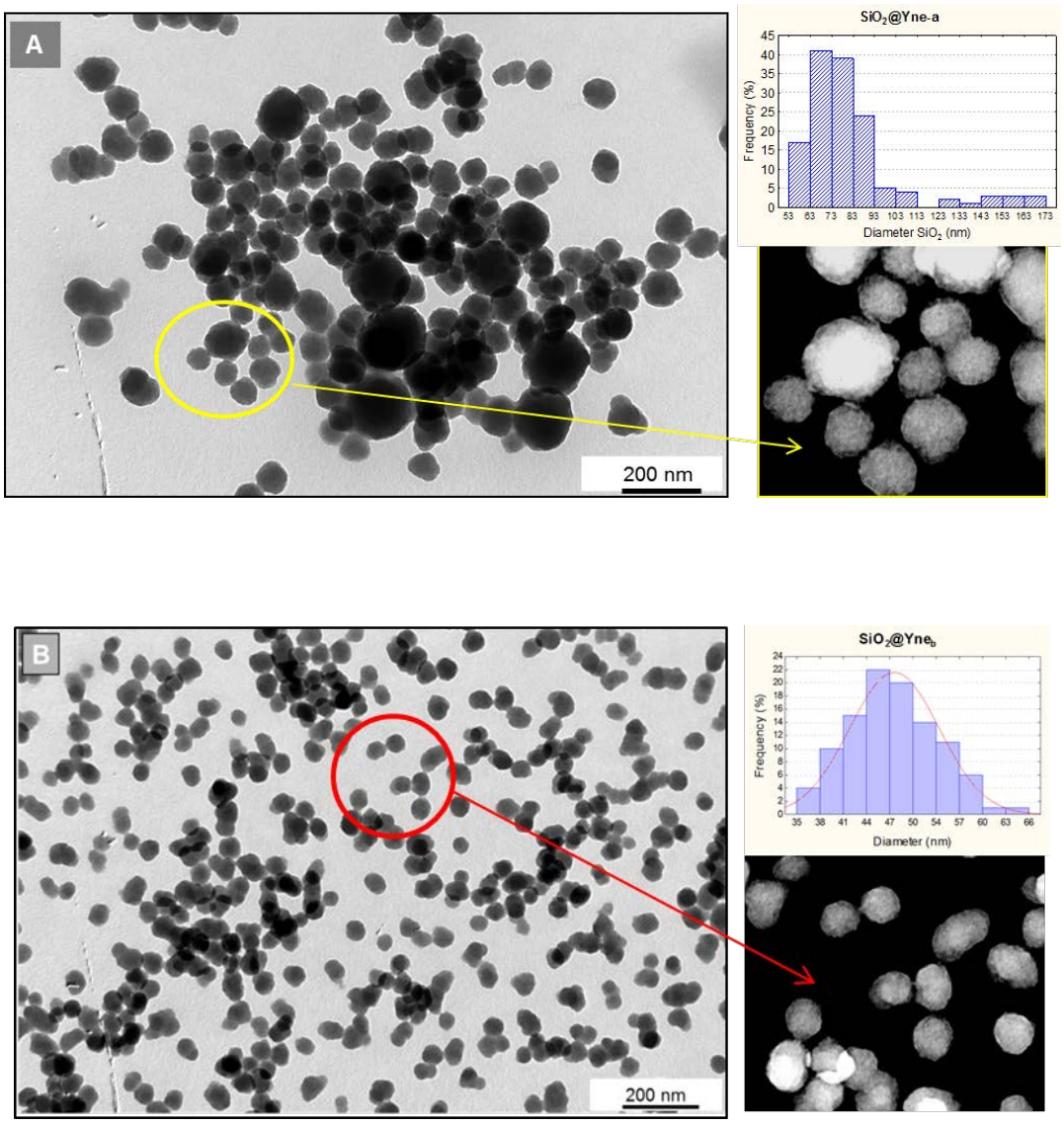

Figure 3.2 TEM image, size distribution, and enlargement of one area in negative mode. **a) SiO_2@Yne-a; b) SiO_2@Yne-b**.

Bare-SiO_2 obtained under the same conditions employed for **SiO_2@Yne-a** had an average size of 367 ± 32 nm, that is almost three times larger than the modified silica. A comparison of the two TEM micrographs on the same scale is reported in Fig. 3.3. This difference in dimensions between **SiO_2@Yne** and **bare-SiO_2** can be explained in terms of lack of propagating alkoxy groups

in **SiO_2@Yne-a** during the hydrolysis step, which hinders particles growth and, in turns, leads to a decrease in size.[6]

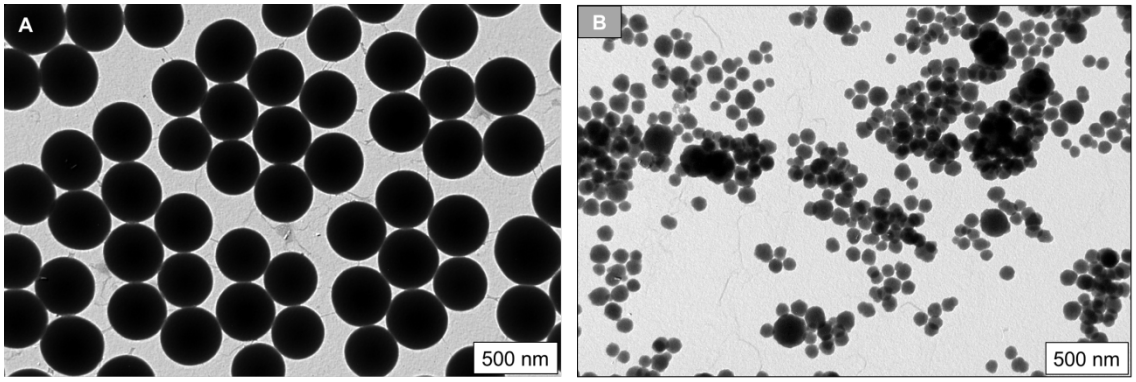

Figure 3.3 TEM images of **(a) SiO_2-bare-a** (367 ± 32 nm); **(b) SiO_2@Yne-a** 79 ± 24.

DLS analysis takes into account the interactions between the solvent and the molecules on the silica surface. Accordingly, the hydrodynamic radii found for all samples were larger than those measured by TEM. TEM and DLS results are summarized in Table 3.1.

Table 3.1 DLS and TEM results of **SiO_2@Yne-a** and **b**.

Sample	DLS (nm)	TEM (nm)
Bare-SiO_2	441	367 ± 32
SiO_2@Yne-a	145	79 ± 24
SiO_2@Yne-b	90	45 ± 6

TGA analysis

Thermogravimetric measurements (TGA) with a temperature profile from 20 °C to 900 °C and heating rate of 10 °C min^{-1} were performed in order to quantify the weight loss (wt %) of organic material present in **SiO_2@Yne-a** and **SiO_2@Yne-b**. For comparison the TGA of **bare-SiO_2** was also performed (Fig. 3.4). In all TGA thermograms (red line) a weight loss of 5 - 6 wt % from 30 to 140 °C is present and was ascribed to desorption of water and ethanol.

The weight loss (5%) in **bare-SiO_2** between 400 – 700 °C was mainly attributed to the presence of not hydrolyzed alkoxy groups, dehydration of the Si-OH groups, and ethanol molecules trapped in the silica matrix. This weight loss value (5 wt %) is in accordance with analogous results found in the literature for silica nanoparticles. [7]

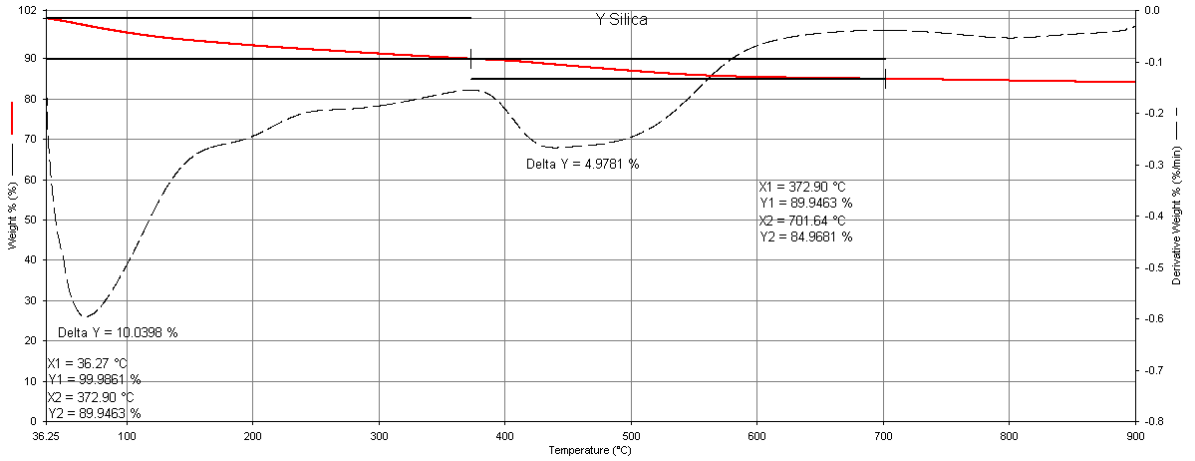

Figure 3.4 TGA curves (continuous red line) and the first derivatives (dashed line) of the weight loss a) **SiO_2@Yne-a** and b) **SiO_2@Yne-b**.

In both **SiO_2@Yne-a** and **SiO_2@Yne-b** an additional weight loss in the range from 200 °C to 500 °C with a maximum loss (evidenced by the first derivatives) at 290 °C was observed and assigned to the decomposition of PPTEOS (Fig. 3.5 a and b). By subtracting the loss in weight obtained for bare-silica (5 wt %) from the total weight loss in the range 170 - 700 °C, an indicative weight % of the alkyne-organosilane incorporated is given as 10 % and 9 % for **SiO_2-Yne-a** and **SiO_2-Yne-b**, respectively (Table 3.2). These results confirm the successful incorporation of the alkyne functionalization to silica and the obtained data are consistent with the expected weight percentage from the evaluation of the reacted PPTEOS.

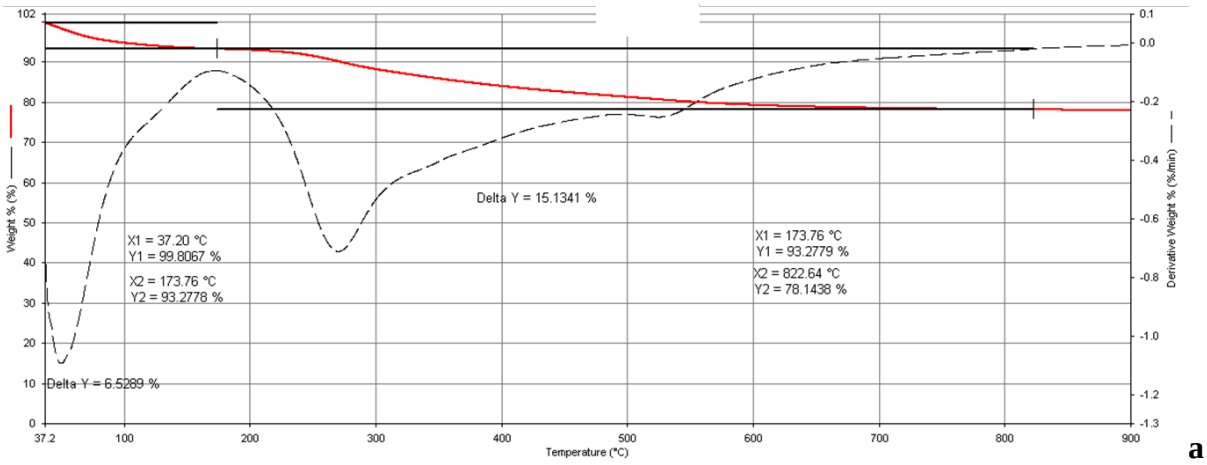

a

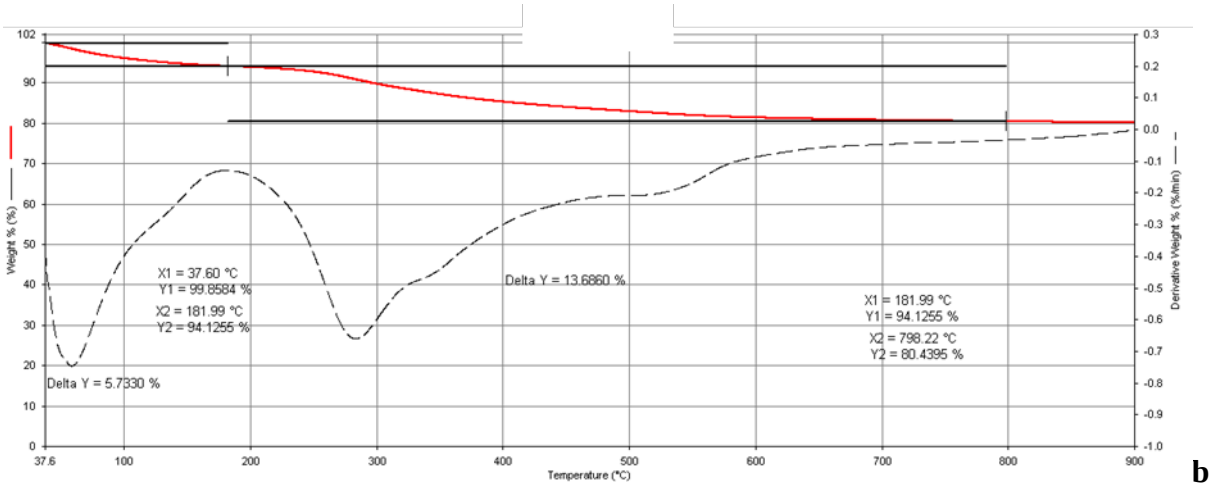

Figure 3.5 TGA curves (continuous red line) and weight percentage first derivatives (dashed line) of **a) SiO_2@Yne-a** and **b) SiO_2@Yne-b.**

Table 3.2 shows the wt % values obtained by TGA analysis, with the estimated value by the amounts of unreacted PPTEOS in the supernatant (see paragraph 3.1.1).

Table 3.2 Comparison of TGA results in **SiO_2@Yne-a** and **SiO_2@Yne-b.**

Samples	TGA (%)[a] Total	TGA (%)[b] Excluded water	TGA (%)[c] Anchored Alkyne	TGA (%)[d] Estimated
Bare-SiO_2	15	5	-	-
SiO_2@Yne-a	22	15	10	13
SiO_2@Yne-b	19	14	9	11

The error associated to the instrument is 1 %.
[a]Total wt % loss;
[b] Total wt % loss excluding water;
[c] Wt % loss associated to PPTEOS anchored on silica: total wt % excluding water and silica contribution.
[d] Wt % loss of PPTEOS incorporation estimated by the unreacted PPTEOS in the supernatant solution.

FT-IR analysis

SiO_2@Yne-a and **SiO_2@Yne-b** FT-IR spectra (Fig. 3.6) exhibit a weak absorption peak at 2131 cm^{-1} ascribed to the alkyne moieties, which confirms the incorporation of PPTEOS on silica, like already evidenced by TGA, TEM, and DLS results compared with **bare-SiO_2**.

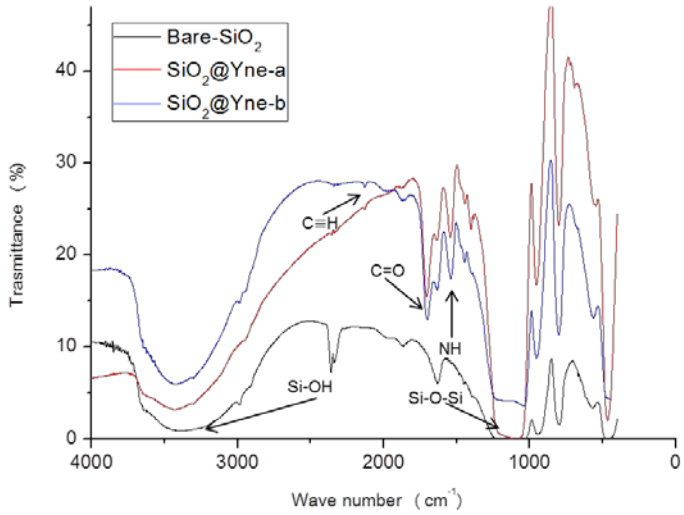

Figure 3.6 Comparison of FT-IR spectra of **SiO_2@Yne-a** (red line), **SiO_2@Yne-b** (blue line) with **bare-SiO_2** (black line).

By comparison of **bare-SiO_2** and **SiO_2@Yne** spectra, the bands ascribed to the SiO_2 network are distinguishable. The strong absorption bands are due to the stretching and bending vibrations of SiOH (3429 cm^{-1}), Si-O-Si (1090 cm^{-1}), and hydrogen-bonded SiOH groups (1635 cm^{-1}). The weak CH_2 and CH_3 vibrations at 2977 cm^{-1} and 2875 cm^{-1} in bare-SiO_2 spectra indicate that there may be some unreacted ethoxy groups of the silane present on the surface. The same bands are present in the **SiO_2@Yne** samples, mainly in **SiO_2@Yne-b.**

SiO_2@Yne-a and **SiO_2@Yne-b** showed the same bands: a band at 3293 cm^{-1} ascribed to C≡CH stretching vibrations (ν_s), one at 1707 cm^{-1} due to ν_s(C=O), and another at 1538 cm^{-1} assigned to NH bending vibrations, according to the literature.[8]

In the Raman spectra, the following bands were observed: the stretching vibration peaks of Si-O-Si at 483 cm^{-1}, the O-H stretching of silica at 3313, 3454, 3602 cm^{-1}, the symmetric (2894 cm^{-1}) and asymmetric (2957 cm^{-1}) stretching of CH_3 groups, and the weak stretching vibration at 1707 cm^{-1} ascribed to C=O (Fig. 3.7). The intense absorption peak at 2122 cm^{-1} supports the presence of C≡CH units on silica.

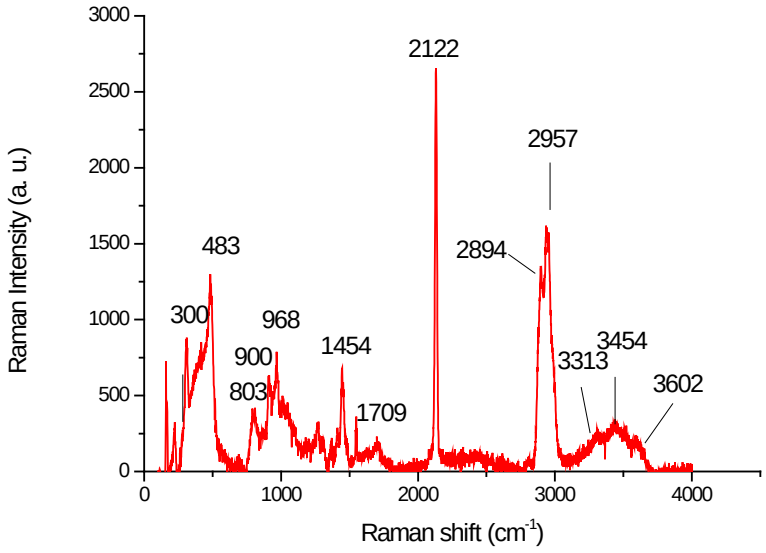

Figure 3.7 Raman spectra of **SiO_2@Yne.**

XPS analysis ***SiO_2@Yne***

The surface functionalization of the **SiO_2@Yne** was analyzed by XPS. This technique gives evidence of the relative composition in the first ten nanometers of surface, hence providing insights into the identity of the functional groups present on the surface. X-ray photoelectron (XP) spectra afford the relative frequencies of binding energies (BEs) of the electrons detected, measured in electron-volts (eV). The binding energies are used to identify the elements to which the peaks correspond. While comparing the areas under the peaks, a relative percentages of the elements in the sample are detected, with an error of ca. 5 % mol. Elements of the same kind in different oxidation states and environments have slightly different characteristic binding energies. Computer software is used to fit peaks within the elemental peak which represent different states of the same element, commonly called deconvolution of the elemental peak.

The survey XPS spectra of **SiO_2@Yne-a** and **SiO_2@Yne-b** are reported in Fig. 3.8, which shows all of the detectable elements present in the samples.

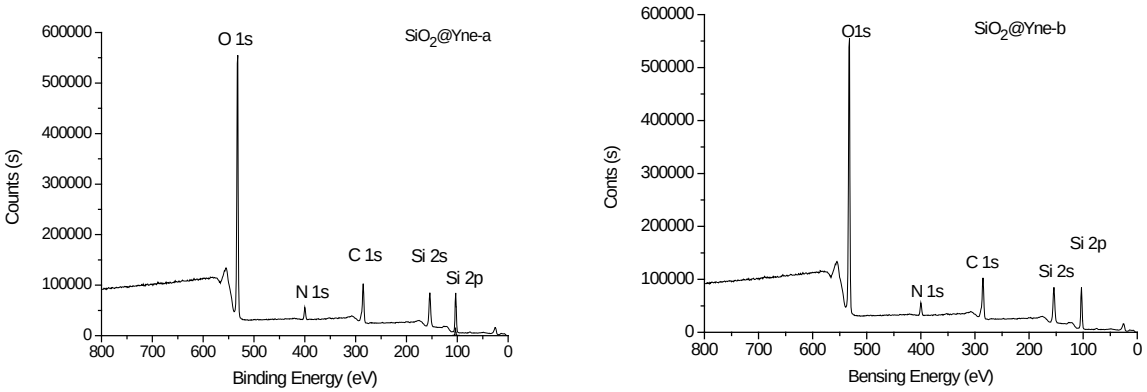

Figure 3.8 XPS survey spectra of **a) SiO_2@Yne-a**; **b) SiO_2@Yne-b**

The relative elemental compositions and the energies of the samples are reported in Table 3.3. It is worth noting that, in addition to silicon and oxygen, carbon and nitrogen, belonging to the organic functionalization, are also present. Table 3.3 shows that there are no significant differences (within the experimental error) between **SiO_2@ Yne-a** and **SiO_2@ Yne-b.**

Table 3.3 XPS spectral relative elemental composition.

Samples	Si 2p (at %) 103.3 ± 0.1 (eV)	O 1s (at %) 532.8 ± 0.1 (eV)	N 1s (at %) 400.1 ± 0.1 (eV)	C 1s (at %)[a] 285.2 ± 0.1 (eV)
SiO_2@ Yne-a	19.2	49.7	3.8	27.4
SiO_2@ Yne-b	22.3	51.3	3.1	25.3

[a] C 1s total carbon concentration % in the elemental analysis, the contents of each carbon species is reported in the appendix.

C 1s spectrum, shown in Fig. 3.9, was fitted with three peaks centred at 285.0, 286.2 and 289.8 eV, which were assigned to C-C and C-Si; C-N, C–O; and C=O, respectively. The signal at 285 eV, attributed to C-C bond, is generally affected by impurities coming from external contamination unavoidable during XPS measurements.

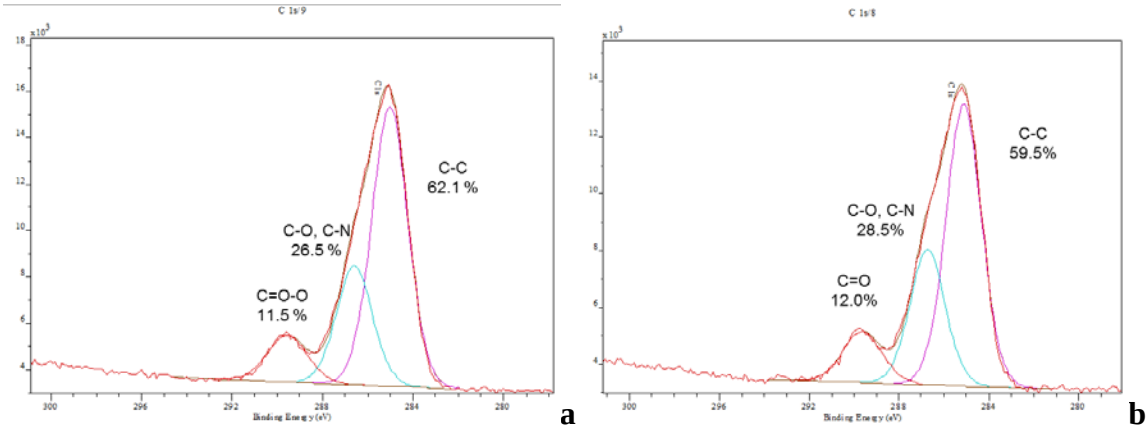

Figure 3.9 Peak-fitted C 1s for **a) SiO_2@Yne-a b)SiO_2@Yne-b**.

By considering the percentage ratio of the areas under the well separated peaks (C-C or C-O/N or C=O) with the total area of C 1s, the carbon composition percentage (*C %*) of each species was obtained. These values are reported in Table 3.4 and shown in Fig. 3.9.

Table 3.4 Carbon composition percentage from the C 1s deconvolution C 1s peak.

C 1s	BE (eV)	**SiO_2@ Yne-a** (*C %*)	**SiO_2@ Yne-b** (*C %*)
C 1s C-C, C-H	285.1 ± 0.1	62.1	59.5
C 1s C-O, C-N	286.7 ± 0.1	26.5	28.5
C 1s O=C-O	289.6 ± 0.1	11.5	12

By the ratio of these values (Table 3.4) with the C=O content, an idea of the different number of carbons present on the anchored molecules on the silica surface is given. These values are in agreement with the structure of condensed PPTEOS (Fig. 3.10); in the case of C-N, C-O, and C-C (where also the effect of the contamination is present) the experimental ratios are slightly larger than the theoretical ones (Table 3.5). This fact can be ascribed to incomplete hydrolysis and condensation of ethoxysilyl residues coming from the two organo-silane precursors (TEOS and PPTEOS), as also observed with previous techniques. The incomplete condensation of ethoxy groups is usually observed in the sol-gel synthesis.[9]

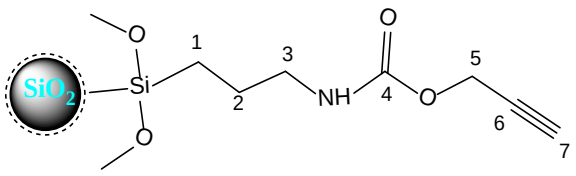

Figure 3.10 Alkyne-terminated moieties containing three C-C (2, 6, and 7) and one C-Si (1), two C-X (3 and 5), and one C-O (4).

Table 3.5 Ratio of the elements with C=O for **SiO_2@Yne-a;** and **SiO_2@Yne-b.**

Entry	Ratio	**SiO_2-Thio-Yne-a**	**SiO_2-Thio-Yne-b**
1	NH/C=O	1.1	1.2
2	C-C/C=O	5.4	4.9
3	C-N, C-O/C=O	2.3	2.4
4	Si/O	0.39	0.43
5	Si/N	5.05	7.02
6	Si/N(tot)	3.6	5.2

The Si/N ratio gives an indication of the functionalization degree of silica. In fact, the nitrogen present in this system comes only from the carbamate functionalities of PPTEOS (Table 3.5) and the lower value for **SiO_2@Yne-b** confirmed that this sample is less functionalized than **SiO_2@Yne-a.** By XPS analysis it was possible to confirm, according to our previous results, that PPTEOS is anchored on the silica surface, but the main aim was to have an XPS reference for the next synthetic steps.

3.1.2 Thiol-yne functionalized silica nanoparticles (SiO_2@Thio-Yne)

3.1.2.1 Synthesis of SiO_2@Thio-Yne

The alkyne-functionalized silica **SiO_2@Yne** was further modified by the thiol-yne click reaction (TYC, see introduction). This reaction offers an alternative to other functionalization techniques, such as Cu-catalyzed azide alkyne cycloaddition, and permits an efficient coupling between various types of molecules onto a nanoparticle surface.[10] To the best of our knowledge, the use of this reaction for the functionalization of silica was not previously reported. In this paragraph, the modification of **SiO_2@Yne** matrix by thiol-yne coupling with cysteamine hydrochloride is reported.

The click reaction on **SiO_2@Yne** was performed in the presence of 2,2-dimethoxy-2-phenylacetophenone (DMPA) as photoinitiator (10% mol to cysteamine hydrochloride) and cysteamine hydrochloride (**3**). The **SiO_2@Yne** powder was first redispersed in EtOH and subsequently added to **3** and DMPA, under a nitrogen atmosphere. The thiol−yne click reactions were initiated by exposure to a light with λ = 365 nm for 3 h at room temperature (Scheme 3.3). Afterwards the **SiO_2@Thio-Yne** was recovered by centrifugation and washed with EtOH and water, obtaining a light yellow powder with a yield of 95 %.

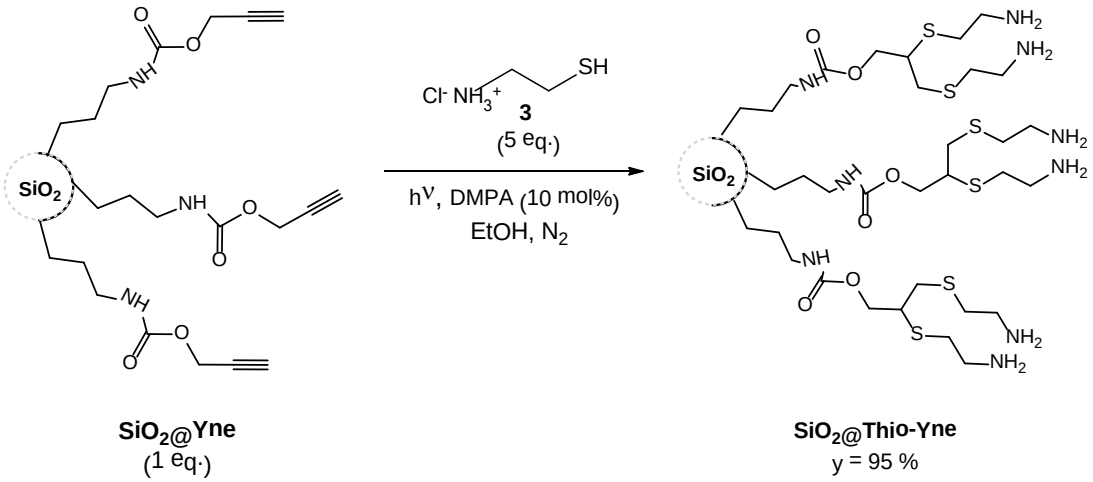

Scheme 3.3 Thiol-yne reaction between alkyne-functionalized silica nanoparticles (**SiO_2@Yne**) and cysteamine hydrochloride.

In order to selectively obtain the bis-sulfide adduct **SiO_2@Thio-Yne** the reaction was performed according to previously developed methods (Scheme 3.3).[2,10] The experimental conditions employed (thiol/alkyne molar ratio, temperature, and solvent) play an important role in order to avoid the detrimental formation of **SiO_2@vinyl sulfide** adduct, as described in detail in Chapter 1.

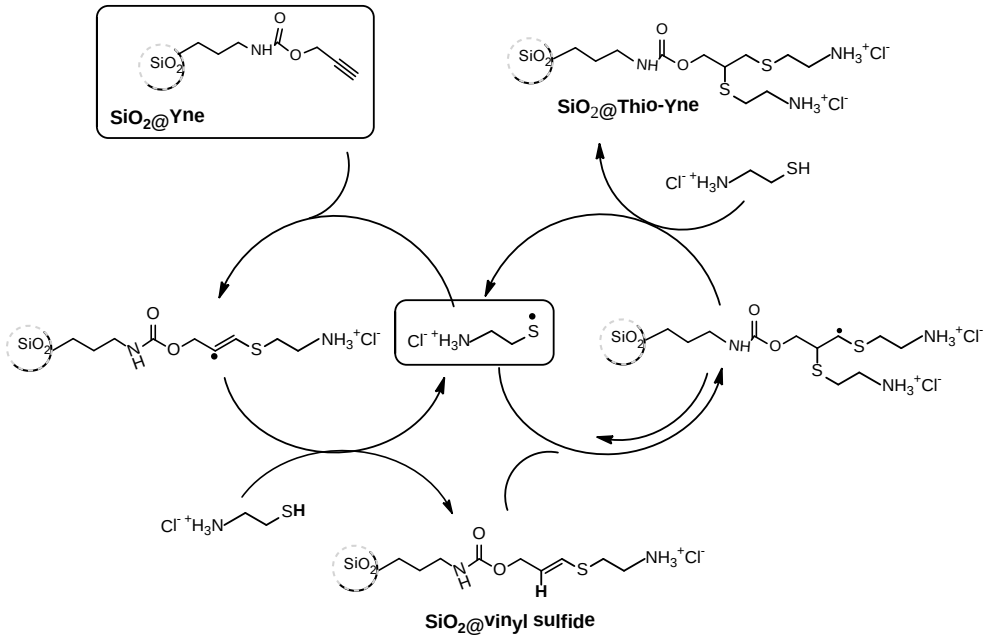

Scheme 3.4 Mechanism of thiol-yne coupling reaction for **SiO_2@Yne**.

[2] In the procedure reported in the literature two equivalents of thiols (to alkyne), 10% mol of DMPA in different solvents were used, obtaining the bis-sulfide adduct in high yields.

To evaluate the best experimental conditions the reaction was first performed using propargyl alcohol as a model substrate. The reaction was carried out with propargyl alcohol (1 eq.) and a stoichiometric amount of cysteamine hydrochloride (2 eq.) in the presence of DMPA (10% mol with respect to the thiol substrate) by using different solvents: ethanol, toluene, or water (Scheme 3.5). By comparison of the ESI-MS(+) and NMR spectra it was possible to distinguish the different species present in the mixture (Scheme 3.5).

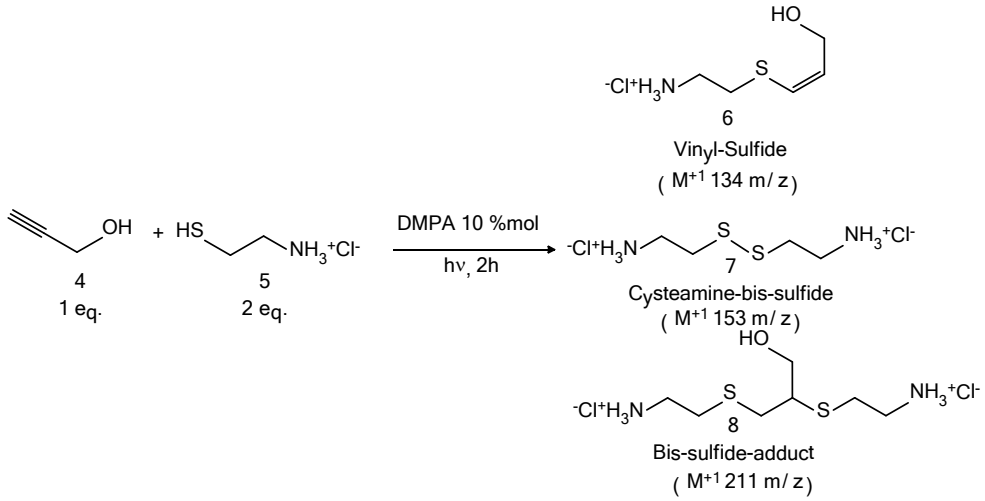

Scheme 3.5 Thiol-yne reaction between cysteamine hydrochloride and propargyl alcohol and the possible products formed in the reaction, with their respective M^{+1} values.

The best results, confirmed by NMR and ESI-MS, were obtained for the reaction in ethanol, where only the formation of the bis-sulfide adduct **8** was observed (peak at *m/z* 211 in Fig. 3.11). In water the target product **8** as well as vinyl-sufide **6** and the bis-cysteamine disulphide **7** were obtained (Fig 3.11); similar results were also observed for the reaction in toluene. Additional reasons for considering ethanol as an optimal solvent for this reaction are suitability for re-dispersion of the **SiO_2@Yne** powder (with the use of a sonic bath in order to obtain a homogeneous system) and solubility of all used reagents.

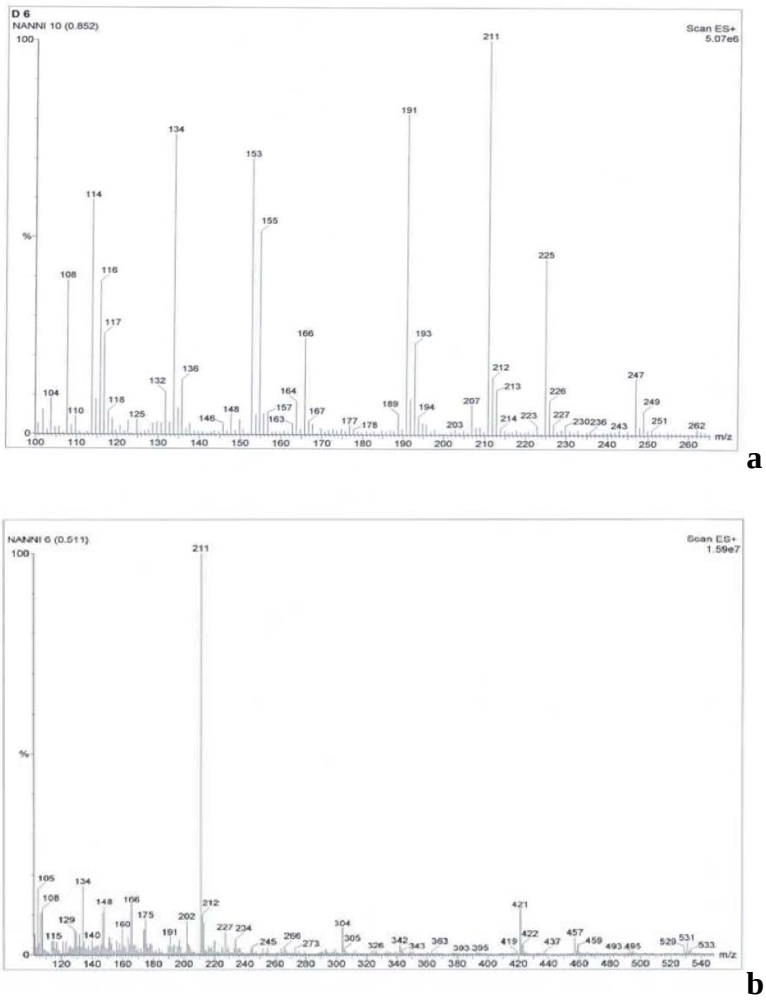

Figure 3.11 ES-MS(+) spectra of **a)** thiol-yne reaction in water; **b)** thiol-yne reaction in ethanol.

The reactions between **SiO_2@Yne** and cysteamine hydrochloride were actually performed using five equivalents of the latter. An excess of cysteamine was considered necessary in order to shift the reversible equilibria described in Scheme 3.4 towards the selective formation of the bis-sulfide **SiO_2@Thio-Yne**. The use of an excess of starting cysteamine hydrochloride did not bring additional purification problems as it can be easily separated from the functionalized nanoparticles by centrifugation.

In the method termed (i) the excess of starting cysteamine hydrochloride was added at once at the beginning of the reaction. This procedure resulted in formation of by-product, non-reactive disulfide cysteamine derivative. Therefore, in a second approach termed (ii), cysteamine hydrochloride was added in portions in the course of the reaction. The two methods (i) and (ii) were used for both samples **SiO_2@Yne-a** and **b** obtaining **SiO_2@Thio-Yne-a(i)** or **(ii)** and **SiO_2@Thio-Yne-b(i)** or **(ii)**, respectively.

3.1.2.2 Characterization of SiO_2@Thio-Yne

TGA analysis

Table 3.6 shows the TGA results for **SiO_2@Thio-Yne** compared with **SiO_2@Yne**. **SiO_2@Thio-Yne-a(ii)** showed an additional weight loss of 10 % with respect to **SiO_2@Yne-a** not observed for **SiO_2@Thio-Yne-a(i)**. These data can be explained with a higher functionalization occurring by adding the cysteamine hydrochloride in different portions during the reaction. As far as sample **SiO_2@Thio-Yne-b(ii)** is concerned**,** the organic load is lower than in **SiO_2@Thio-Yne-a(ii)**, but higher than that of the alkyne derivate.

Table 3.6 Comparison of TGA results for **SiO_2@Thio-Yne-a** by (i) and (ii) method.

Samples	TGA (%)[a]	TGA (%)[b]	TGA%[c]
SiO_2@Yne-a	22.4	15.8	10.8
SiO_2@Thio-Yne-a(i)	21.9	17.1	9.3
SiO_2@Yne-a(ii)	21.7	15.1	10.1
SiO_2@Thio-Yne-a(ii)	31.3	25.3	20.1
SiO_2@Yne-b	19.4	13.7	8.7
SiO_2@Thio-Yne-b (ii)	21.3	15.5	10.5

[a] Total wt% loss;
[b] Total wt % loss excluding water;
[c] Wt % corresponding to the organic fraction;

In view of these results, from this point onward, only the samples obtained by the method **(ii)** will be taken into account.

FT-IR analysis

The FT-IR spectra of **SiO_2@Thio-Yne-a** and **b** shows that the alkyne moieties are still present (2131 cm^{-1}) and the obtained spectra are very similar to those of the corresponding **SiO_2@Yne** (Fig. 3.12).

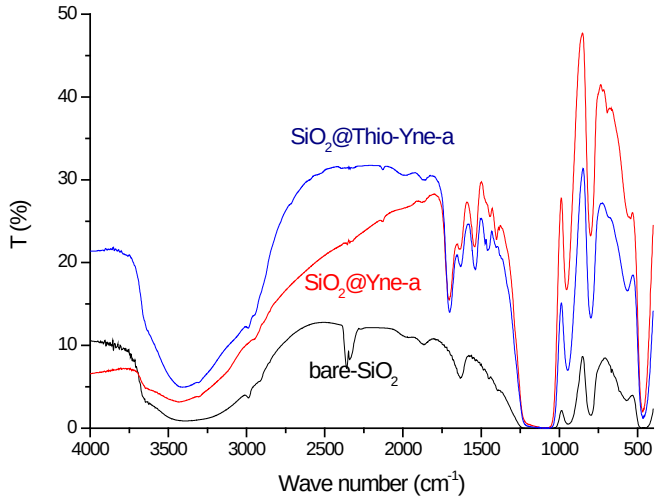

a

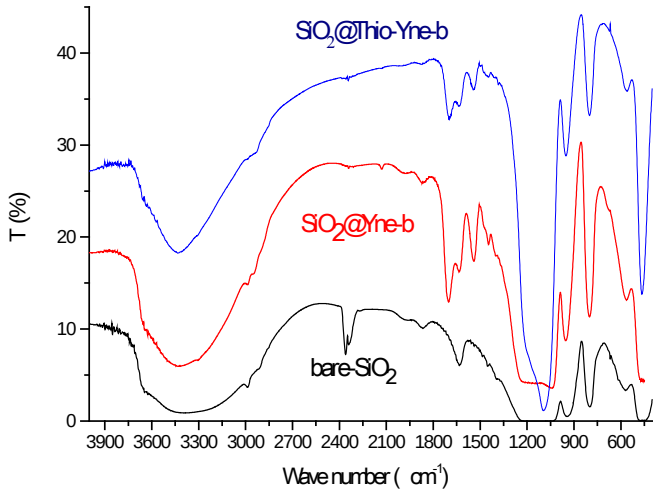

b

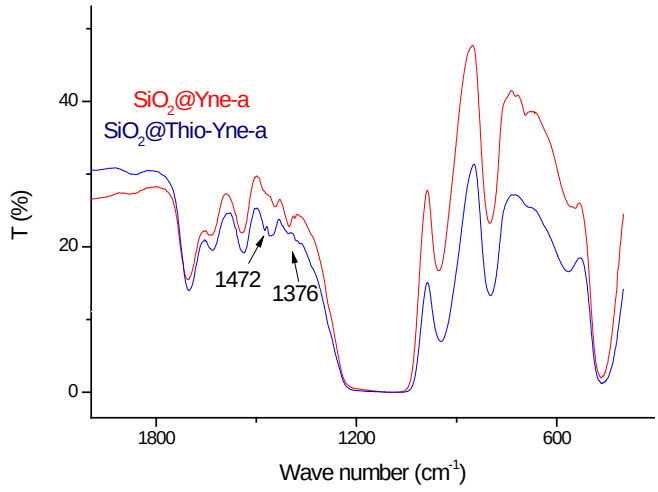

c

Figure 3.12 FT-IR spectra comparison; **a) bare-SiO_2** (black line) with **SiO_2@Yne-a** and **SiO_2@Thio-Yne-a**; **b) SiO_2@ Yne-b** (red line), **SiO_2@Thio-Yne-b** (blue line), and **bare-SiO_2** (black line); **c)** Enlargement of the spectra of **SiO_2@Thio-Yne-a** in the spectral range of 1800-1200 cm^{-1}.

Comparing the spectra of **SiO_2@Thio-Yne** with **SiO_2@Yne** few differences can be observed (Fig. 3.12). The weak band at 2977 cm^{-1}, present on bare silica and **SiO_2@Yne** owing to unreacted ethoxy-silane groups, disappeared in the case of **SiO_2@Thio-Yne-b** as a result of their complete hydrolysis. Additionally, two new very weak bands at 1472 and 1376 cm^{-1} are observed and they can be tentatively ascribed to δ_s and δ_{as} of C-H bonds. By this technique the sulfide C-S bonds are not well recognizable. Unfortunately, although in Raman spectroscopy the C-S bonds give usually rise to strong, intense bands, we could not make use of this technique as the spectra of the **SiO_2@Thio-Yne** samples presented a significative fluorescence contamination that did not allow spectra recording.

*TEM characterization of **SiO_2@Thio-Yne***

DLS and TEM results are resumed in Table 3.7. TEM micrographs did not show any substantial difference between the corresponding alkyne derivatives and the thiol-yne ones. Only few nanometers in difference were observed. In fact this technique cannot detect functionalization changes that vary the surface of few Å. The TEM picture for **SiO_2@Thio-Yne-a** and **b** sample are reported in Fig. 3.13.

Table 3.7 DLS and TEM results for **SiO_2@Thio-Yne-a** and **b.**

Sample	DLS (nm)	TEM (nm)	TEM (nm)[a]
	SiO_2@Thiol-yne	**SiO_2@Thiol-yne**	**SiO_2@Yne**
SiO_2@Thio-Yne-a	300	81 ± 22	79 ± 24
SiO_2@Thio-Yne-b	220	49 ± 5	45± 6

[a] TEM results for **SiO_2@Yne** are also reported

The hydrodynamic diameter measured by DLS can provide more information, evidencing the changes in the interactions with the solvent due to the incorporation on the surface of charged R-NH_3^+ groups. In general, the DLS diameter is bigger than the TEM radius, like seen before, but in all thiol-yne samples an increase of the diameter with respect to the alkyne-modified ones was always observed. This fact clearly suggests that the thiol-yne reaction has occurred.

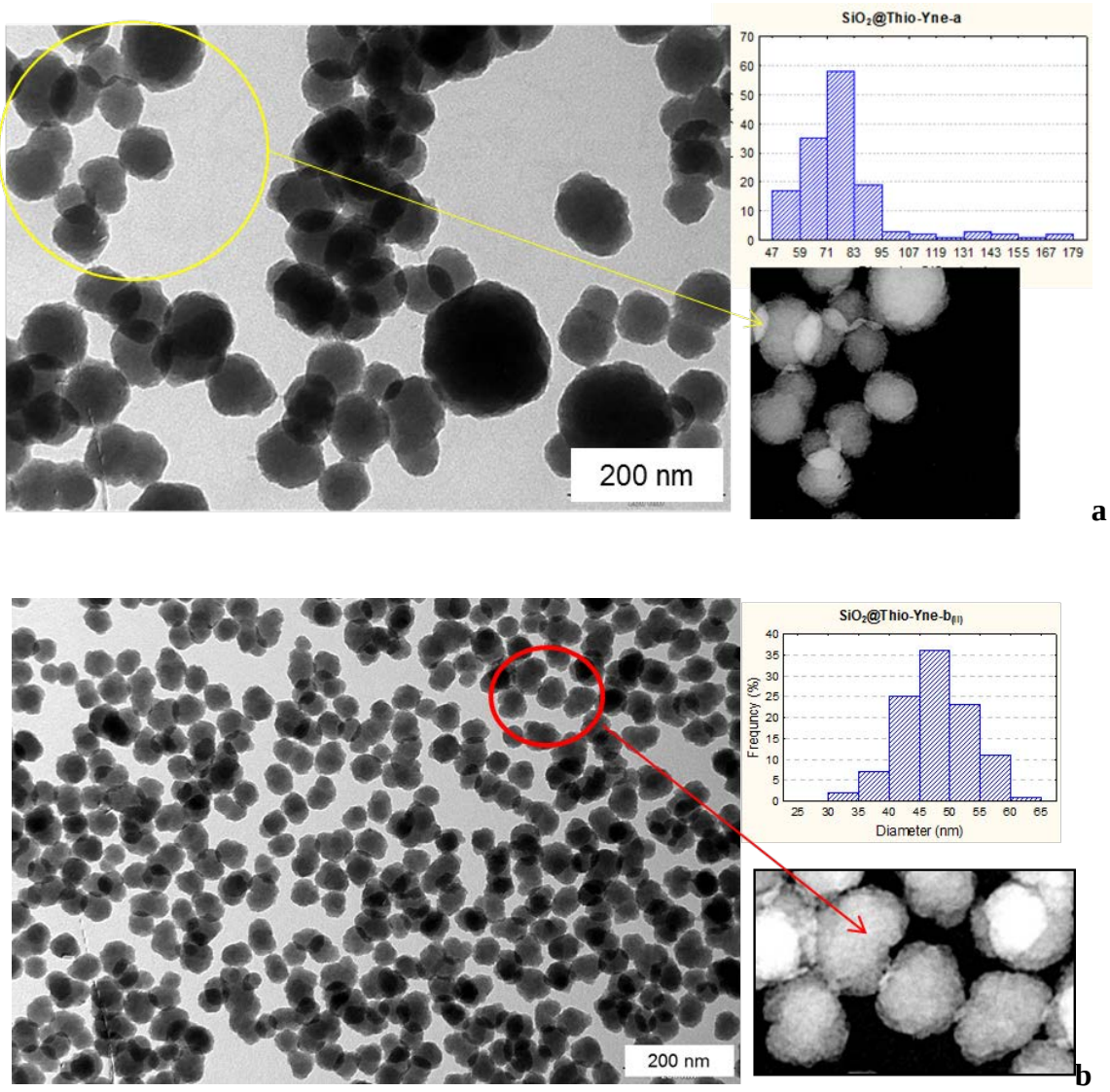

Figure 3.13 TEM micrograph **a) SiO_2@Thio-Yne-b; b) SiO_2@Thio-Yne-b**.

XPS ***SiO_2@Thio-Yne***

The successful thiol-yne click functionalization of the surface of **SiO_2@Yhio-Yne** was evidenced by the appearance of S 2p and Cl 2p peaks, at 163.6 and 197.8 eV respectively, in the XPS survey spectra (Fig. 3.14).

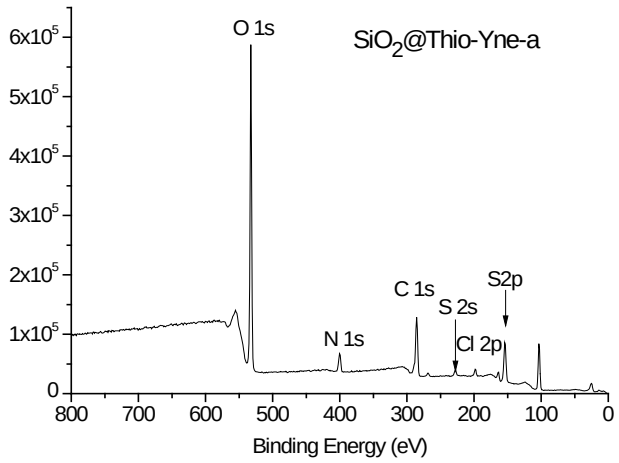

Figure 3.14 XPS survey spectra of **SiO_2@Thio-Yne-a**.

The relative elemental composition for **SiO_2@Thio-Yne-a** and **b**, is reported in Table 3.8.

Table 3.8 XPS atomic percentage (at %) for **Au-SiO_2@Thio-Yne-a** and **b**.

Samples	Si 2p (at %) 103.2 ± 0.1 (eV)	O 1s (at %) 532.7 ±0.1 (eV)	N 1s (at %) 399.9 ±0.1 (eV)	C 1s (at %) 285.0 ±0.1 (eV)	S 2p (at %) 163.6 ±0.1 (eV)	Cl 2p (at %) 197.8±0.1 (eV)
SiO_2@Thio-Yne-a	18.3	42.8	5.1	31.4	1.5	0.9
SiO_2@Thio-Yne-b	21.2	49.3	4.1	24.2	0.8	0.4

The N 1s peak was resolved into two peaks at 399.9 and 401.7 eV, corresponding to C-NH-(C=O) of the carbamate moieties and to NH_3^+ of the bis-sidulfide adducts, respectively. The percentage ratio obtained by dividing the area under $–NH_3^+$ or NH-C=O with the sum of N 1S areas (N %) permits to estimate the reaction yield. To obtain the bis-sulfide adducts (**7**) the alkyne moieties have to react with two cysteamine molecules. In case of total conversion the expected percentage for NH_3^+ and NH-C=O would be ca. 66 and 33 %, respectively (two NH_3^+ for one NH carbamate). Comparing that theoretical values with the percentage compositions obtained by XPS, the reaction yield for **SiO_2@Thio-Yne-a** and **b** were estimated as 40 % and 33 %, respectively.

Table 3.9 XPS N 1s percentage (at %)

N 1s	BE (eV)	**SiO_2@Thio-Yne-a** (*N %*)	**SiO_2@Thio-Yne-a** (*N %*)
N 1s C-NH-(C=O)	399.9	73.1	78.2
N 1s $–NH_3^+$	401.7	26.9	21.8

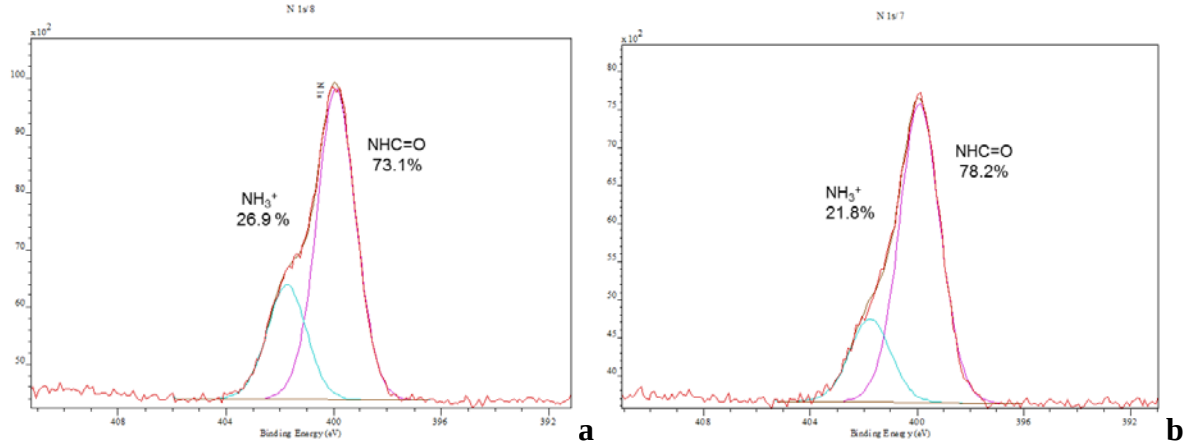

Figure 3.15: N 1s XPS spectrum **a) SiO_2@Thio-Yne-a; b) SiO_2@Thio-Yne-b**.

The XPS C 1s peak at 285.0 was deconvoluted in three peaks, 285.0, 286.4, and 289.5 eV corresponding to C-C, C-Heteroatoms (CO, C-N, C-S), and C=O, resepctively (Fig. 3.16). Comparing the % composition of C1s peaks with **SiO_2@Yne** samples (Table 3.10) it is possible to observe an increment in carbon-heteroatoms bonds (C-O, C-S, C-N), with a proportional decrease in C-C. In fact, the thol-yne reaction modifies the alkyne terminated structure in two sulfide adducts both ending with ammonium ions, where, from initial two C-Heteroatoms bonds, we got to seven C-Heteroatoms (C-S, C-N, C-O).

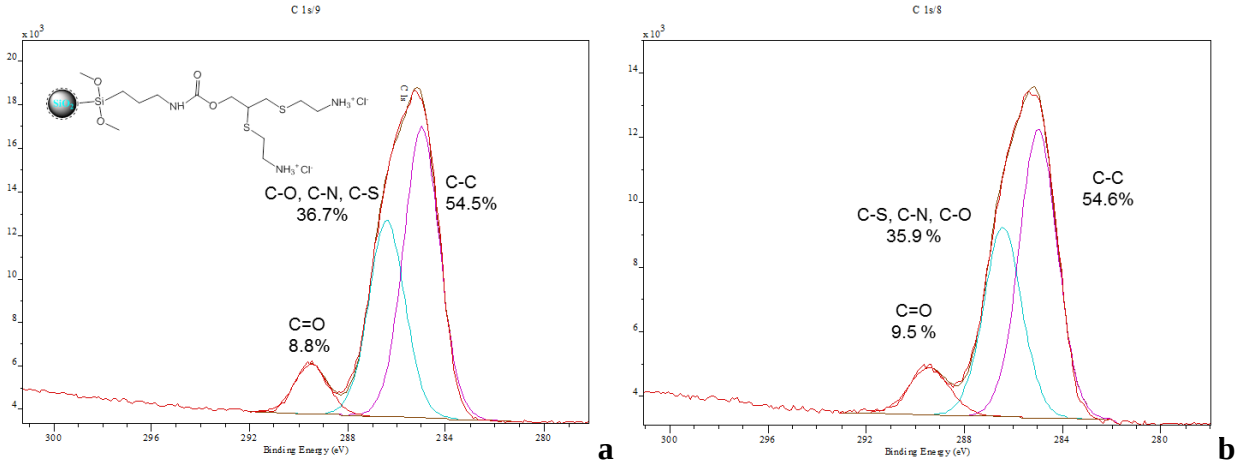

Figure 3.16 XPS C1s spectrum and carbon composition percentage **a) SiO_2@Thio-Yne-a**; **b) SiO_2@Thio-Yne-b**.

Table 3.10 Comparison of XPS C1s composition % between **SiO_2@Thio-Yne-a** and **b** and **SiO_2@Yne-a** and **b**.

Name	BE (eV)	**SiO_2-Thio-Yne-a** *(C %)*	**SiO_2@Yne-a** *(C %)*	**SiO_2-Thio-Yne-b** *(C %)*	**SiO_2@ Yne-b** *(C %)*
C 1s C-C, C-H	285.0	54.5	62.1	54.6	59.5
C 1s C-O, C-N, C-S	286.4	36.7	26.5	35.9	28.5
C 1s O=C-O	289.5	8.8	11.5	9.5	12

The different ratios of the elemental composition are reported in Table 3.11. The S/NH_3^+ ratio (ca. 1) is in line with a sulfur content proportional to the amount of NH_3^+. The higher ammonium-chlorine ratio, expected to be one, can be justified from the fact that the chlorine present is in amounts (<1 %) whithin the instrument detection limit. The Si/N ratio decreases with respect to the **SiO_2@Yne** samples, and this is consistent with the higher contents of nitrogen after the TYC reaction.

Table 3.11 Ratio of the elemental composition (at %)

Entry	Ratio	**SiO_2-Thio-Yne-a**	**SiO_2-Thio-Yne-b**
1	S/NH_3^+	1.1	0.9
2	NH_3^+/NH-C=O	0.4	0.398
3	NH-C=O/C=O	1.3	1.4
4	NH_3^+/Cl	1.5	2.1
5	Si/O	0.4	0.4
6	Si/N(tot)	3.6	5.2

According to the XPS results, only 20 and 17 % of alkynes, for **SiO_2@Thio-Yne-a** and **b** respectively, react with cysteamine hydrochloride to give the functionalized silica (Fig. 3.16). Although the presence of vinyl sulfide adducts cannot be completely excluded by this technique, where the differences in carbon hybridization cannot be detected, the preliminary tests conducted with propargyl alcohol in similar conditions gave no evidence of the presence of vinyl sulfide monoadducts. Moreover, in both **SiO_2@Thio-Yne-a** and **b**, FT-IR spectra showed no bands associated to vinyl groups, showing instead, as confirmed by XPS, signals due to the residue alkyne groups remaining from the incomplete TYC reaction.

We suggest that the partial conversion of the TYC reaction is not due to the experimental conditions, but rather to mainly steric and/or electrostatic interactions between the silica-anchored alkyne moieties and cysteamine. In fact, with respect to "free" alkynes, our triple bonds are distributed on the silica surface and, as they react with cysteamine forming the bulky bis-sulfide adduct, they could hinder the analogous reaction of a vicinal alkyne, that will be much less accessible to attack by the cysteamine sulfanyl radicals both by steric reasons and by electrostatic interactions between the anchored cysteamine and the free, approaching one. This part will be discussed in details in the XPS session of **Au-SiO_2@Thio-Yne** samples.

3.1.3 Au_{NPs} supported by SiO_2@Yne (Au-SiO_2@Yne)

3.1.3.1 Synthesis of Au- SiO_2@Yne

The preparation of alkyne-modified silica-supported Au_{NPs} (**Au-SiO_2@Yne**) was performed by simply adding an aqueous solution of $HAuCl_4$ (1 mM) to a dispersion of **SiO_2@Yne** in water in an ultrasonic bath at 30 °C for 30 minutes. The ultrasonic bath was used to avoid silica aggregation and to maintain the system homogeneous throughout the reaction. The amount of Au(III) precursor used was chosen in order to have a theoretical total amount of gold of 4.6 wt.%. During the first 10 minutes the pale yellow colour of the reaction mixture turned first to violet and then gradually to red-purple (Scheme 3.6). At the end of the reaction, a portion of the crude material was directly analyzed by TEM, while the rest was separated by centrifugation and dried by an intense flux of N_2 in oven at 50 °C for 4 h to give **Au-SiO_2@Yne** as a purple powder analyzed by XPS, UV-vis, and FT-IR analysis.

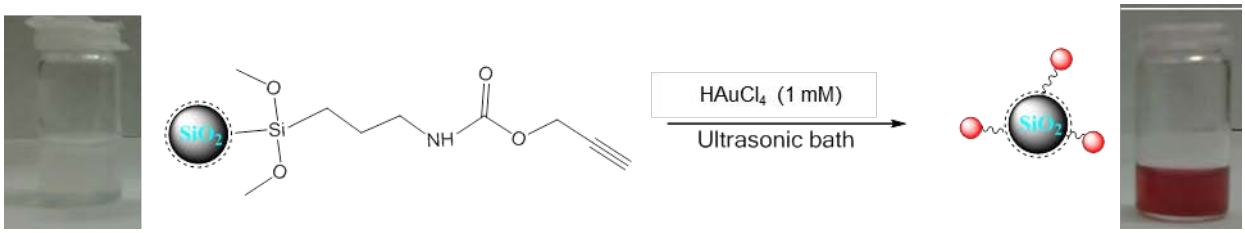

Scheme 3.6 Synthesis of **Au-SiO_2@Yne**: **SiO_2@Yne** powder was dispersed in water and a $HAuCl_4$ solution was added to obtain a final concentration of 0.5 mM. The final colour of the dispersion **Au-SiO_2@Yne** (right) is compared with the initial white dispersion (left).

It is worth noting that **bare-SiO_2**, under the same reaction conditions, gave no change in colour, even after months.

3.1.3.2 Characterization of Au-SiO_2@Yne

UV-vis

The UV-vis absorption spectra of the **Au-SiO_2@Yne-a** and **b** are presented in Fig. 3.17 a and b. The **SiO_2@Yne-a** did not show any significant peaks in the analyzed wavelength range (black line), whereas a Surface Plasmon Resonance band (SPR) was observed for both A**u-SiO_2@Yne-a** and **Au-SiO_2@Yne-b** with maxima wavelength positions at 531 and 525 nm, respectively, confirming the Au_{NPs} formation.

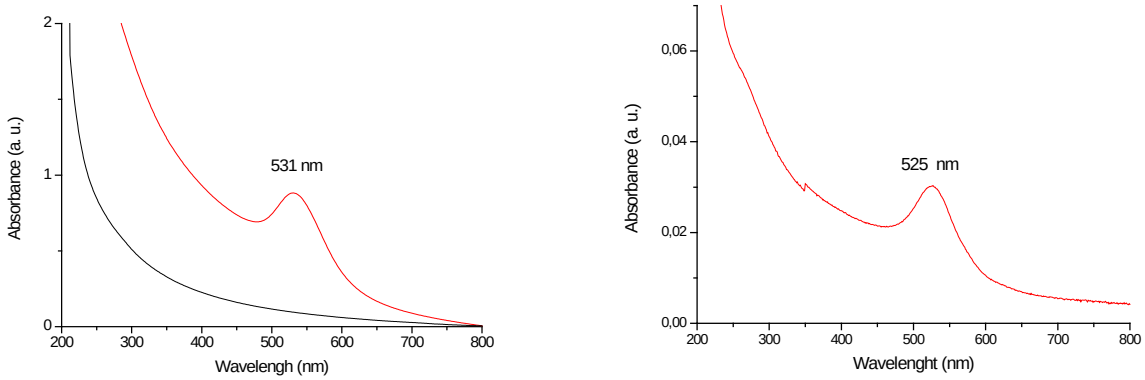

Figure 3.17 UV-vis spectra recorded for the aqueous dispersion of **a) Au-SiO$_2$@Yne-a**; **b) Au-SiO$_2$@Yne-b.**

*TEM **Au-SiO$_2$@Yne***

The morphology of the alkyne modified silica after the addition of the gold precursor was investigated by TEM microscopy. In Figs. 3.18 and 3.19 the TEM micrographs are reported for both samples **Au-SiO$_2$@Yne-a** and **b.** In both cases gold nanoparticles are attached on the silica surface and present an approximately spherical shape. Although the TEM analysis was carried out on the crude material prior centrifugation, no free gold nanoparticles were detected. In the first case (**Au-SiO$_2$@Yne-a**) the image reveals an average diameter of about 14 ± 3 nm (size distribution in Fig. 3.18 and Table 3.12).

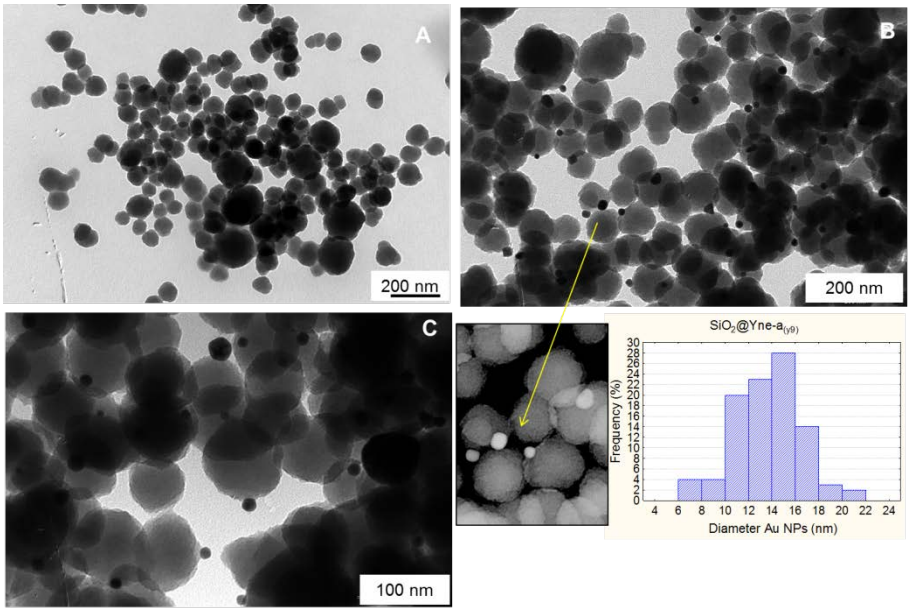

Figure 3.18 TEM micrograph and histogram of gold size distribution **Au-SiO$_2$@Yne-a.**

The TEM micrograph of **Au-SiO$_2$@Yne-b** reveals the presence of nanoparticles with an average diameter of 11 ± 4 nm (Fig. 3.19) however a population of smaller nanoparticles (ca. 6 nm) is also present, as shown in the size distribution histogram.

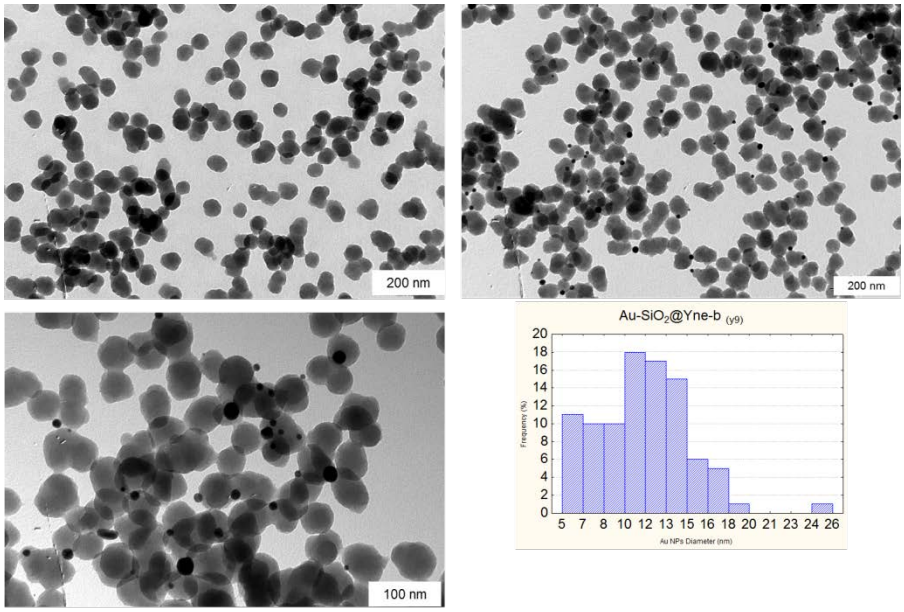

Figure 3.19 TEM micrograph of **a)** before gold addition **b) Au-SiO_2@ Yne-b**; **b)** histograms of particle size distribution of the Au_{NPs}.

Table 3.12 Comparison of average diameter calculated by TEM and maximum absorbance wavelength position in the UV-vis spectra.

Sample	λ_{max} (nm)	Au TEM (nm)
SiO_2@ Yne-a	531	14 ± 3
SiO_2@Yne-b	526	11 ± 2

FT-IR ***Au-SiO_2@Yne***

The FT-IR spectra of the synthetized **Au-SiO_2@Yne-a** (Fig. 3.21) and **b** (Fig. 3.32 in appendix) are very similar and show substantial changes compared to the **SiO_2@Yne** starting material: a loss in intensity of the bands at 1660 cm^{-1} (ν_s C=O) and 1538 cm^{-1} (δ N-H) was observed and it was attributed to modifications occurred to the carbamate group (*vide infra*).

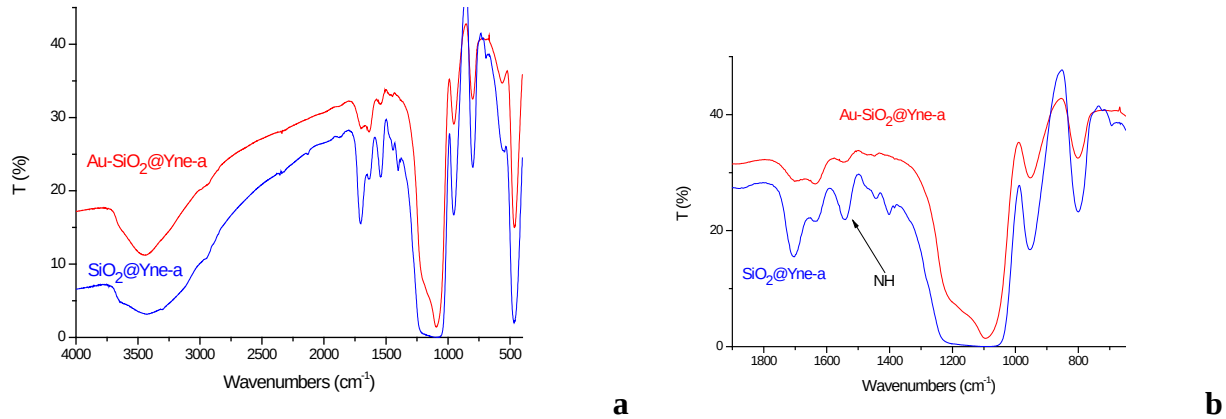

Figure 3.20 a) FT-IR spectra **Au-SiO$_2$@Yne-a**; **b)** Enlargement of the spectral window in the range 1900-650 cm^{-1}.

*XPS **Au-SiO$_2$@Yne***

XPS survey spectra of **Au-SiO$_2$@Yne** show the same elements present in **SiO$_2$@Yne** and the appearance of a new doublet ascribed to Au 4f$_{7/2}$ with a binding energy (BE) of 84.3 eV, which is characteristic of metallic Au(0) species.[11,12] In Table 3.13 the relative elemental composition (%) for **Au-SiO$_2$@Thio-Yne-a** and **b** is reported. In both cases a similar amount of gold is present (0.5 and 0.4 at %, respectively). In these peaks only the contribution from metallic gold is observed in both samples, and signals deriving from Au(I) and Au(III), generally with binding energies of 85.5 and 86.5 eV, were not observed.

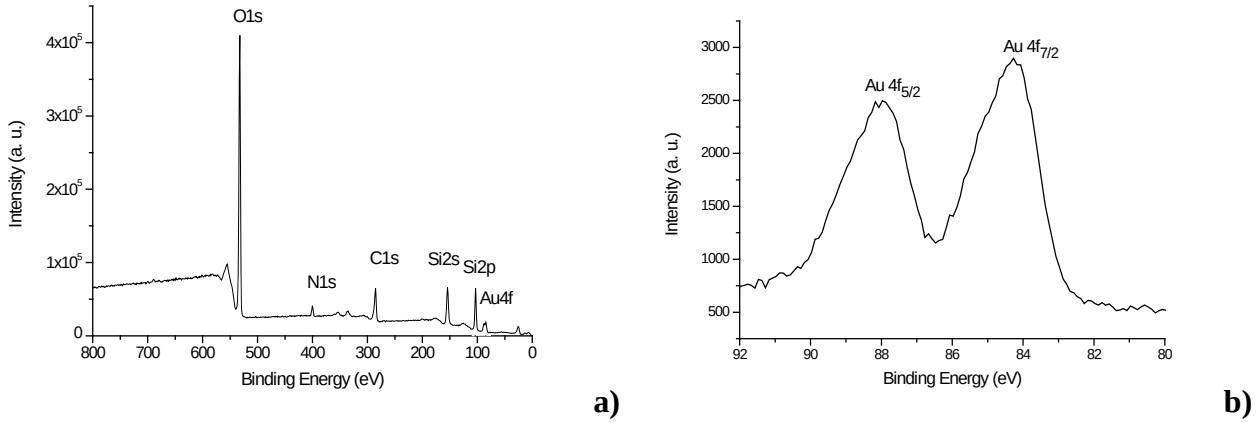

Figure 3.21 XPS survay spectra **a) Au-SiO$_2$@Yne-a**; **b)** XPS spectra of the Au 4f level.

Table 3.13 XPS atomic percentage (at %) for **Au-SiO$_2$@Yne-a** and **b**.

Sample	Si 2p (at %) 103.3±0.1 (eV)	O 1s (at %) 532.8±0.1 (eV)	N 1s (at %)[a] 400.1±0.1 (eV)	C 1s (at %) 285.2±0.1 (eV)	Au 4f (at %) 84.3±0.1 (eV)
Au-SiO$_2$@ Yne-a	20.8	50.4	3.6	24.7	0.5
Au-SiO$_2$@ Yne-b	21.6	54.8	2.9	20.2	0.4

The C1s peak at 285 eV was deconvoluted into four peaks: 285.1, 286.7, 289.6, and 288.4, corresponding to C-C (C-H and C-Si), C-Heteroatoms (C-O, C-N), O-C=O, and to a new species, respectively. This new peak at 288.4 eV, not previously observed for **SiO$_2$@Yne** samples, was formed during the reduction of Au(III) to Au(0).

The percentage ratio in carbon (*C %*) of the deconvoluted species (C-C; C-N, C-O; C=O, and the new C species respectively divided by the total carbon content) was considered and compared with the obtained values for the **SiO$_2$@Yne** samples (Fig. 3.22 a and b).

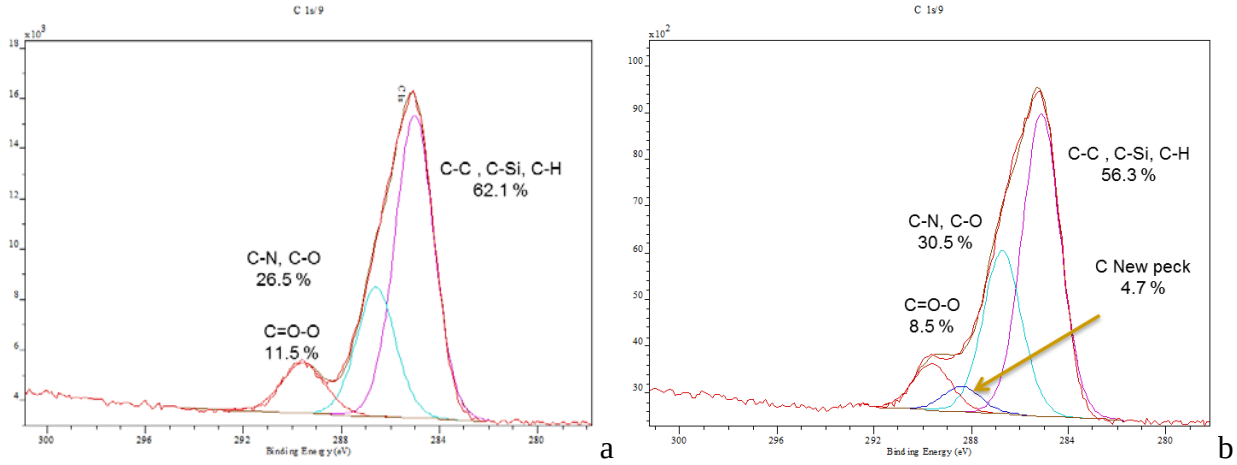

Figure 3.22 XPS C1s spectrum and carbon composition percentage **a) SiO$_2$@Yne-a**; **b) Au-SiO$_2$@Yne-a,** with a new band at 288.4 eV.

For sake of clarity the XPS data for **SiO$_2$@Yne** already reported in Table 3.4 are also reported in Table 3.14.

Table 3.14 XPS C1s composition percentage.

C 1s	BE (eV)	**Au-SiO$_2$@Yne-a** (*C %*)	**SiO$_2$@ Yne-a** (*C %*)	**Au-SiO$_2$@Yne-b** (*C %*)	**SiO$_2$@ Yne-b** (*C %*)
C 1s C-C, C-H	285.1 ± 0.1	56.3	62.1	53.1	59.5
C 1s C-O, C-N	286.7 ± 0.1	30.5	26.5	32.5	28.5
C 1s O=C-O	289.6 ± 0.1	8.5	11.5	8.9	12
C 1s new peak	288.4 ± 0.1	4.7	-	5.7	-

With respect to the carbon composition percentage C 1s, a comparison between **Au-SiO_2@Yne** and **SiO_2@Yne** data show, for the former, an evident decrease in O-C=O and C-C contents with a simultaneous increase in C-N, C-O and formation of a new species at 288.4 eV. As a general rule of the XPS technique, bonds with electronegative atoms lead to a shift towards higher binding energy (i.e. lower kinetic energy). The carbon in the carbamate (H)NC(O)X group, attached to electronegative atoms X such as oxygen and nitrogen, has a peak with a binding energy of 289.6 eV well distinguishable, by deconvolution (Fig. 3.22), from the new species found at 288.4 eV. For the latter a change in the environment is observed with a binding energy characteristic of a carbonyl species such as RC(O)R' in which R is a carbon and R' can be a carbon or hydrogen, like in a ketone or an aldehyde.[13]

The elemental analysis of **Au-SiO_2@Yne** (%) compared to **SiO_2@Yne (**Table 3.15) shows a decrease in the carbon content, whereas the nitrogen amount does not change significantly.

Table 3.15 Comparison of elemental composition in **SiO_2@Yne** and **Au-SiO_2@Yne.**

Samples	Si 2p (at %) 103.3 ± 0.1 (eV)	O 1s (at %) 532.8 ± 0.1 (eV)	N 1s (at %) 400.1 ± 0.1 (eV)	C 1s (at %)[a] 285.2 ± 0.1 (eV)
Au-SiO_2@ Yne-a	20.8	50.4	3.6	24.7
SiO_2@ Yne-a	19.2	49.7	3.8	27.4
Au-SiO_2@ Yne-b	21.6	54.8	2.9	20.2
SiO_2@ Yne-b	22.3	51.3	3.1	25.3

Tentative mechanistic hypotheses

Reactions of alkynes with Au(III) substrates are well documented in literature, where in general the partial reduction of Au(III) to Au(I) brings to mixed Au(III) and Au(I) complexes not as stable as the thiol and phosphine analogues.[14] Au(III) and Au(I) complexes can interact with the triple bond upon coordination and activate the alkyne moiety, which becomes more reactive towards nucleophiles. For example, Zhang reported that systems similar to ours, such as propargyl esters (Scheme 3.7), experience a great variety of chemical transformations catalyzed by Au(III) and Au(I) complexes. In his works[15,16,17] he proposed different reaction mechanisms involving a structural rearrangement by either 1,2- or 1,3-acyl migrations to give the α-vinyl gold oxocarbenium as reported in Scheme 3.7.

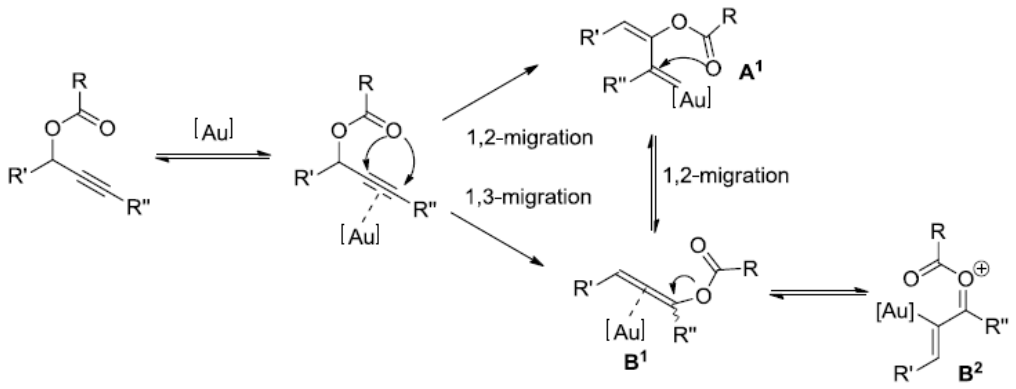

Scheme 3.7 Zhang Gold (III)-catalyzed propargyl ester rearrangements, where R= H, CH_2-CH_3.

Since in the reported studies no reduction to Au(0) was ever observed, we were led to suppose that, in our system, the presence in the **SiO_2@Yne** of the carbamic nitrogen instead of the alkyl group R (the only notable difference) could be able to explain such an efficient formation of gold nanoparticles. A similar 1,3-acyl migration mechanism was hence hypothesized involving the carbamic nitrogen (Scheme 3.8) with formation of an allene intermediate **A** followed by decarboxylation (to give **B**) and rearrangement to the eventual unsaturated imine **D**. That imine, as well as its hydrolysis products (e.g. **E**), can act as an efficient reducing agent for Au(III) or Au(I) to Au_{NPs}, in analogy with the behaviour of silica-PEI (see chapter 2); oxidation of the carbamate branch would eventually account, at the same time, for the formation of new carbonyl moieties (e.g. an aldehyde) on the silica, as shown by XPS data.

Moreover, this tentative mechanism can explain the change in the percentage content of the total carbon respect to **SiO_2@Yne** samples. The formation of **F** can also justify the decrease in intensity of the N-H bending vibration in **Au-SiO_2@Yne** FT-IR spectra (Fig. 3.20). Although XPS analyses did not show any significant variation in the percentage content of nitrogen, this can be explained in terms of the fact that bending vibration in amines are more difficult to be detected, respect to the N-H of carbamate.[18]

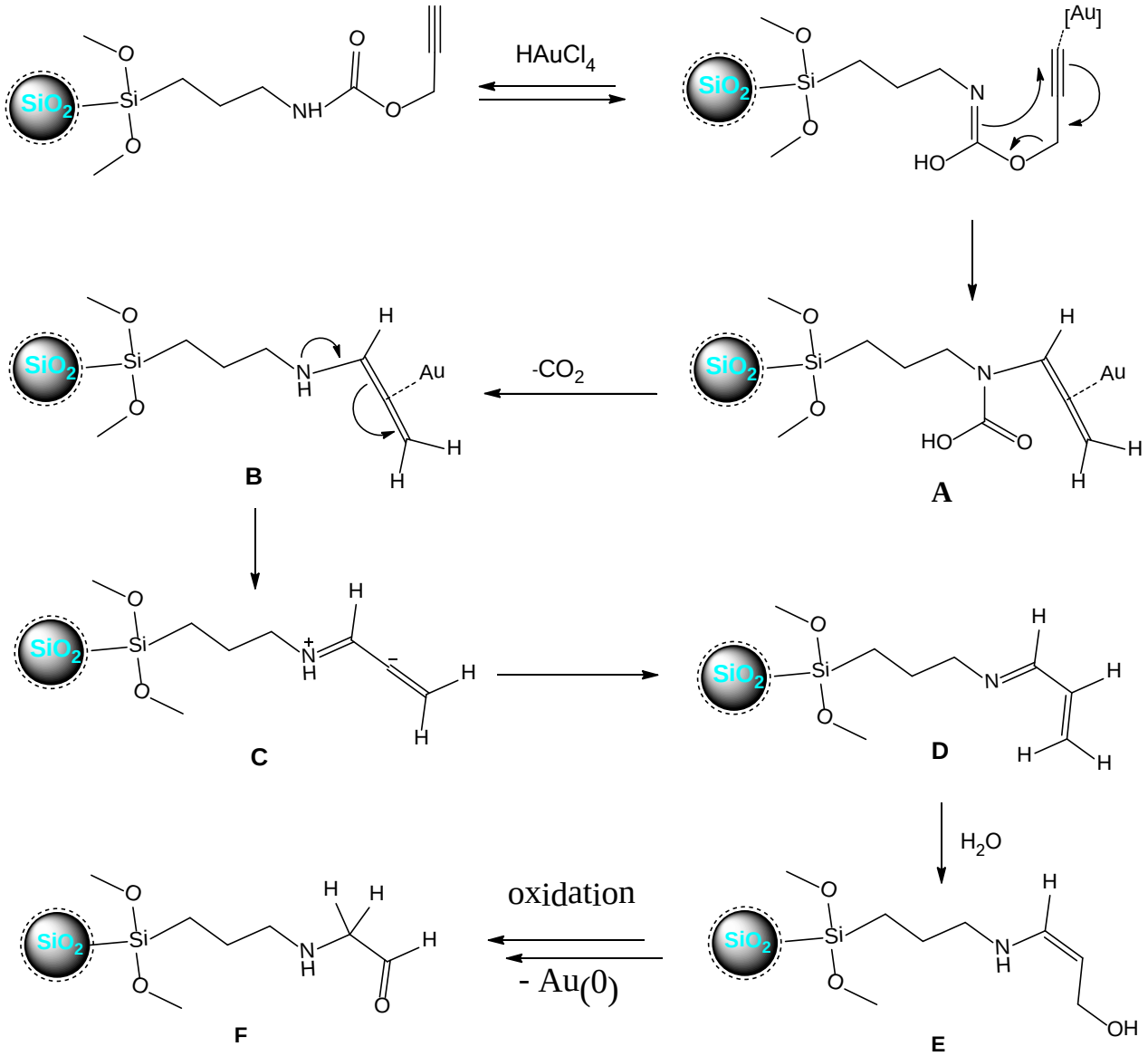

Scheme 3.8 Proposed mechanism for the **SiO_2@Yne**-mediated reduction of $HAuCl_4$.

3.1.4 Au_{NPs} supported by SiO_2@Thio-Yne (Au- SiO_2@Thio-Yne)

*Synthesis of **Au-SiO$_2$ @Thio-Yne***

The preparation of thiol-yne modified silica was performed under the same conditions described for the **Au-SiO$_2$@Yne** by simply adding an aqueous solution of $HAuCl_4$ (1 mM) to a dispersion of **SiO$_2$@Thio-Yne** in water in an ultrasonic bath at 30 °C. Few minutes after the gold precursor is introduced, a yellow, intense orange colour is detected, which gradually changes to red-purple during a period of 20 minutes (Scheme 3.9).

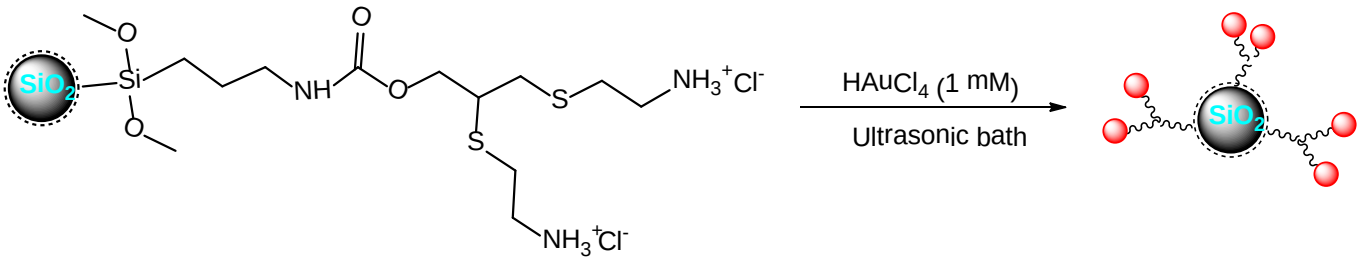

Scheme 3.9 Synthesis of **Au-SiO$_2$@Thio-Yne**: **SiO$_2$@Thio-Yne** are dispersed in equal volumes of water and $HAuCl_4$ (1 mM) solution, to obtain a 0.5 mM final concentration of Au(III).

The first colour change suggests the initial formation of a Au(III)-disulfide complex that is gradually reduced to Au(0) with concomitant oxidation of the disulfide groups. As previously described for **Au-SiO$_2$@Yne**, at the end of the reaction, a portion of the crude material was directly analyzed by TEM, while the rest was separated by centrifugation and dried in oven at 50 °C for 4 h to give **Au-SiO$_2$@Thio-Yne** as a purple powder analyzed by XPS, UV-vis, and FT-IR analysis.

UV-vis

In Fig 3.23 a and b the UV-vis absorption spectra of **Au-SiO$_2$@Thio-Yne-a** and **b** are reported. The sample **SiO$_2$@Thio-Yne** does not absorb in this region and both samples show a SPR band at 536 nm and 530 nm for **Au-SiO$_2$@Thio-Yne-a** and **b,** respectively.

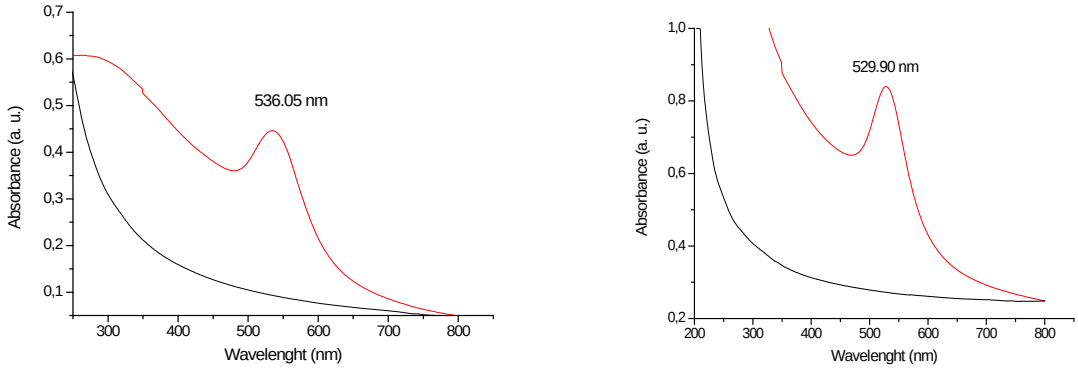

Figure 3.23 UV-vis spectra for **a) Au-SiO$_2$@Thio-Ynea b) Au-SiO$_2$@Thio-Yne-b.**

TEM ***Au-SiO$_2$@Thio-Yne***

The TEM images reported in Figs. 3.24 and 3.25 clearly revealed, unlike what observed for **Au-SiO$_2$@Yne**, the presence of both silica-attached-Au$_{NPs}$ (evidenced by the enlargement Fig. 3.24 e) and free Au$_{NPs}$. With regard to the **Au-SiO$_2$@Thio-Yne-b** samples, the average diameter of the Au$_{NPs}$ attached on the silica surface and that of the "free Au$_{NPs}$" is identical and equal to ca. 11 nm. All the particles are spherical in shape and are often located close to each other in a geminal form.

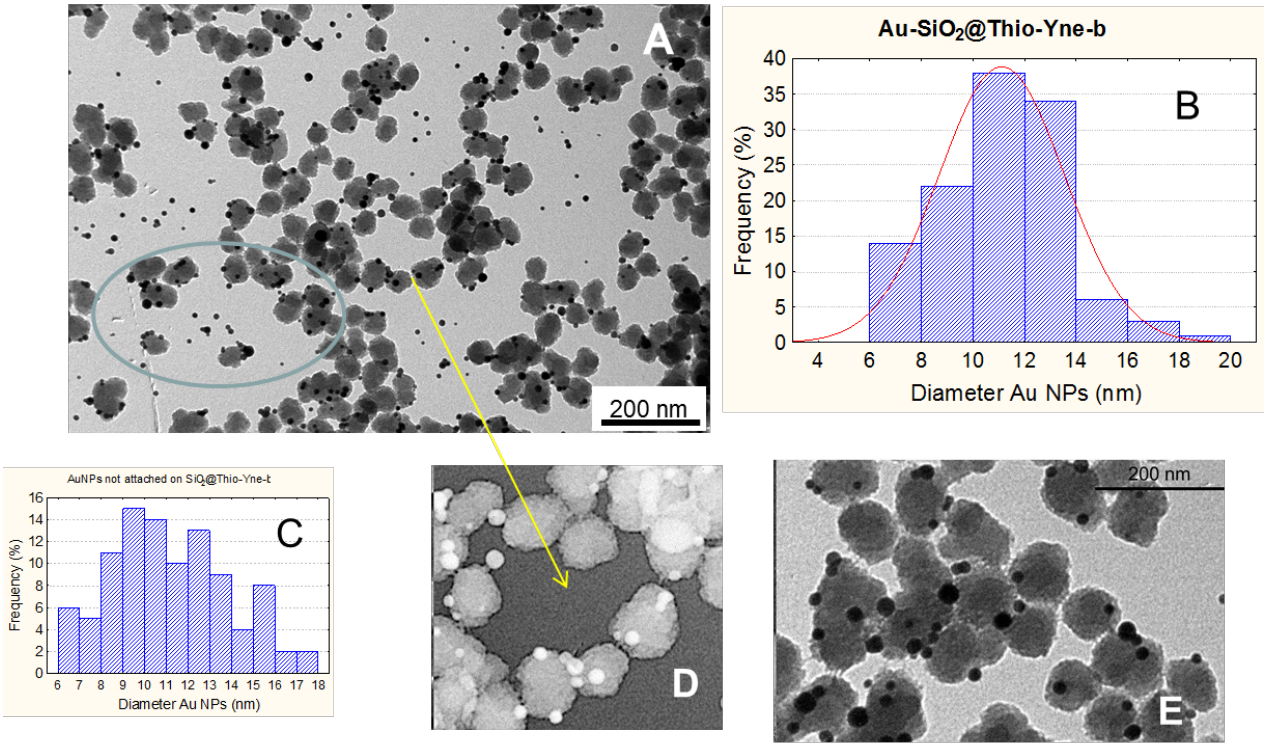

Figure 3.24 TEM micrograph of a) **Au-SiO$_2$@Thio-Yne-b** b) histograms of particle size distribution of the Au$_{NPs}$ attached on silica and of **c)** Au$_{NPs}$ not anchored on silica; **d)** enlargement in negative mode.

.

Overall, in **Au-SiO$_2$@Thio-Yne-b** the gold nanoparticles appear more distributed on the silica surface compared to the **Au-SiO$_2$@Yne-b** system. In fact, in the former case, the ammonium ions present on the silica surface can trap electrostatically the $AuCl_4^-$ ions resulting in a widespread distribution of Au(III) on the system, that is hence first efficiently complexed and then reduced to Au(0).

In **Au-SiO$_2$@Thio-yne-a** the anchored Au_{NPs} are larger (see Table 3.16) with an average diameter of ca. 24 nm (almost twice the previous obtained nanoparticles) and the percentage of "free Au_{NPs}" is almost negligible. The difference in dimensions suggests that in the **Au-SiO$_2$@Thio-yne-b** system the nucleation process is more favoured.

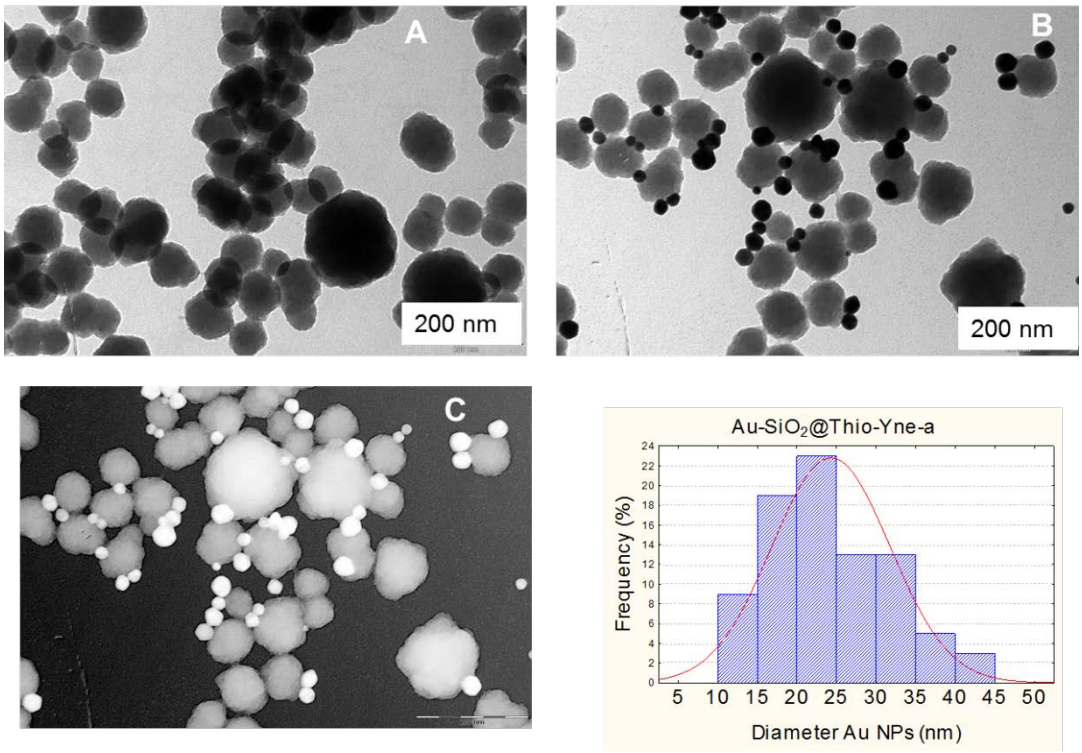

Figure 3.25 TEM micrographs of Au-SiO$_2$@Thio-Yne-a a) before the synthesis; b) after the reaction; c) the TEM picture in negative mode and f) and histograms of particle size distribution.

Table 3.16 Comparison of average diameter calculated by TEM and maximum absorbance wevalenght position in the UV-vis spectra for **SiO$_2$@Thio-Yne-a** and **b** samples.

Sample	λ_{max}	Au TEM (nm)[b]
SiO$_2$@Thio-Yne-a	536	24.2 ±7.4
SiO$_2$@Thio-Yne-b	530	11.3 ± 2.4

FT-IR analysis

FT-IR spectra are reported in Fig. 3.26. FT-IR spectra of **Au-SiO$_2$@Thio-Yne** shows an evident change in the intensity in the bands associated to carbamate moieties with respect to **SiO$_2$@Thio-yne**. The enlargement of the spectra window from 1700 to 1200 cm^{-1} evidences the disappearance of the band at 1446 cm^{-1} in **Au-SiO$_2$@Thio-Yne** and a new weak band formation at 1400 cm^{-1}, ascribed to the S=O stretching, suggesting oxidation of the sulfide to a sulfoxide moiety (see the XPS analysis). Both samples **a** and **b** showed similar bands, reported in the appendix.

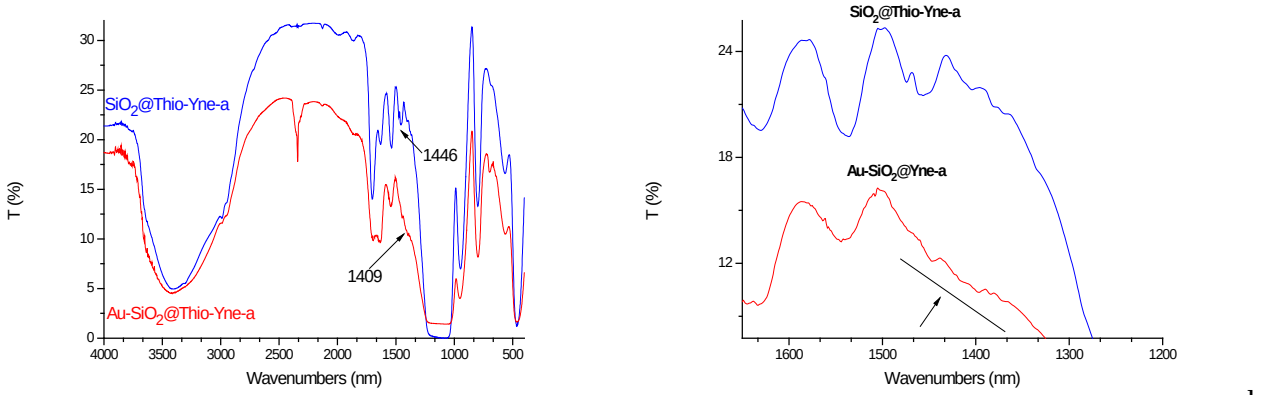

a b

Figure 3.26 a) FT-IR spectra comparing **Au-SiO$_2$@Thio-Yne-a** (red line) with **SiO$_2$@Thio-Yne-a** (blue line); **b)** enlargement of the spectra window from 1700 to 1200 cm^{-1}, evidencing the disappearance of the band at 1446 cm^{-1} in **Au-SiO$_2$@Thio-Yne,** with a new band formation at 1400 cm^{-1}.

*XPS **Au-SiO$_2$@Thio-Yne***

Survey XPS spectra of **Au-SiO$_2$@Thio-Yne** show the presence of the band at 84.3 eV ascribed to gold (Au 4f$_{7/2}$), with similar load of gold for **a** and **b**. Also in these samples in the Au 4f$_{7/2}$ peaks only metallic gold is present.

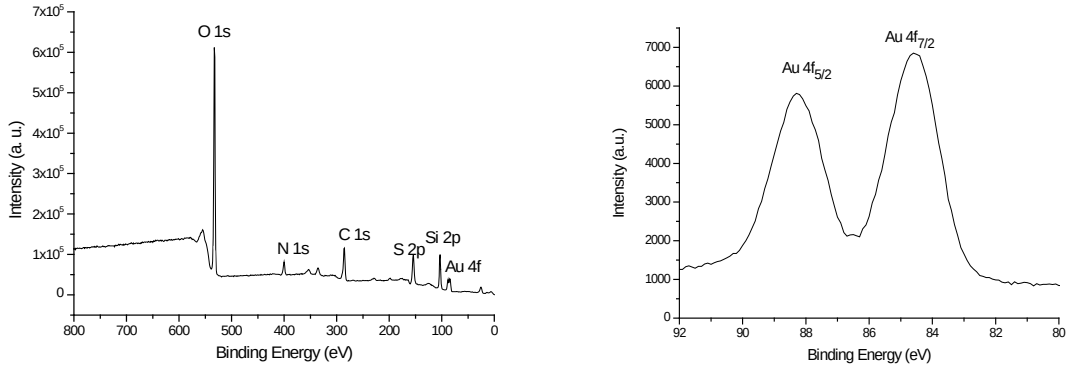

Figure 3.27 XPS survey spectra of **Au-SiO$_2$@Thio-Yne-a**; **b)** XPS spectra of the Au 4f level in **Au-SiO$_2$@Thio-Yne-a**.

For the sake of knowledge, the elemental composition of **Au-SiO_2@Thio-Yne-a** was compared with the % of the starting material **SiO_2@Thio-Yne-a,** before the addition of Au(III) (Table 3.17). The XPS results for sample **Au-SiO_2@Thio-Yne-b** will be reported in the appendix.

Table 3.17 XPS atomic percentage (at %) comparison of **Au-SiO_2@Thio-Yne-a** and **SiO_2@Thio-Yne-a.**

Element	BE	**Au-SiO_2@Thio-Yne-a**
Si 2p	103.3	18.9
O 1s	532.6	47.5
N 1s	400.0	4.8
N 1s (O=C)-NH-C	400.0	4.0
N 1s -NH_3^+	402.0	0.8
C 1s	285.3	26.9
C 1s C-C, C-H	285.0	13.6
C 1s C-O, C-N	286.4	9.9
C 1s O=C-O	289.6	2.0
C new	287.8	1.3
S 2p	163.6	1.0
S 2p S-C	163.6	0.8
S new (S=O) 2p	168.1	0.2
Cl 2p	198.0	0.3
Au 4f	84.5	0.7

Element	**SiO_2@Thio-Yne-a**
Si 2p	18.3
O 1s	42.8
N 1s	5.1
N 1s (O=C)-NH-C	3.7
N 1s -NH_3^+	1.4
C 1s	31.4
C 1s C-C, C-H	17.1
C 1s C-O, C-N, C-S	11.5
C 1s O=C-O	2.8
S 2p	1.5
Cl 2p	0.9

Comparing the results of the two samples, an increase in the oxygen and a decrease in the carbon contents can be observed in **Au-SiO_2@Thio-Yne-a**, where the ratio O/C_{tot} changes from an initial value of 1.8 to 1.4 after the addition of the gold precursor. In **Au-SiO_2@Thio-Yne-a** the deconvoluted C 1s peak, in addition to the bands at 285.0, 286.4, and 289.5 eV (corresponding to C-C; CO, C-N, C-S and C=O) shows a new band at 287.8 (Fig. 3.28). By dividing the area under the carbon peaks (C-N, C-O,C-S; C=O; C-C or the carbon new species) with the sum of C 1s area, a consistent increase in C-C content and a slight decrease for C=O of carbamate respect to **SiO_2@Thio-Yne-a** was observed, with the additional formation of a new component with a BE characteristic of carbonyl groups.

Table 3.18 XPS C1s composition percentage for **Au-SiO_2@Thio-Yne-a** and **SiO_2@Thio-Yne-a**.

Au-SiO_2@Thio-Yne-a	BE (eV)	**Au-SiO_2@Thio-Yne-a**	**SiO_2@Thio-Yne-a**
C 1s C-C, C-H	285.0	50.7	54.5
C 1s C-O, C-N	286.4	36.8	36.7
C 1s O=C-O	289.6	7.7	8.8
New C 1s	287.8	4.8	-

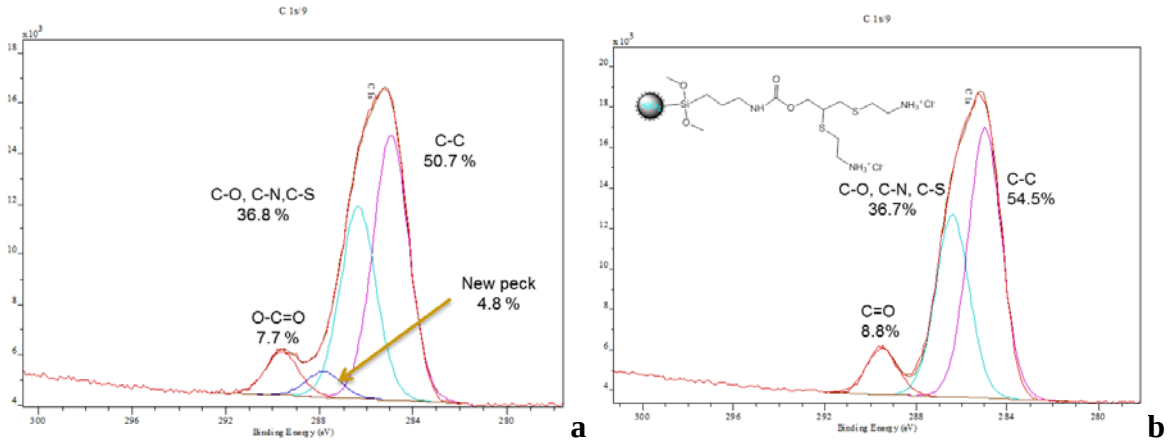

Figure 3.28 XPS C1s spectrum and carbon composition percentage **a)Au-SiO_2@Thio-Yne-a b) SiO_2@Thio-Yne-a.**

The N 1s peak, as for **SiO_2@Thio-Yne,** was resolved into two bands at 399.9 and 401.7 eV corresponding to the O-C=O of carbamate and NH_3^+ of the bis-sulfide adducts (Fig 3.34). In **Au-SiO_2@Thio-Yne** an increase in NH-C=O content was observed: this can suggest that some NH_3^+ groups could be neutralized (during the repeated cycles of centrifugation and washing with water and ethanol) with formation of the corrisponding primary amines. The binding energy of amines, as reported in the literature, is around 399 eV[19] and in this case these species will be included in the area under the peak of NH-C=O, where the deconvolution of the peak cannot distinguish between the two species.

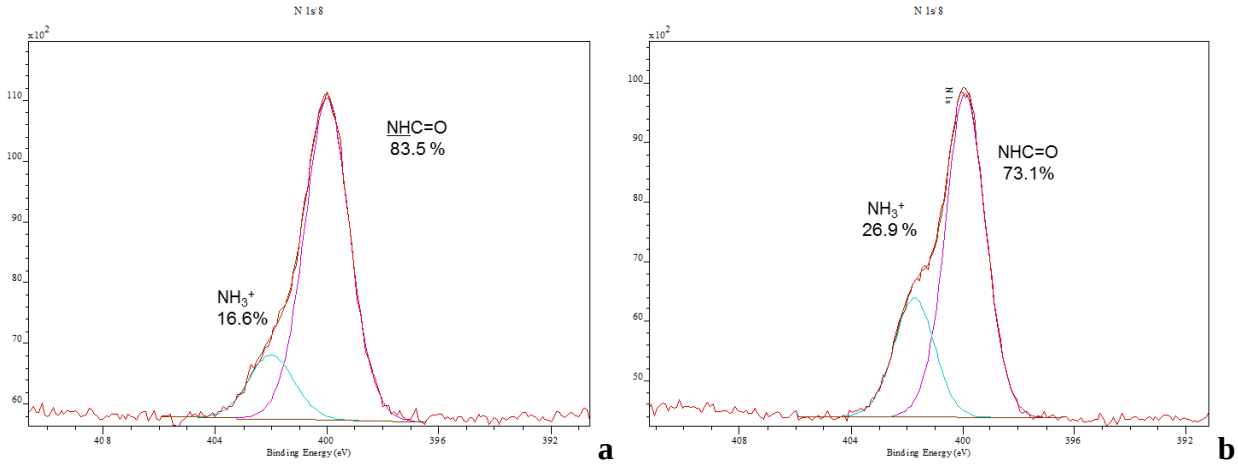

Figure 3.29: N 1s XPS spectrum **a)Au- SiO_2@Thio-Yne-a; b) SiO_2@Thio-Yne-a**.

The S 2p peak at 163 eV in **Au-SiO_2@Thio-Yne** was deconvoluted into two peaks respectively at 168.1 and 163.7 eV. The second peak is present also in **SiO_2@Thio-Yne** and it was associated to S-C bonds. The other one is not present in **SiO_2@Thio-Yne** and this binding energy is ascribed to S=O formation. The percentage in composition of S-C and S=O in **Au-SiO_2@Thio-Yne-a** is 82 % and 18 %, respectively (Table 3.19).

Table 3.19 XPS S 2p composition percentage for **Au-SiO$_2$@Thio-Yne-a**.

S 2p	BE (eV)	**Au-SiO$_2$@Thio-Yne-a**
S-C	163.6	81.8
S=O	168.1	18.2

Form these results it seems that two new species are formed: one from the sulfide and the other by the carbamate moiety. The percentage of S=O formed, with respect to the new carbon species, is ca. 13 %. We suggest that the two species are obtained by two different mechanisms. The new carbon species observed in the deconvolution of C1s spectra has a binding energy tipical of carbonyl groups and similar to the BE observed for the new peak in **Au-SiO$_2$@Yne** spectra. This product is due to the reaction of the alkynes groups activated by gold, as discussed in the previous mechanism for **Au-SiO$_2$@Yne** (Scheme 3.9).

Table 3.20 Ratio of the elemental composition (at %)

Entry	Ratio	**SiO$_2$-Thio-Yne-a**
1	S-C/NH_3^+	0.9
2	NH_3^+/NH-C=O	0.2
3	NH-C=O/C=O	2.0
4	NH_3^+/Cl^-	2.7
5	Si/O	0.4
6	Si/N(tot)	3.9
7	C=O/Au	2.8
8	C new /Au	1.8
9	S=O/C-S	3.8

The oxidized form of sulfur, on the contrary, arises by oxidation of the bis-sulfide adducts (Scheme 3.10). A very similar reaction was reported by Cattalini et Al. in 1975, where l-methionine, in the presence of chloroauric aqueous solution, gave optically pure sulfones.[20] The suggested mechanism included displacement of a chlorine atom of the Au(III) compound by the sulfide, oxidation of the latter to sulfone with concomitant reduction of Au(III) to Au(I), and eventual disproportionation of Au(I) to Au(0) and again Au(III).

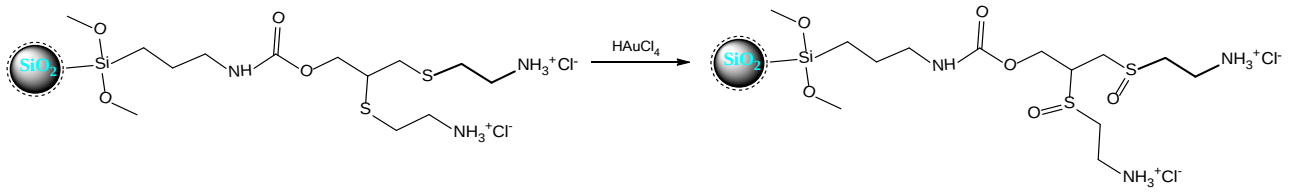

Scheme 3.10

3.2 Conclusions

Silica nanoparticles functionalized with alkynyl carbamate moieties (**SiO_2@Yne**) were synthesized by condensation of a difunctional organosilane, PPTEOS, with TEOS in alkaline medium. By simply performing the synthesis with different amounts of NH_4OH, two kinds of **SiO_2@Yne** were prepared: S**iO_2@Yne-a** and **b.** Spherical alkyne functionalized silica nanoparticles with a raspberry-like structure and different size distributions were obtained. In the case of **SiO_2@Yne-a** (higher amounts of NH_4OH) the average size was 79 ± 24 nm, whereas for **SiO_2@Yne-b** (lower NH_4OH concentration) the average size was 45 ± 6 nm. The most uniform particles size distribution was detected for **SiO_2@Yne-b**.

SiO_2@Yne-a and **b** were post-functionalized with cysteamine hydrochloride to obtain amino-sulfide branches (**SiO_2@Thio-Yne-a** and **b**) by using a click-chemistry approach, i.e. the radical "thiol-yne coupling" (TYC) reaction. An incomplete conversion of the alkyne moieties to bis-sulfide adducts was observed in both samples. Since, unfortunately, this brings about problems in understanding the behaviour of these new materials in formation and support of gold nanoparticles, alternative synthetic roots are currently under investigation to improve the degree of functionalization.

By adding the obtained materials to an aqueous solution of $HAuCl_4$ spontaneous formation of Au_{NPs} was observed in both cases and in very short times. In **Au-SiO_2@Yne-a** and **b** Au_{NPs} of about 11 nm anchored on silica surface were obtained. XPS results revealed a change in structure on the carbamic functionality. Hence, a rearrangement mechanism involving addition of the carbamic nitrogen to the alkyne moieties activated by Au(III) with formation of an imine derivative was suggested. The final rearranged product can account, in the aqueous medium, for formation of reduced gold (Au_{NPs}) and carbonyl compounds (aldehydes).

In the **Au-SiO_2@Thio-Yne** systems Au_{NPs} (of about 24 nm for **Au-SiO_2@Thio-Yne-a**, and 11 nm for **Au-SiO_2@Thio-Yne-b**) appear more distributed on the silica surface compared to the **Au-SiO_2@Yne** system: this is probably the result of the presence of the ammonium ions anchored to the silica surface, which can electrostatically trap the $AuCl_4^-$ ions giving a widespread distribution of Au(III), and hence of the eventual Au_{NPs}, on the system. Sound conclusions on the reduction mechanism cannot be drawn, due to the concomitant presence on the silica of both aminosulfide and alkyne moieties, which makes the system too complicated to be rationalized. Efforts are hence underway to devise a clean synthesis of cysteamine-functionalized silica.

3.3 Experimental Section

3.3.1 Materials

$HAuCl_4 \cdot 3H_2O$ was prepared as reported previously.[21] 3-(Triethoxysilyl)propyl isocyanate (IPTEOS) (95%), Tetraethoxysilane, (TEOS) (99%), propargyl alcohol (99%), ethanol (99%), dichloromethane (DCM, 99%), triethylamine (TEA, 99%), Cysteamine hydrochloride (98 %), 2-dimethoxy-2-phenylacetophenone (DMPA) were purchased from Aldrich and used as received. Ammonia hydroxide solution (28%) was purchased from Carlo Erba. Ultrapure water purified with the Milli-Q plus system (Millipore Co, resistivity over 18 MΩ cm) was used in all cases. EtOH was boiled and stored under N_2 prior to use under N_2. Centrifuge (ALC 4239R).

3.3.2 Synthesis of [3-(2-Propynylcarbamate)propyl]triethoxysilane

Synthesis of the alkyne-terminated organo-silane PPTEOS was performed according to described procedure.[3] In a dry round bottom flask a solution of propargyl alcohol (1,16 mL, 20 mmol) and TEA (2,4 mL, 18 mmol) in 20 mL of DCM was prepared under nitrogen and cooled in an ice bath. IPTEOS (4,45 g, 18 mmol), dissolved in 10 mL of DCM, was added drop wise under nitrogen. The reaction mixture was allowed to stir for 24 h at room temperature and monitored by TLC (7/3 Ethylic Ether/ Petroleum Ether). When the starting materials were not more presented, the mixture were evaporated under reduced pressure to afford PPTEOS as an orange oil (88 %).

^{1}H NMR (300.1 MHz, $CDCl_3$): δ 0.59 (t, 2H, CH_2Si); 1.19 (t, 9H, $OCH_2\underline{CH_3}$); 1.59 (m, 2H, CH_2CH_2NH); 2.43 (t, 1H, CH); 3.20 (m, 2H, CH_2NH); 3.82 (q, 6H, CH_2O); 4.63 (d, 2H,CH_2-C≡C); 5.15 (bs, 1H, NH).

^{13}C NMR (75.50 MHz, CDCl3): 155.65 (NHCO); 78.55 (C≡CH); 74.56 (C≡CH), 58.48 (3 CH_2), .52.26 ($\underline{CH_2}$-C≡CH), 43.59 (NH-CH_2), 23.24 (CH_2), 18.30 (3 CH_3); 7.65 (CH_2-Si

ESI-MS (MeOH, m/z): $[M]^{+1}$ 304; (MeOH, Ammonium chloride, m/z): $[M]^{NH4+}$ 321

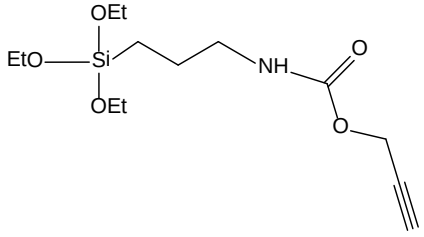

PPTEOS

3.3.3 General preparation of Alkyne-Functionalized Silica Nanoparticles (SiO_2@Yne)

Alkyne-modifies silica nanoparticles (**SiO_2@Yne**) were prepared according to the Stöber method, following a reported procedure with some modifications.[22] The synthesis was performed using two different concentration of ammonia solution.

A two-neck dry round bottom flask of 100 mL was charged with TEOS (2.0 mL, 9.38 mmol) and 50 mL of EtOH. PPTEOS (0.666 g, 2.20 mmol), previously dissolved in 15 mL of EtOH was added to the vigorously stirred mixture under nitrogen, thermostated at 40 °C. Once the system reach the desired temperature. NH_4OH was added to the solution as a basic catalyst. In order to investigate the effect of NH_4OH concentration on the size of **SiO_2-Yne**, two different volumes of ammonia hydroxide solution (28 %) were used: 10 mL (0.145 mol) for **SiO_2@Yne-a** samples and 3.4 mL (0.05 mol) for **SiO_2@Yne-b** (0.05 mol), respectively. The reaction mixture was allowed to stir for 24 h at 40 °C. After the addition of ammonia solution becomes gradually milky white, which corresponds to the silica nanoparticles formation. In the case of **SiO_2@Yne-a** (10 mL of ammonia added) this phenomenon is evident after 2 minutes; whereas for **SiO_2@Yne-b** only after 2 h. After the reaction was completed, the obtained **SiO_2@Yne** were separated by centrifugation at 7800 rpm for 1h and re-dispersed in EtOH using a bath sonicator (thrice). The removed EtOH solution was concentrated under reduced pressure and weighted to determine the amount of unreacted PPTEOS. The **SiO_2@Yne** dispersion can be conserved in EtOH and stored in the dark in the fridge. In order to determine the NPs concentration, 1 mL of dispersion was evaporated and dried, the residue was weighted.

The **SiO_2-Yne** dispersion can be also conserved as dried powder. For this purpose, the sample was concentered under reduced pressure and dried in oven at 50 °C for 3 h and kept under N_2 stream to remove the residual solvent, resulting in a white powder. For the subsequent reaction the dried dispersions were always used in order to avoid the precipitation of nanoparticles on the bottom in dispersion form with change in the concentration.

The **bare-SiO_2** was prepared by the same procedure using TEOS (2 mL, 9.38 mmol) without addition of PPTEOS.

3.3.4 Thiol-yne reaction on with propargyl alcohol and cysteamine hydrochloride

In a 100 mL two-neck round bottom flask under nitrogen atmosphere, propargyl alcohol (0.5 mmol; 30 µl) and cysteamine hydrochloride (1 mmol, 0.113 g) were solubilized in 6 mL of solvent. Different solvent were used: ethanol, toluene and water. DMPA (0.1 mmol, 2.6 mg) was added to the mixture as photoiniziator and the reaction was initiated by exposition to UV-light for 3 h. At the end of the reaction the mixture was reduced in concentration, and analyzed, without further purification.

^{1}H NMR (300.1 MHz, $CDCl_3$): δ 3.80 (d, 2H, CH); 3.26 (t, 4 H, CH_2), 3,09 – 2,84 (m, 7 H).
ESI-MS (MeOH, m/z): $[M]^{+1}$ 211.

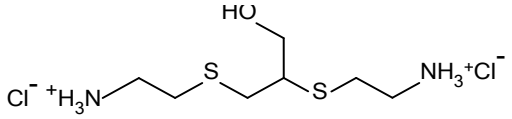

3.3.5 General method to prepare SiO_2@Thio-Yne

In a 50 mL two-neck round bottom flask under nitrogen atmosphere 100 mg of dry **SiO_2@Yne** were dispersed in 8 mL of ethanol by bath sonicator during 10 minutes. Once the powder looked completely dispersed, 75 mg of cysteamine hydrochloride (0.64 mmol) and 15 mg of DMPA (0.06 mmol) were added to the system and irradiated with a 365 nm light by an UV lamp for 3 h, under vigorous stirring. During the reaction the **SiO_2@Yne** white dispersion starts to gain an increasing light-yellow color.

As cysteamine presence in solution can result in by-products formation of non-reactive disolphure cysteamine derivatives, a second approach was used: method (ii).

According to method (ii) cysteamine hydrochloride was added in portions in course of the reaction (25 mg every 30 minutes, 75 mg in total) to the system (100 mg **SiO_2@Yne** and 15 mg DMPA in 8 mL ethanol). In contrast to the first approach, in which all cysteamine hydrochloride were added once in the beginning of reaction, this way its addition was made in portions during the first 1.5 h of the reaction, and the reaction was maintained for another 1.5 h. The obtained **SiO_2@Thio-Yne** were isolated by centrifugation (3000 rpm x 30 min). The supernatant was removed and **SiO_2@Thio-Yne** was redispersed thrice: in EtOH, in water and then again EtOH using a bath sonicator. The **SiO_2@Thio-Yne** were dried under a stream of nitrogen and kept in oven at 50 °C for 2 h.

3.3.6 Synthesis of Au-SiO_2@Yne and Au-SiO_2@Thio-yne

The same procedure for all the obtained silica (**SiO_2@Yne-a** and **b**; **SiO_2@Thio-Yne** a and **b**; **bare-SiO_2**) was used. Typically in a 50 mL Pyrex glass, in a ultrasonic bath, 80 mg of functionalized silica and 20 mL of ultrapure water were added. After the first 10 minutes needed to disperse the solid completely, (in order to obtain an homogenous system) 20 mL of $HAuCl_4$ 1 mM were added to the dispersion. The reaction was carried out in the ultrasonic bath for other 30 minutes, maintaining the temperature around 30-35 °C. Since the first minutes of the reaction changes in color are observed for the functionalized silica and not for bare-silica. After the first 10 minutes in **SiO_2@Yne** systems, an initial violet colour take place and gradually change in red-purple. In **SiO_2@Thiol-yne** dispersion soon as it is introduced the precursor a yellow and intense orange is detected, that gradually, in 20 minutes, changes to red-purple.

At the end of the reaction, the obtained **Au-SiO_2@Yne-a** and **b** or **Au-SiO_2@Thio-Yne-a** and **b** were separated by centrifugation at 6000 rpm for 30 minutes and re-dispersed twice in water and twice in EtOH using a bath sonicator. The collected functionalized-silica was dried by an intense flux of N_2 and conserved in oven for 4 h at 50°C. The obtained powder were analyzed for XPS analysis. For TEM analysis the sample was analyzed without farther purification.

3.3.7 Characterization

Thermogravimetric analysis were carried out using a Perkin Elmer TGA-7. Heating was performed in a platinum crucible at a rate of 10 °C/min from 20 °C to 900 °C. The samples weights were in the range 5–10 mg.

UV absorbance spectra were recorded on a Varian Cary 100 Bio UV-Vis spectrophotometer, Spectra in EtOH or in water.

The XPS analyses were performed using a Kratos Analytical AXIS UltraDLD spectrometer, Monochromatized aluminum source (AlKα = 1486,6 eV) was used for excitation. The analyzer was operated in constant pass energy of 40 eV using an analysis area of approximately 700 µm × 300 µm, Charge compensation was applied to compensate for the charging effect occurring during the analysis. Quantification of the experimental photopeaks was carried out using the CasaXPS software taking into account a linear background subtraction.

DLS and potential measurements were performed using a Malvern Zeta series, the measurement were done on dispersion in ethanol or water.

For TEM investigations a Philips CM 100 transmission electron microscope operating at 80 kV was used. To prepare the sample a drop of the suspension was transferred onto holey carbon foils supported on conventional copper microgrids.

FT-IR spectra were recorded under a nitrogen atmosphere in the range 4000÷400 cm^{-1} using a Perkin Elmer Spectrum 2000 spectrophotometer; the samples (2-3 mg) were grinded into a fine powder and pelletized with KBr (200 mg).

The NMR spectra were recording using a Varian Inova (^{1}H 300,1; ^{13}C 75,5 MHz). The spectra were referenced internally to residual solvent resonances and they were recorded at 298 K for characterization proposes, full ^{1}H and ^{13}C NMR assignments were done.

ESI-MS analysis were performed by direct injection of methanol solutions of the compounds in methanol solutions using a WATERS ZQ 4000 mass spectrometer.

3.4 Appendix

3.4.1 SiO_2@Thio-Yne Thermograms

TGA thermogram obtained for **SiO_2@Thio-Yne-a** by method (i), and comparison with the respective **SiO_2@Yne-a.**

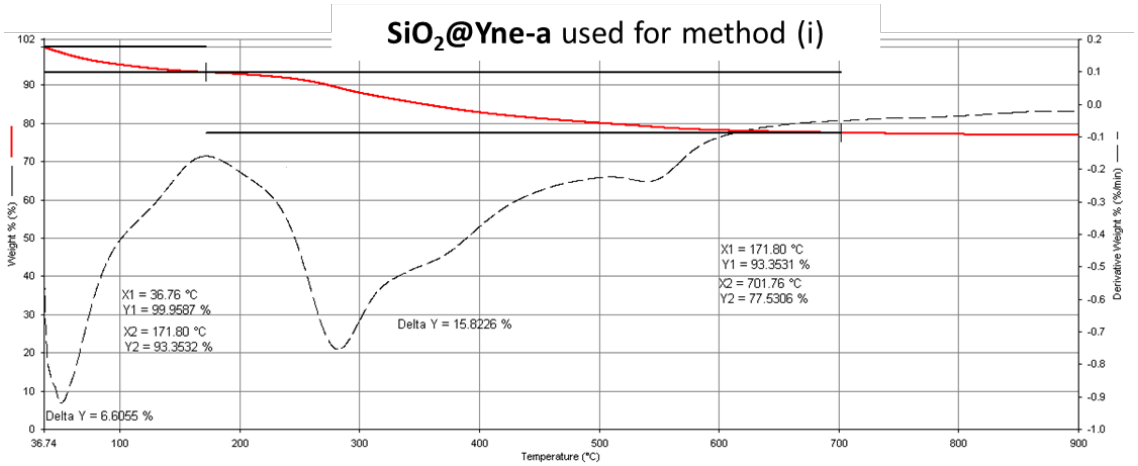

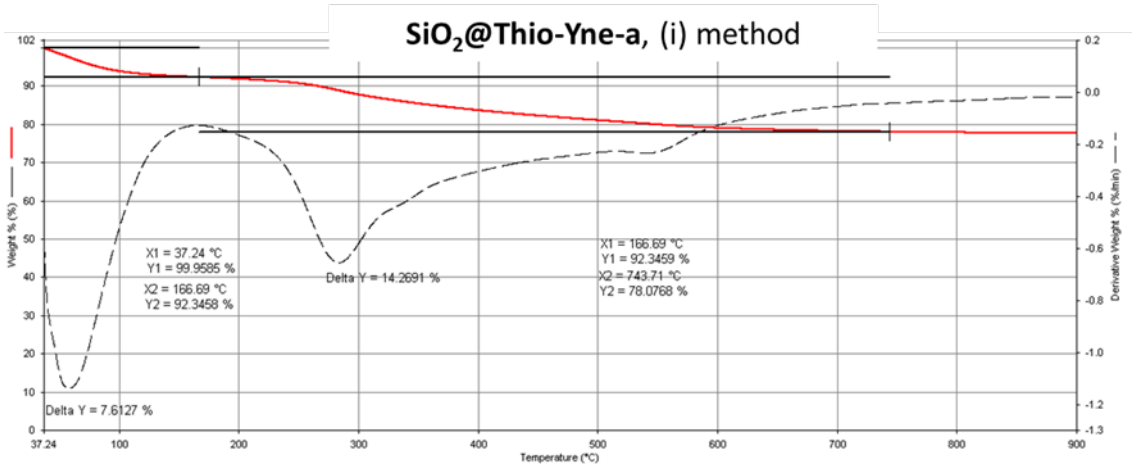

TGA thermograms for samples **SiO_2@Thio-Yne-a** and **b** by the method (ii) are reported. In both spectra in the range from 200 to 600 °C three maxima are highlighted by the first derivatives of the weight percentage (dotted line). The range of temperature that includes these maxima are: 30 – 150 °C (losses in water and ethanol), 150 - 320 ° C (organic material), 320-450°C (organic fraction); the third 450-730 °C (loss due to hydrolysis of silica).

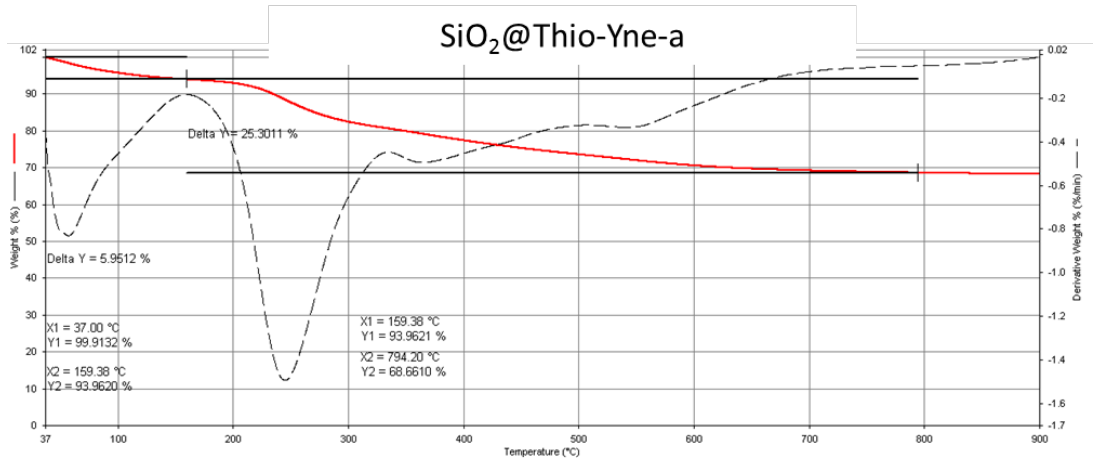

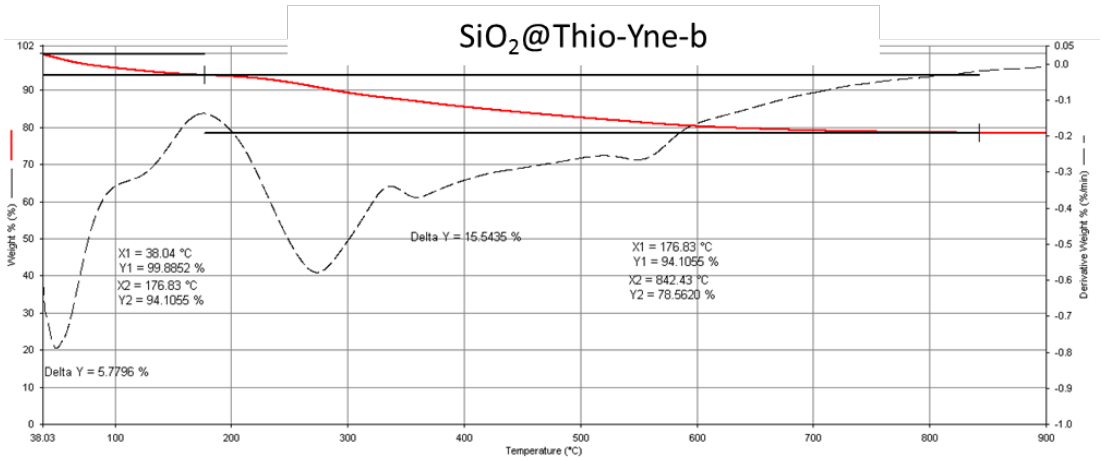

3.4.2 NMR and ES-MS spectra

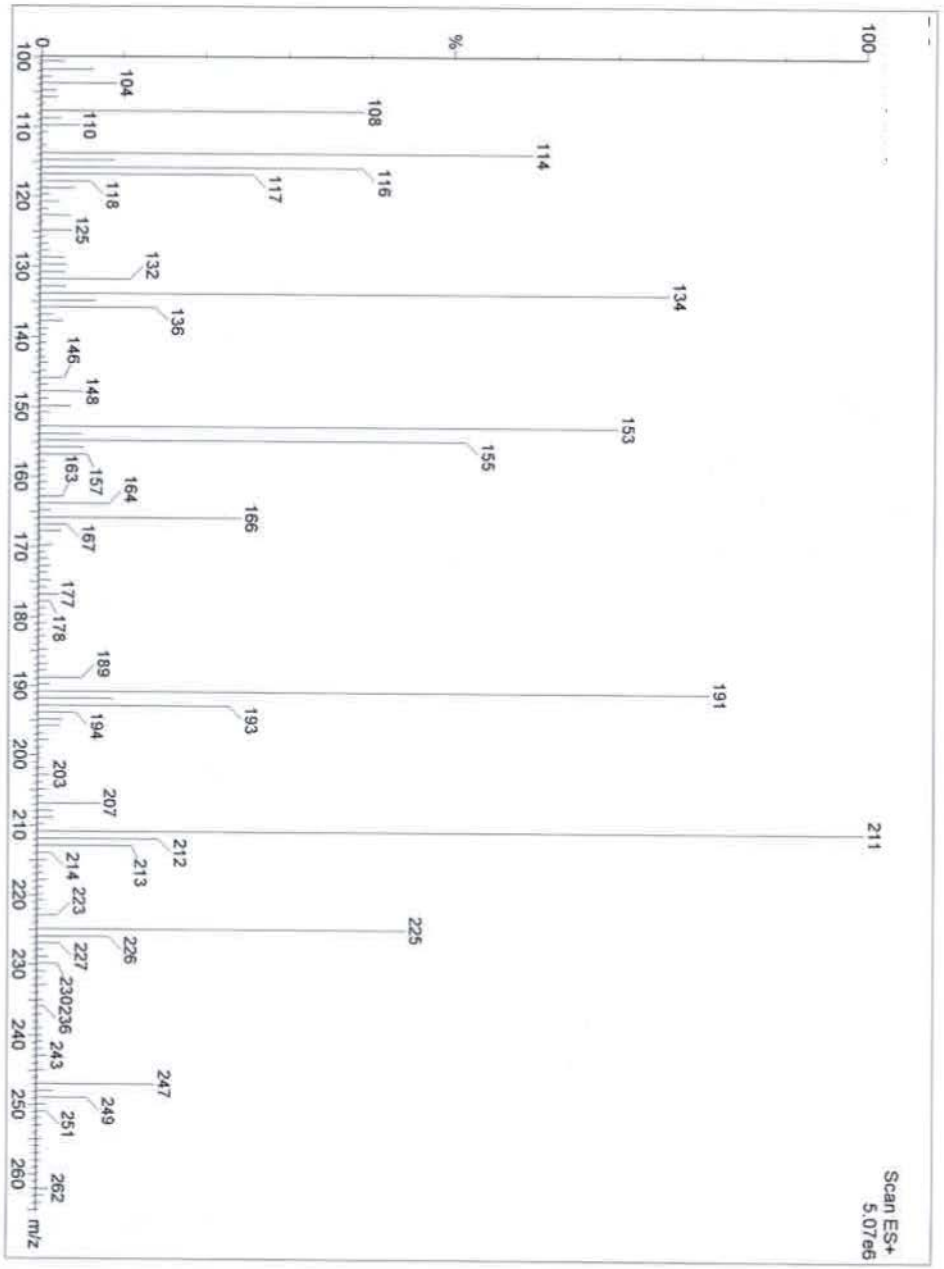

3.4.3 XPS DATA

SiO_2@Yne

Table 3.21 Elemental analysis composition (at %) for **SiO_2@Yne-a** and **SiO_2@Yne-b**, more percentage concentration of the three components of C 1s obtained by deconvolution of C 1s.

Samples	Si 2p (at %) 103.3±0.1 (eV)	O 1s (at %) 532.8±0.1 (eV)	N 1s (at %) 400.1±0.1 (eV)	C 1s (at %)[a] 285.2±0.1 (eV)	C-N, C-O[b] 289.5±0.1 (eV)	C-C[b] 285.0 ±0.1 (eV)	C=O[b] 289.76 ±0.1 (eV)
SiO_2@ Yne-a	19.2	49.7	3.8	27.4	7.3	17.0	3.2
SiO_2@ Yne-b	22.3	51.3	3.1	25.3	7.2	15.0	3.0

Au-SiO_2@Thio-Yne-b

Table 3.22 Elemental analysis composition (at %) for **Au-SiO_2@Thio-Yne-b**.

Element	**BE (eV)**	**Au-SiO_2@Thio-Yne-b (at %)**
Si 2p	103.5	21.9
O 1s	532.7	53.4
N 1s	400.0	3.7
N 1s (O=C)-NH-C	400.0	3.2
N 1s -NH_3^+	402.0	0.6
C 1s	285.4	20.0
C 1s C-C, C-H	285.0	10.2
C 1s C-O, C-N	286.4	7.1
C 1s O=C-O	289.6	1.6
C new	287.8	1.0
S 2p	164.1	0.3
S 2p S-C	164.6	0.24
S new (S=O) 2p	168.1	0.06
Cl 2p	198.7	0.1
Au 4f	84.0	0.5

Table 3.23 XPS C 1s composition percentage for **Au-SiO_2@Thio-Yne-b** and **SiO_2@Thio-Yne-b**.

Au-SiO_2@Thio-Yne-a	BE (eV)	**Au-SiO_2@Thio-Yne-b**	**SiO_2@Thio-Yne-a**
C 1s C-C, C-H	284.9	50.9	54.6
C 1s C-O, C-N	286.4	35.7	35.9
C 1s O=C-O	289.6	8.2	9.5
New C 1s	287.8	5.2	-

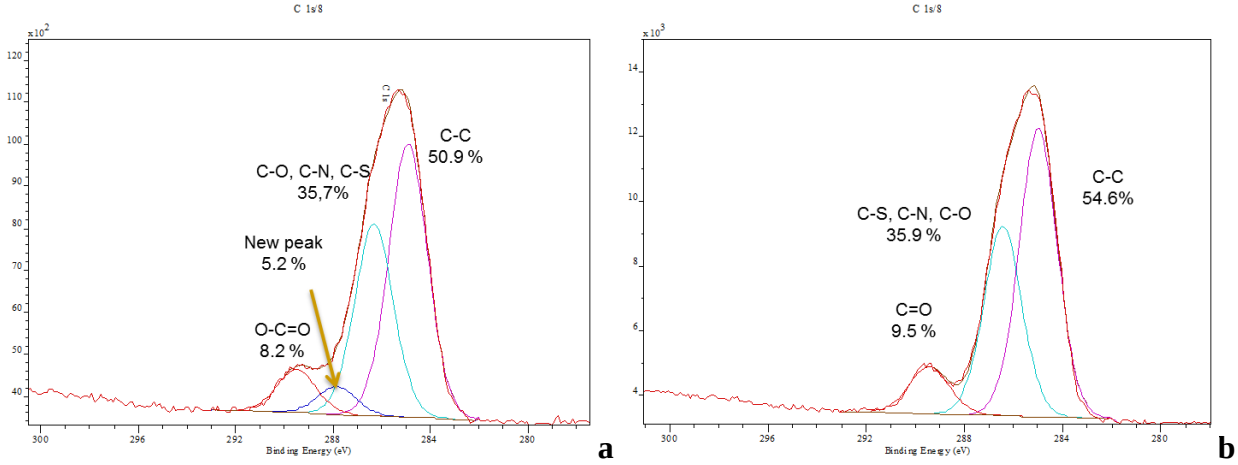

Figure 3.30 XPS C 1s spectrum and carbon composition percentage **a)Au-SiO_2@Thio-Yne-b**; **b) SiO_2@Thio-Yne-b.**

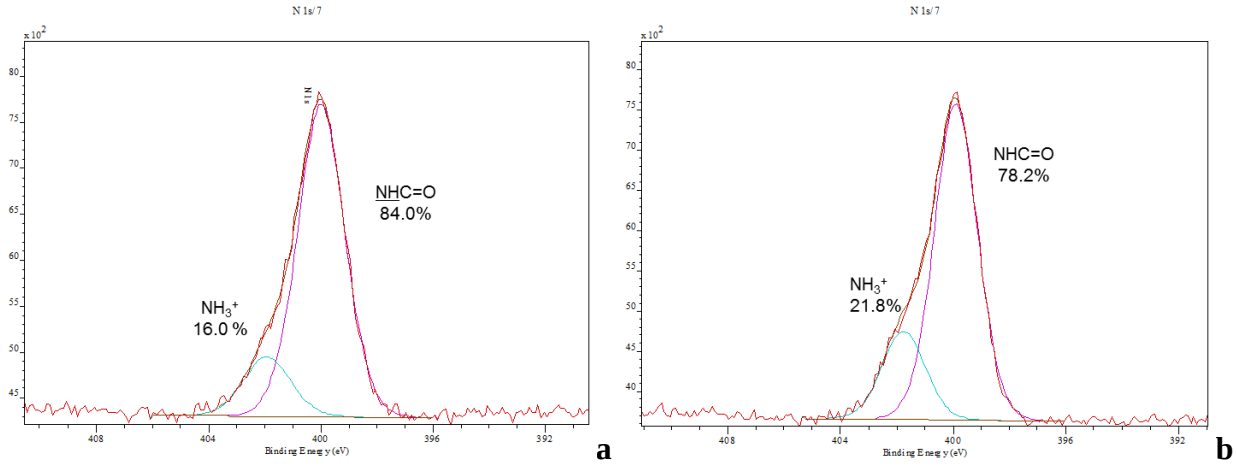

Figure 3.31 XPS N 1s spectrum and carbon composition percentage **a)Au-SiO_2@Thio-Yne-b; b) Au-SiO_2@Thio-Yne.**

Table 3.24 XPS S 2p composition percentage for **Au-SiO_2@Thio-Yne-b**.

S 2p	BE (eV)	**Au-SiO_2@Thio-Yne-a**
S-C	163.6	80.4
S=O	168.1	19.6

3.4.4 FT-IR

Comparison of FT-IR spectra between the respective **a** and **b** systems for **Au-SiO_2@Yne**; **Au-SiO_2@Thio-Yne** (Figs. 3.31 and 3.32).

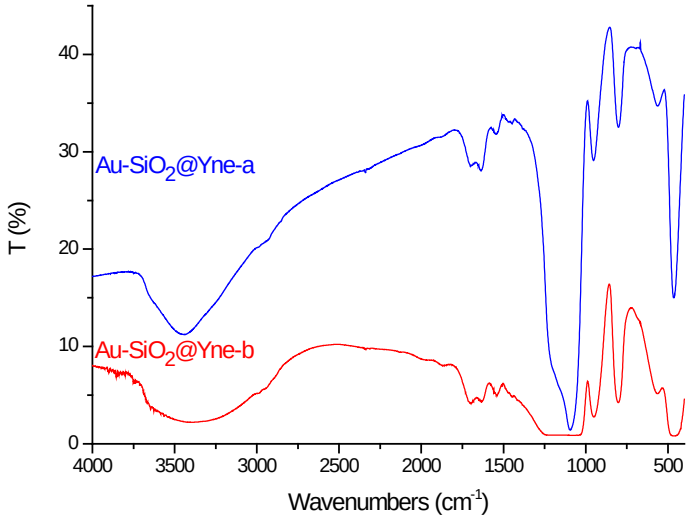

Figure 3.32 FT-IR spectra of **SiO_2@Yne a** and **b**.

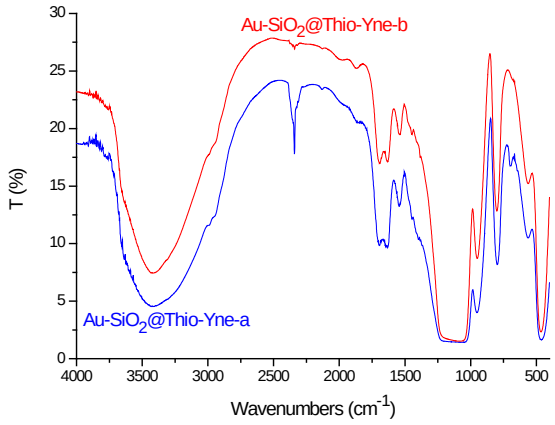

Figure 3.33 FT-IR spectra of **Au-SiO_2@Thio-Yne-a** and **b**.

References

[1] A. Choualeb, J. Ros, P. Braunstein, R. Welter, *Organometallics* **2003**, 22, 2688.

[2] J. Burkus, J. *Org. Chem.* **1961**, 26, 3, 779.

[3] X. Lu, S. Fu, J. Wang, J. Zhiìong, D. Qingzhi, *Macromol. Rapid Commun*, 30, 2116-2120.

[4] *ImageJ*, Image processing and analysis in Java: http://rsb.info.nih.gov/ij/.

[5] W. Stober, A. Fink, *J. Colloid Interface Sci* **1968,** *26*, 62.

[6] J. Lee, Y. Lee, K. Youn Jong, B. Na Hyon, T. Yu, H. Kim, S.-M. Lee,Y.-M. Koo, H. Kwak Ja, G. Park Hyun, N. Chang Ho, M. Hwang,J.-G. Park, J. Kim and T. Hyeon, *Small* **2008**, *4*, 143.

[7] A. Peled, M. Naddaka, J. P. Lellouche, *J. Mater. Chem*. **2011**, *21*, 11511.

[8] KL. Furer, *J. Mol. Struct*. **1998**, 449, 53.

[9] T. Wu, Q. Zhang, J. Hu, G. Zhang, S. Liu, *J. Mater. Chem*. **2012**, *22*, 5155

[10] M. Minozzi, A. Monesi, D. Nanni, P. Spagnolo, N. Marchetti, A. Massi, *J. Org. Chem.* **2011**, *76*, *450*.

[11] M.P. Casaletto, A. Longo, A. Martorana, A. Prestianni, A.M. Venezia, *Surf. Interface Anal.* **2006**, *38*, 215.

[12] M. Brust, M. Walker, D. Bethell, D. J. Shiffrin, R. Whyman, *J. Chem. Soc., Chem. Commun.* **1994**, 801.

[13] N.s Bhairamadgi, S. Gangarapu, M. A. Caipa Campos, J. M. J. Paulusse, C. J. M. van Rijn, H. Zuilhof, *Langmuir* **2013**, *29*, 4535.

[14] Chemistry of Organic Derivatives of Gold and Silver, ed. S. Patai, Z. Rappoport, John Wiley & Sons, **1999**.

[15] L. J, Zhang, *J. Am. Chem. Soc.* **2005**, *127*, 16804.

[16] Li, G.; Zhang, G.; Zhang, *J. Am. Chem. Soc*. **2008**, *130*, 3740.

[17] Shi, F.-Q.; Li, X., Xia, Y.; Zhang, L. Yu, Z.-X, *J. Am. Chem. Soc* **2007**, *129*, 15503.

[18] The Handbook of Infrared and Raman Characteristic Frequencies of Organic Molecules, ed. D. Lin-Vien, N. B. Colthup, W. G.Fately, J. G. Grasseli, Academic Press, New York, **1991**.

[19] A. S. M. Chong, X. S. Zhao, *J. Phys. Chem. B*, **2003**, *107*, 12650.

[20] G. Natile, E. Bordignon, L. Cattalini, *Inorganic Chemistry*, 15, **1976**, 246.

[21] G. Braurer, *Handbook of Preparative Inorganic Chemistry*, Academic Press, New York, **1963**, Vol. II, 1058.

[22] X. Lu, S. Fu, J. Wang, J. Zhiìong, D. Qingzhi, *Macromol. Rapid Commun, 30*, 2116.

CHAPTER 4 116

4. DIRECT INVESTIGATION OF GOLD NANOPARTICLES FORMATION INSIDE A MICROFLUIDIC CHANNEL BY IN SITU XANES SPECTROSCOPY. 116

4.1 Results and Discussion 117

4.1.1 Gold nanoparticles synthesis by a microfluidic set-up 117
4.1.2 Microfluidic setup adapted to *in situ* XANES characterization 119

4.2 Experimental section 124

4.2.1 Materials 124
4.2.2 XAS Data Collection 124

4.3 Conclusion 125

CHAPTER 4

4. Direct investigation of gold nanoparticles formation inside a microfluidic channel by in situ XANES spectroscopy.

In this study the first direct *in situ* time-resolved X-Ray Near Edge Structure (XANES) characterization of gold nanoparticles formation in a microfluidic device was reported. The classic Turkevich gold nanoparticles synthesis (Au_{NPs}) was transposed to a microfluidic set-up and directly investigated by XANES. By taking the advantage of converting a “time scale” to a “length scale” the reaction was followed along different position of the micro-reactor in continual flow. Evidences of the oxidation states and chemical environment of gold atoms in those positions has allowed us to propose a general mechanism of nanoparticle formation during the microfluidic reaction.

4.1 Results and Discussion

4.1.1 Gold nanoparticles synthesis by a microfluidic set-up

During a six month stay at the University of Lille, under the supervision of Dr. J. S. Girardon, I worked on synthesis of colloidal nanoparticles by microfluidic systems.

Girardon et al., in recent publications,[1,2] reported the fine tuning of gold nanoparticle size by the transposition of a classic Turkevich synthesis to a microfluidic device. The microfluidic reactor, made from commercially available items, is made up of two meters of a micro-capillary with an inner diameter of 200 µl of fused silica inside, and a polyimide coted outside in order to have a flexible material. The high surface-volume ratio of the micro-capillary permits quick heating and quenching time in the reaction. The two reagents, $HAuCl_4$ and citrate, are driven inside the micro tube by a syringe pump that regulates the flow rate and the residence time of the reagents inside the micro-channel. Au(III) precursor and citrate are quickly mixed by a T-mixer and driven into the micro-reactor placed spirally on a hot-plate (Fig. 4.1).

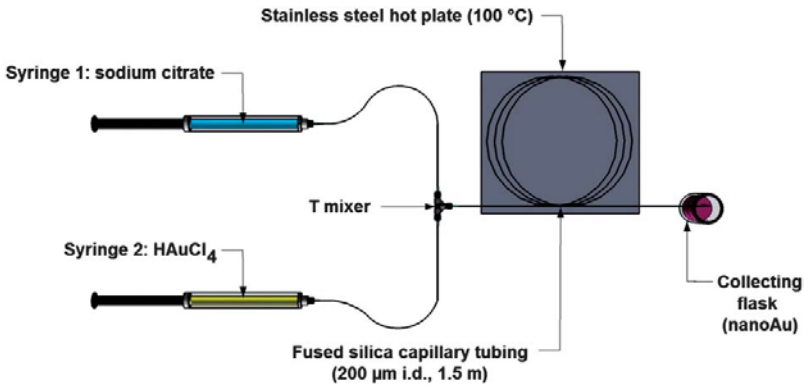

Figure 4.0.1 Two syringes, one containing $HAuCl_4$ (5.4×10^{-3} M) and another sodium citrate solution (16.3×10^{-3} M) were connected by a 15 cm length of silica capillary to a "T" micro-mixer connector in order to introduce the reagents (driven by the syringes pump, not represented) to a silica capillary of 2 m. The capillary with an inner diameter of 200 µm, was positioned on the hot plate.

By using $HAuCl_4$ ten times more concentrated than the classic batch Turkevich synthesis[3] and a residence time of 47 s (flow rate of 60 μl^{-1}) at 100 °C in the microfluidic device, gold nanoparticles with an average diameter of 1.8 nm are obtained, as shown in the TEM picture in Fig. 4.2 a.[1] However, the same concentration of citrate and gold in a batch experiment led to an intractable black slurry, while in diluted condition, like in the classic Turkevich synthesis (10 times more diluted than the microfluidic synthesis) Au_{NPs} with an average diameter of 15 nm are obtained (Fig 4.2 b).

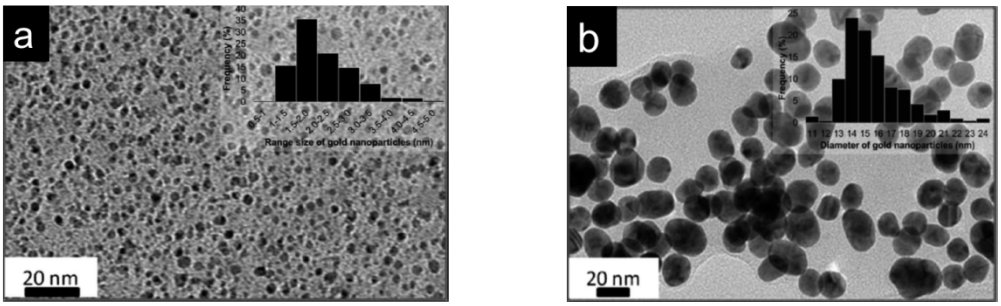

Figure 4.2 Transmission electron microscopy (TEM) images and size distribution of gold nanoparticles obtained **(a)** by microfluidic device at a flow rate of 60 mL min^{-1} (residence time 47 s); **(b)** in a Turkevich glassware synthesis.[1]

In the microfluidic synthesis, by changing the residence time of the reagents into the micro-channel by 35 to 95 s (corresponding to flow rates ranging from 30 to 80 µ L min^{-1}) and maintaining all the other parameters unchanged (Au(III)-citrate ratio= 3.15 and temperature to 100 °C) a slight change in size was observed. Variation of AuNPs DLS distribution with residence time is reported in Fig. 4.3, where the size distribution is much sharper at low residence time widens after 48 s. In parallel, when the residence time is increased, between 35 and 57 s, the diameter decreases from 1.8 to 1.5 nm, while after 57 sec an increase in size up to 3.0 nm is observed (Fig.4.3).

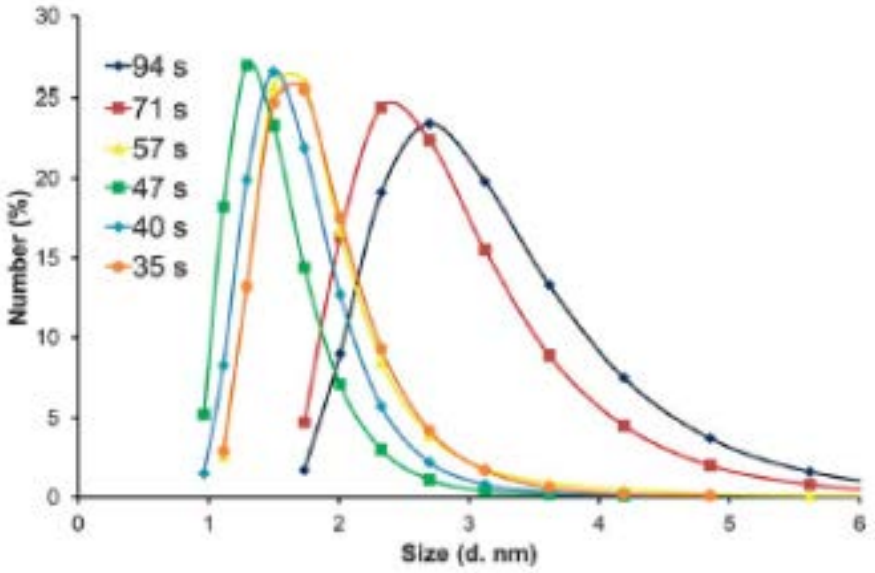

Figure 4.3 Dependence between gold nanoparticle DLS distribution and residence time in the micro-capillary.

Microfluidic gold nanoparticles can be a convenient method to obtain concentrated AuNPs colloids with a narrow size distribution in a few seconds of reaction with a tuneable size by using different experimental conditions. The fast reduction is comparable to that of a strong reducing agent, like $NaBH_4$, where the fast heat transfer and the quick mixing permit to obtain smaller nanoparticles.

In this scenario the importance of understanding the mechanism of the gold nanoparticle formation inside the micro-channel plays a critical role in evaluating which parameters govern the

synthesis (residence time, pH, etc.). Many mechanisms are proposed in the literature (see introduction) but they are still unclear due to i) the short times involved in growth and nucleation processes, ii) the limited accessibility to *in situ* time-resolved characterization and iii) to the low amounts used to obtain gold colloidal dispersions.

Synchrotron radiation related techniques are suitable for *in situ* characterization of diluted systems and can be used to study nanoparticles formation. Polte *et al.* [4] studied Turkevich synthesis in batch conditions, by SAXS and XANES analysis, and a mechanism with successive steps were proposed (see introduction). The main problem in using the synchrotron radiation is in the fact that X-rays can induce the reduction of the gold precursor.

4.1.2 Microfluidic setup adapted to *in situ* XANES characterization

The microfluidic device was adapted in order to monitor directly the reaction by X-Ray absorption spectroscopy (XAS). By taking the advantage of converting a "time scale" to a "length scale"[i] was possible fallow the reaction along the micro-tube during the synthesis.

As reported in Fig. 4.4 the setup is composed by two syringes driven by the syringe pump. First syringe, containing $HAuCl_4$ (5.4×10^{-3} M) was directly mixed to a second one containing a sodium citrate solution (16.3×10^{-3} M) by a T-mixer and driven to the micro-capillary, placed on the hot-plate. The hot plate, at 85 °C, is vertically positioned at 30 cm from the T-mixer and translated, according to the 'z-axis'. The X-ray spot of 1 mm * 200 □m was directed to the micro-channel section in order to get the best signal.

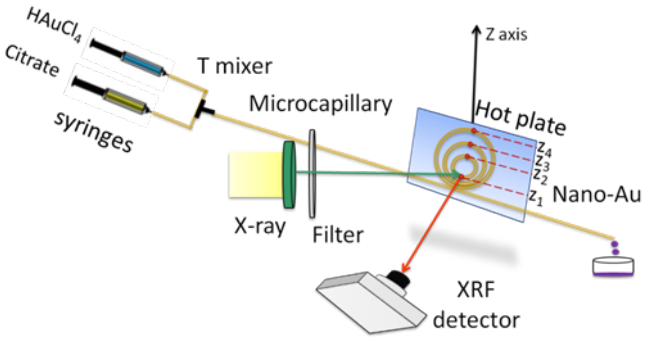

Figure 4.4 Schematic representation of the experimental device.

To prevent beam induced gold reduction,[4] the capillary was washed with water after each spectra acquisition and a fluorescence scan of the internal volume was performed to ensure the

[i] This approach consists in maintaining an infinite time window focused on a rapid physic-chemical phenomenon, which allows time analysis windows above the life time phenomenon.

absence of gold deposition on capillary wall. By previous study on this system,[1, 2] it was assured that the particles formation are correlated to the heating time and not to the flow rates used. By modifying the flow rate and the analysis position along the heated micro-reactor (Fig. 4.4, the different positions are indicated with z_2, z_3 and z_4) it was possible to get XANES spectra at different reaction times, like reported in Table 4.1 .

Table 4.1 Calculated reaction times as function of the location and the reactants flow rate injection.

Flow Rate	50cm	90cm	130cm
30µL.min^{-1}	-	56.5s	81.6s
40µL.min^{-1}	-	42.4s	61.2s
50µL.min^{-1}	-	33.9s	-
60µL.min^{-1}	15,7s	28.2s	40.8s
70µL.min^{-1}	-	24.2s	-
80µL.min^{-1}	-	21.2s	-
90µL.min^{-1}	-	18.2s	-

XANES spectra are very sensitive to the local geometry and the oxidation state associated to the photo-absorbing atom (see introduction), Au in our case. As seen in Chapter 2, the XANES spectrum of the precursor, $HAuCl_4$, is characterized by a sharp peak on the rising edge at about 11920 eV, which is absent in the case of bulk Au(0). This peak, called *white line*, is assigned to a *2p-5d* transition and has been used as an optimal probes of the unfilled *5d* states (Fig. 4.5).[5] As expected, the white line is present in the case of Au(III) precursor being the Au electronic configuration $5d^8 6s^0$, but not in the case of bulk Au, where the electronic configuration is $5d^{10} 6s^1$. On the contrary, two broad peaks are not only characteristics of bulk Au(0) but are missing in the case of $HAuCl_4$. Therefore, the difference in intensity of these features, could be used as an indicator of the Au oxidation state.[6]

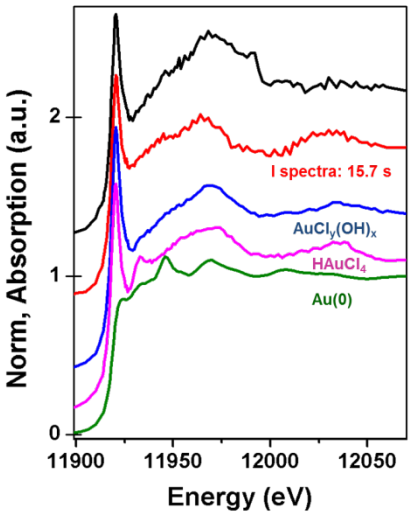

Figure 4.5 Comparison of XANES spectra collected for: $HAuCl_4$ solution, metallic gold Au(0) and $HAuCl_4$ solution with modified-pH to 6 ($AuCl_y(OH)_x$) compared with spectrum collected at 15.7 sec.

The XANES spectra, collected at different reaction times are reported in Fig. 4.6. A decrease in the *white line* intensity for long reaction times was observed, as well as, the formation of XANES sharpness features due to the formation of reduced Au_{NPs}. A detailed analysis of these spectral shapes with reference spectra have permitted to propose a general gold nanoparticles formation mechanism inside the micro-channel (Fig. 4.6).[7]

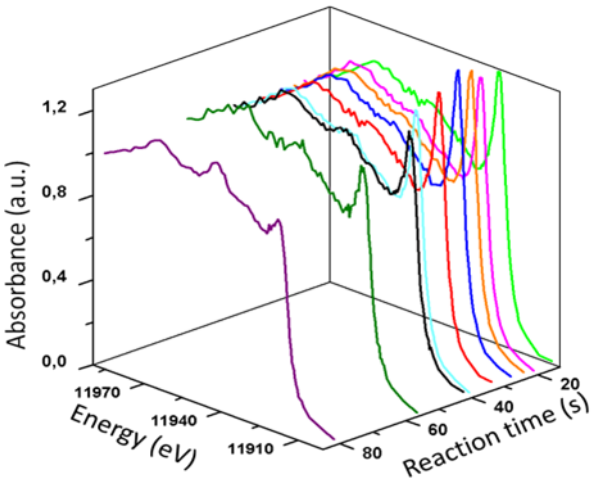

Figure 4.6 XANES spectra collected at different reaction times.

The first step of the reaction was associated to substitution reaction of the chloride ligands of $HAuCl_4$ by OH groups because the XANES fingerprint of recorded at 15.7 sec (Fig. 4.5) was not fitting with the one of $HAuCl_4$ precursor**.** When citrate and $HAuCl_4$ are mixed together, the pH value measured at the output of the T mixer is about 6.5. At this pH hydrolysis of $HAuCl_4$ in aqueous solution is expected. To compare the first spectra collected at 15.7 sec with the hydrolysis

products of gold precursor at pH=6.5 and T=85°C, $HAuCl_4$ solution was introduced to the micro-capillary with a NaOH solution (in place of citrate solution). The NaOH concentration was chosen in order to reach a final pH of 6.5. The comparison of $HAuCl_4$ and $HAuCl_x(OH)_y$ XANES fingerprints exhibit a significant modification of the local structure. It means a "Cl" ligands substitution by "OH" ligands, in good agreement with the observation of Ji *et al.*,[8] where $HAuCl_4$ precursor can exist in different forms depending of pH solution: $AuCl_4^-$, $AuCl_3(OH)^-$, $AuCl_2(OH)^{2-}$, $AuCl(OH)^{3-}$, or $Au(OH)^{4-}$. The coordination sphere substitution of "Cl" with "OH" modifies the electron distribution in the central "Au" cation, and thus, the affiliated XANES fingerprint.

In the range between 0 and 21 sec, the study of collected spectra shows a continuous increase in the rate of reduction of gold (up to 30%). Otherwise, between 20 sec and 35 sec the decomposition of spectra shows two distinct trends, where no evolution in white line is observed. At the same time a significant evolution of the rest of the spectra approaching the fingerprint of the metallic gold reference sheet is observed. These observations lead to hypothesize a gold structuration between 21 and 35 sec. Instead the last period can be attributed to reduction by Au(III) consumption and gold nanoparticles growth.

By these results a multi steps process of particles formation is proposed, as reported in Fig. 4.7, where the 81 % of gold was reduced in 81 sec . The comparison between microfluidic mechanism to those reported in literature for batch mode could be hazardous, as the various forces and interactions within the microfluidic environment can impact the outcome of a reaction.[9]

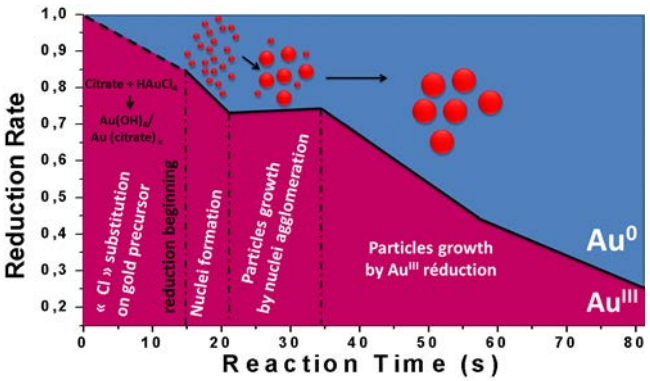

Figure 4.7 Schematic illustration of the gold nanoparticles formation steps in the microfluidic setup.

The first step (0~15s.) involves two competitive steps: ligand substitution and primary nuclei formation. This rapid initial reduction of only a fraction of the precursor is described also by Polte *et al.*[4] and can be attributed to a burst nucleation.

During the second phase (15~35 sec), a significant lack of progress of the nucleation formation rates is observed, that can be explained by $AuCl_x(OH)_y$ complex formation, less reducible

than $HAuCl_4$ precursor.[10] Then, in the range of 21 and 35 sec the almost constant reduction rate and the structuration observed lead to suppose that the particles grow by agglomeration of the initial formed nuclei.

The third phase (35 - 81 sec) includes a rapid reduction of the remaining Au^{III} species (ca. 65%) with a significant growth of the particles. It can be considered that as the $AuCl_x(OH)_Y$ complex is less reducible, the driving force to reduce the remaining $AuCl_x(OH)_y$ complex comes from the coalesced nanoparticles which can react as seeds. In this way the $AuCl_x(OH)_y$ complex, following a random molecular movement in a confined space could be consumed rapidly in the microfluidic system and homogeneously by an autocatalytic reduction process on the surface of the formed nanoparticles.

The second conclusion shows that in situ XANES characterization allow to establish optimized conditions for analysis of few second reactions by characterizations tools, with a time analysis windows of several minutes. Thus the combination of *in situ* XANES analysis with microfluidics technology seems to be a major asset that should be more deeply developed. Indeed, this work presents an example that could be exported to the identification and understanding of other mechanisms that remain unresolved mainly for technical reasons.

4.2 Experimental section

4.2.1 Materials

$HAuCl_4 \cdot 3H_2O$ (99.99%) and sodium citrate (99%) were purchased respectively from Alfa-Aesar and Sigma-Aldrich; Silica capillary[11] with an internal diameter of 200 µm was produced by Polymicro. Syringe pump Phd ultra, Hardvard apparatus was used to . Ultrapure water purified with the Milli-Q plus system (Millipore Co., resistivity over 18 MΩ cm) was used in all cases.

4.2.2 XAS Data Collection

XAS spectra were recorded at Synchrotron Soleil, beam line SAMBA (**S**pectroscopy **A**pplied to **M**aterial **B**ased on Absorption), (Gif-sur-Yevette - Cedex, France). The storage ring was operated at 2.0 GeV in top up mode with a typical current of 300 mA. The data were recorded at Au L_{III} edge in transmission mode using ionization chamber filled with a mixture of Ar, N_2 and He in order to have 10%, 70%, and 95% of absorption in the I_0, I_1, and I_2 chambers, respectively.

The white beam was monochromatized using a fixed exit monochromator equipped with a pair of Si(111) crystals. Harmonics were rejected by using the cutoff of the reflectivity of the Platinum mirror placed at 3 mrad with respect to the beam upstream the monochromator. The precursor Au(III) sample was recorded on a 10 mM solution of $HAuCl_4$ using a suitable cell for liquids, whereas Au_{NPs}/SiO_2-PEI catalysts samples were solid pellets, prepared by mixing the material with cellulose filler. The energies were defined by assigning to 11919 eV the first inflection point of the spectrum of the gold foil. Spectra were collected in sequence and recording Au reference foil before each sample. This allowed a continuous monitoring of the energy during consecutive scans. No energy drifts of the monochromator were observed during the experiments. Spectra were collected with a constant k-step of 0.03 $Å.^{-1}$ with 3 s/point acquisition time from 11730 eV to 12900 eV.

4.3 Conclusion

In summary it has not been possible to distinguish the “Cl” substitution on $HAuCl_4$ precursor and reduction phenomena which should be in competition shows a total substitution (no $HAuCl_4$ detected) and a weak reduction (12% Au). From this observation, it becomes essential to know the order of these two phenomena to interpret more accurately the reaction mechanism. Indeed the reduction rate does not change during the first particles growth stage (21-35s.) and this may be due to the formation of $AuCl_y(OH)_x$ complex which is less reducible compared to $HAuCl_4$ precursor.

References

[1] J. Ftouni, M. Penhoat, A. Addad, E. Payen, C. Rolando, J.-S. Girardon, *Nanoscale* **2012**, *4*, 4450.

[2] J. Ftouni, J.-S. Girardon, M. Penhoat, E. Payen, C. Rolando, *Microsyst. Technol.* **2012**, 18, 151.

[3] J. Turkevich, P.C. Stevenson, J. Hillier, *Discuss. Faraday Soc.* **1951**, *11*, 55.

[4] J. Polte, R. Erler, A. F. Thünemann, S. Sokolov, T. Torsten Ahner, K. Rademann, F. Emmerling and R. Kraehnert., *J. Am. Chem. Soc.* **2010**, *4*, 1076.

[5] B. Abécassis, F. Testard, Q. Kong, B. Francois; O. Spalla, *Langmuir* **2010**, *26*, 13847-13854.

[6] Gardea-Torresdey, J. L.; Tiemann, K. J.; Parsons, J. P.; Gamez, G.; Herrera, I.; Jose-Yacaman, M. *Microchem. J.* **2002**, *71*, 193-204.

[7] A. Tougerti, S. Fazzini, L. Balducci, I. Laoufi, J. Ftouni, E. Fonda, E. Payen, J. S. Girardon, *submitted paper*, 2014.

[8] Turkevich, J., P.C. Stevenson, J. Hillier, *J. Phys. Chem.*, **1953**, *57*, 670.

[9] Y. Song, J. Hormes, and C. S. S. R. Kumar, *Small* **2008**, *4*, 698.

[10] D.V. Goia, E. Matijevic´, Colloids and Surfaces A: Physicochem. Eng. Aspects 146 (1999) 139.

[11] Agilent Technologies 160-2205-5.

CHAPTER 5 ..... .128

5. GOLD NANOPARTICLES ON NANODIAMOND AS NEW GENERATION CATALYST 128

5.1 Results and Discussion 129

5.1.1 Synthesis of Au-NDs 129
5.1.2 Characterization of Au-ND 129
5.1.3 Catalysis 132

5.2 Conclusions 135

5.3 Experimental Section 136

5.3.1 Materials 136
5.3.2 Synthesis of Au-ND 136
5.3.3 Catalysis 136

5.4 APPENDIX 138

CHAPTER 5

Gold nanoparticles on nanodiamond as new generation catalyst

Regular structures of gold nanoparticles (Au_{NPs}) supported by detonation nanodiamonds (DND) were obtained using an aurate salt complex as precursor.[1] Au_{NPs} are formed on the ND surface by a one pot synthesis in acqueous medium, without use of reducing or surfactant agents. The obtained **Au-NDs** system has been fully characterized via transmission electron microscope (TEM), UV-Vis absorption, total energy detector (TED), X-ray energy dispersive spectroscopy (EDS). The catalytic activities had been studied in the reduction of 4-Nitrophenol (4-NP) to 4-Amminophenol (4-AP) with $NaBH_4$ in aqueous media.

5.1 Results and Discussion

5.1.1 Synthesis of Au-NDs

Gold nanoparticles supported by detonation nanodiamonds (**Au-NDs)** were obtained by simply adding an aqueous solution of an aurate imidazolium complex $[Cl_3AuNH_2(CH_2)_2ImMe][AuCl_4]$ to a dispersion of ND in water at room temperature, for 15 minutes under moderate agitation. The obtained dispersion change from a pale gray to pink-red in about 5 minutes, indicating the rapid formation of gold nanoparticles.

This method involves the natural discharge of an aurate imidazolium complex to the surface of nanodiamond without the use of any reducing agents in solution. DND shows a very complex surface with several chemical groups: hydroxyl, etheric and carbonylic groups of β-diketons, ketoester or non-primary amides. Most of these chemical functionalities can directly reduce aurate salt on diamond surface. The ability to control the uniformity of the size, shape, composition, and crystal structure properties of gold nanoparticles interacting with nanodiamonds is essential for assessing their intrinsic catalytic properties. To obtain insight into the evidence of the local nano-structure of assembling noble gold-nanodiamonds nanoparticles, transmission electron microscopy (TEM) coupled with selected area electron diffraction (SAED) and high resolution TEM measurements have been applied. The formation of pure metallic gold was confirmed using X-ray energy dispersive spectrometer (EDS).

5.1.2 Characterization of Au-ND

UV-Vis absorption spectra of **Au-ND** is characterized by a strong absorption at about 522 nm, whereas pure **ND** dispersion does not exhibit any characteristic absorption but only a scattering line (Fig. 5.1).

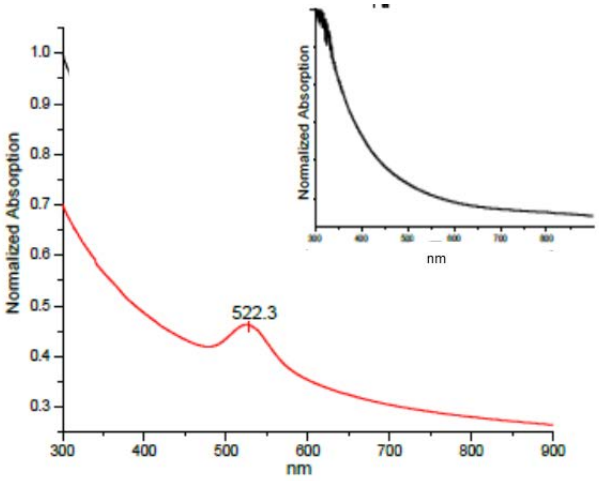

Figure 5.1 UV-vis absorption spectra of aqueous dispersion **Au-NDs**.

Bright field TEM image at low magnification (Fig. 5.2) exhibits an aggregate of NDs in which larger nanoparticles of the darker contrast with the size about 23 ± 5 nm and a spherical shape can be observed. For recognizing the chemical composition of the darker nanoparticles, TEM-EDS mode was applied, probing the electron beam on the nano-aggregate of Fig. 5.2. The chemical composition shows a high purity peaks of gold, confirming the absence of species due to the impurity of the synthesis processes (Cu peaks results from the support grid) (Fig 5.3).

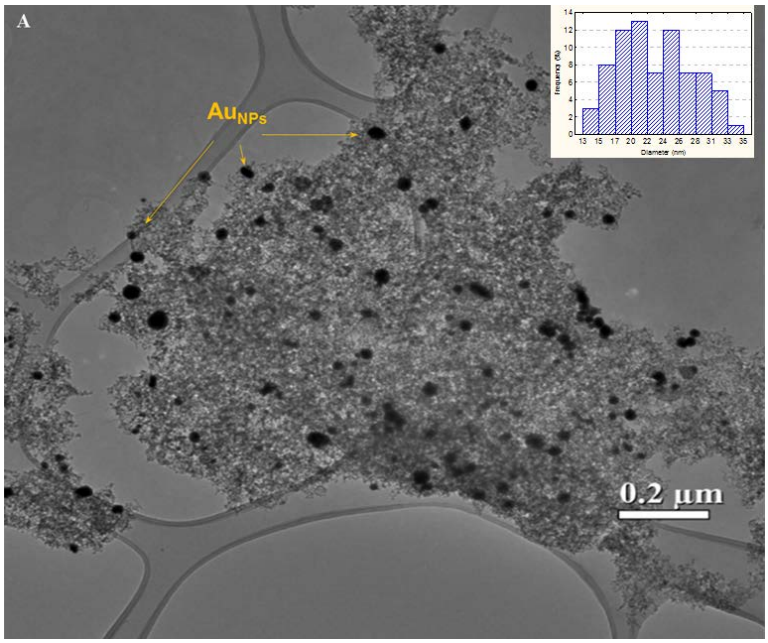

Figure 5.2 Bright field TEM image of an NDs aggregate within gold nanocrystals well-dispersed of dark-contrast (yellow arrows) and size distribution of Au_{NPs} Avarage diameter = 23 ± 5 nm.

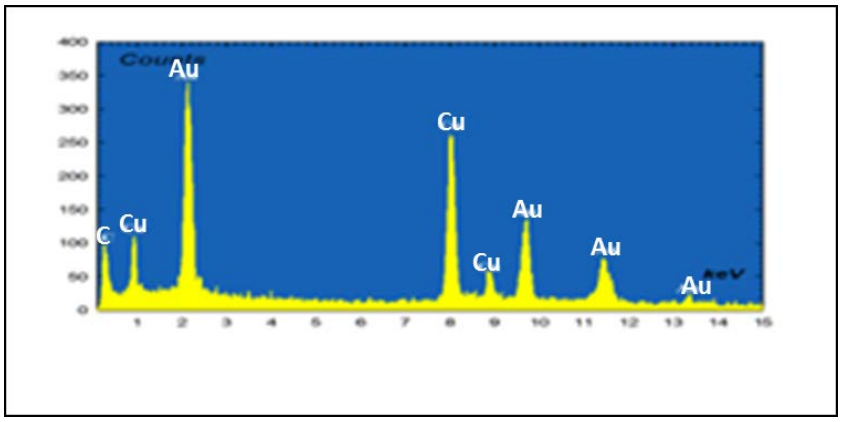

Figure 5.3 EDS spectral image probed on figure **5.3.**

An electron diffraction analysis was performed on aggregate **Au-NDs** nanoparticles (Fig 5.4 b) to establish the crystallographic features. The electron diffraction pattern (EDP) reported in

figure 5.4 shows a superposition of diffraction signals. The diffraction rings belong to **NDs** with typical symmetry of space group *Fd3m* generated by the different crystallographic orientations of the nanodiamonds in respect to the electron beam direction (strong signal rings, white arcs). The diffraction spots have been recognized as face-centered-cubic (*fcc*) gold crystallites of space group *Fm-3m* (few spots, yellow arcs) measuring the d-spacing of the diffraction spots.

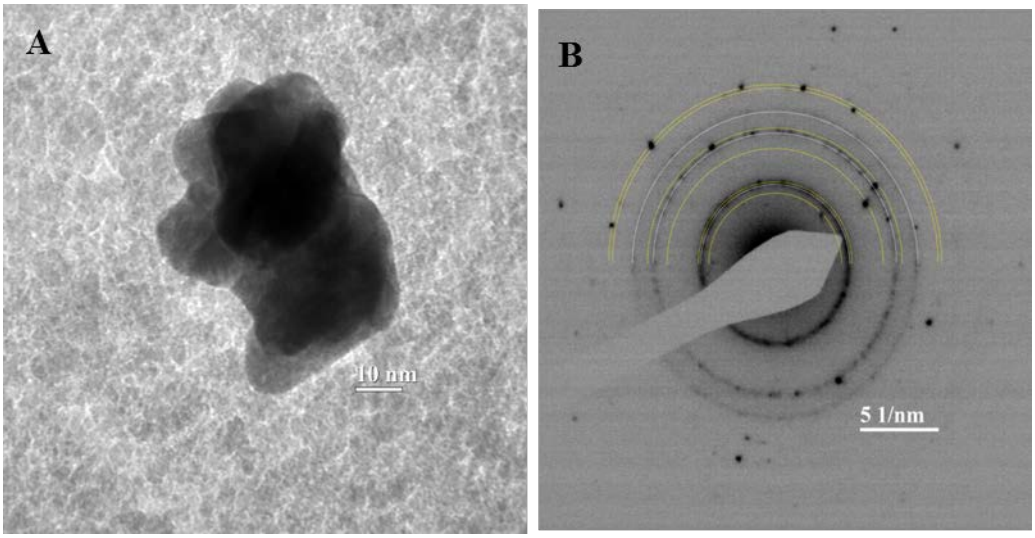

Figure 5.4 a) Bright field TEM image of **Au-NDs** aggregate; **b)** The corresponding electron diffraction pattern taken from figure **a** shows distinct diffraction rings belonging to the cubic ND phase (white arcs) overlapped by diffraction spots belonging to the face-centered-cubic Au phase (yellow arcs).

High resolution electron microscopy image shows nanodiamonds of d_{111} = 0.206 nm lattice spacing deposited on amorphous carbon film (Fig. 5.5 a**)**. Evidence of nanodiamonds interacting with atomic gold layers has been observed in figure 5.5 b. The high resolution image clearly shows a single nanodiamond overlapping with the edge of gold nanoparticle (white arrow).

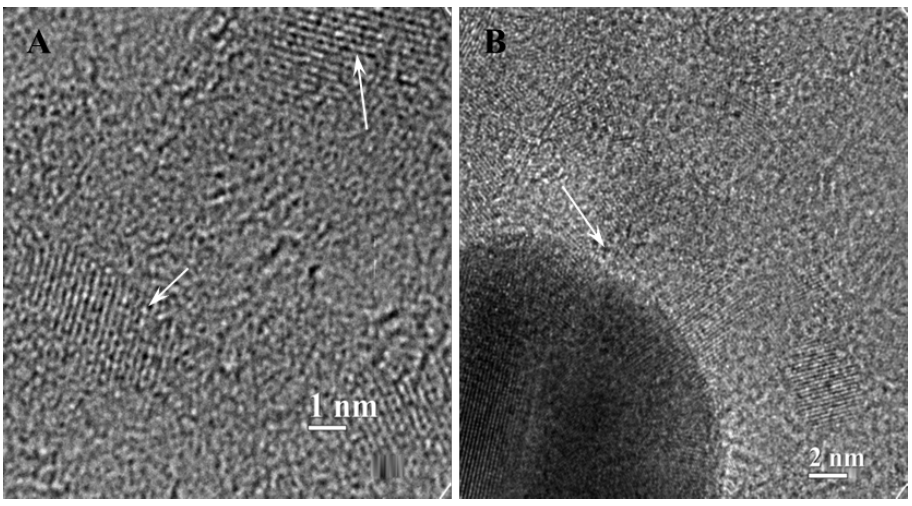

Figure 5.5 High resolution TEM image **a)** nanodiamonds deposited on carbon amorphous film, showing a lattice fringes of d_{111} = 0.206 nm (white arrows); **b)** High resolution TEM image at the edge of **Au-NDs** nanoparticle, showing highly crystalline nature of the gold lattice fringes overlapped by lattice fringes of nanodiamond (white arrows).

5.1.3 Catalysis

As Figure 5.6 shows, the absorption at 317 nm peak, corresponding to nitrophenol, after addition of the $NaBH_4$ is shifted to 400 nm upon the formation of 4-nitrophenolate anion in alkaline conditions. In the absence of the catalyst, this peak remains unaltered for a long duration, indicating the inability of the strong reducing agent $NaBH_4$ to reduce 4-nitrophenolate ion.[2] However, the addition of a very small amount (0.1 mg) of **Au-NDs** to the reaction system caused a fading and ultimate bleaching of the yellow-green colour of 4-nitrophenolate ion in aqueous solution, with a decrease of the absorption at 400 nm and the concomitant appearance of a new peak at 295 nm (attributed to the generation of 4-aminophenolate ion). (Fig. 5.6 b).

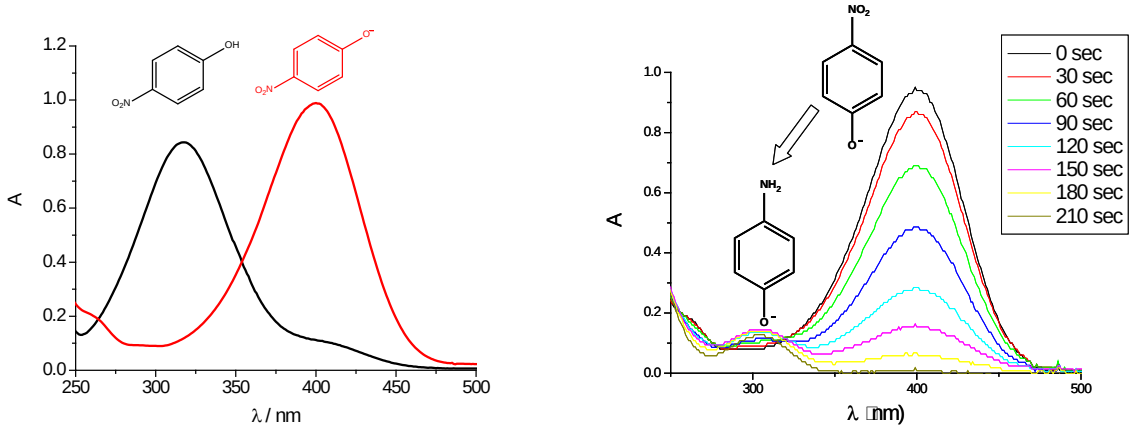

Figure 5.6 a) UV-Vis spectra of 4-NP before (black line) and after adding $NaBH_4$ solution (red line); **b)** UV-Vis spectra of 4-NP reduction in the presence of excess $NaBH_4$ over catalyst **Au-ND**. Reaction conditions: aqueous media at 295 K, 4-NP = 0.15 μmol, $NaBH_4$ = 249 μmol, Au = 9.9 10^{-3} μmol (Au/4-NP/$NaBH_4$ = 1/15/25151).

The rate constants of the reduction process are determined through measuring the change in absorbance at 400 nm. Since the absorbance of 4-NP is proportional to its concentration in the medium, the ratio of absorbance at time A_t /A_0 could be used instead of the ratio of concentrations. Since the concentration of $NaBH_4$ largely exceeds the concentration of 4-NP, the reduction rate could be independent to the concentration of borohydride with a pseudo–first–order kinetics with regard to the 4-NP concentration. The plot of $\ln(A_t/A_0)$ *vs* time is obtained by a straight line whose slope, in absolute value, is the kinetic constant *k*. In this way the kinetic constant for NDs systems, with and without gold was calculated (Fig. 5.7). The *k* reported in table 5.1 are obtained by the average of three measurements for each sample.

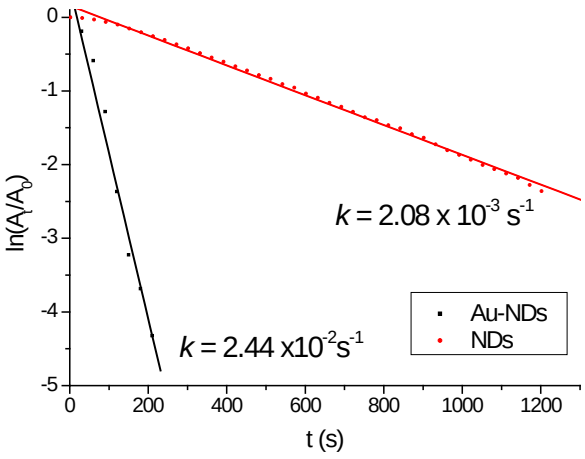

Figure 5.7 Plot of ln(A_t/A_0) versus time for the reduction of 4-NP catalyzed **a)** for **Au-NDs** and **b)** for **NDs**.

Table 5.1 Comparison of kinetic constants (*k*) of **Au-NDs** e **NDs**.

Sample	Au (wt %)	Weight (mg)	*k* (s^{-1})
NDs[a]	-	0.11	$2.08 \pm 0.13\ 10^{-3}$
Au-NDs[b]	9	0.11	$2.4 \pm 0.1\ 10^{-2}$

a Au_{NPs} were not present; $NaBH_4$ /4-NP was 1333/1 (mol/mol);

b The ratio $NaBH_4$ /4-NP/ Au used was 25151/15/1 (mol/mol/mol).

It is known that the reusability is the main advantage of using heterogeneous catalyst rather than homogeneous catalyst, which gives in general better catalytic constants. **Au-NDs** offer an optimum compromise between homogeneous and heterogeneous catalysts.

The kinetic constant of $2.4\ 10^{-2}\ s^{-1}$, comparable with *k* values found for homogeneous catalysis, [3] is much higher than *k* usually obtained for heterogeneous catalyst (in general in the order of 10^{-3} sec^{-1}).[4,5,6] In our case the reduction of 4-NP starts immediately after the addition of small portion of **Au-NDs** (0.1 mg) and in two minutes a totally conversion of 4-NP to 4-AP is obtained.[7] Decreasing the ratio Au/4-NP from 1/30 (mol/mol) to 1/15 (mol/mol) an induction period of 200 sec and a decrease in *k* value was observed (Fig. 5.8). In this condition (i. e. using 0.05 mg of **Au-NDs**) the diffusion rate of the substrate is a ruling factor to determine the reaction rate. [8,9,i]

[i] Esumi *et al* distinguished two steps in the reduction of nitrophenol: (i) diffusion and adsorption of 4-NP to the Au surfaces and (ii) electron transfer mediated by Au from BH_4^- to 4-NP. In heterogeneous catalysts the first diffusion step determined the rate of the reaction, the presence of induction periods might be interpreted as a slow diffusion of the reagents of substrates to Au_{NPs}.

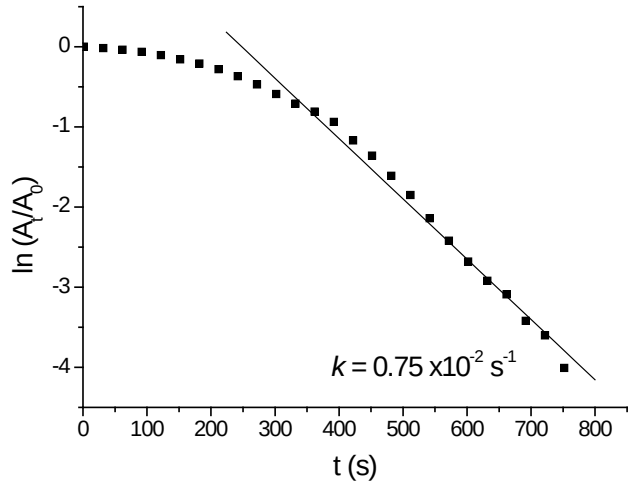

Figure 5.8 Plot of ln(A_t/A_0) versus time for the reduction of 4-NP catalyzed for **Au-NDs** using 0.05 mg of catalyst, and a ratio Au/4-NP=1/15.

It is interesting notice that also **NDs** exhibit catalytic activity in the reduction of 4-NP (Fig. 5.7), with a *k* of $2.1 \cdot 10^{-3}$ sec. This behaviour can be justified by the presence of micro-impurities of iron and other metals as observed in elemental analysis of **NDs** (see appendix). By reducing the amounts of **NDs** (from 0.05 mg) the catalytic activity was not more observed.

Au-NDs was also recovered by simple centrifugation after the first cycle and then washed with water and reused in the next cycle. The decreased catalytic activity with increasing cycles may result from losses of catalyst during the centrifugation and purification processes used (Table 5.2). During the cycles an increment of the induced period is observed (Fig. 5.9). The decrease in catalytic activity and the k calculated are very similar to those observed when less amount of **Au-NDs** (Fig. 5.8) was employed. We can summarize that **Au-NDs** maintain their catalytic activity, but losses of catalyst during the recovery lead to a decreasing in the kinetic constant values.

Table 5.2 *k* using fresh (firs cycle) and recycled (second to fourth) **Au-ND** catalyst.

Uses	*first*	*second*	*third*	*fourth*
k (s^{-1})	2.44×10^{-2}	2.23×10^{-2}	1.31×10^{-2}	0.73×10^{-2}

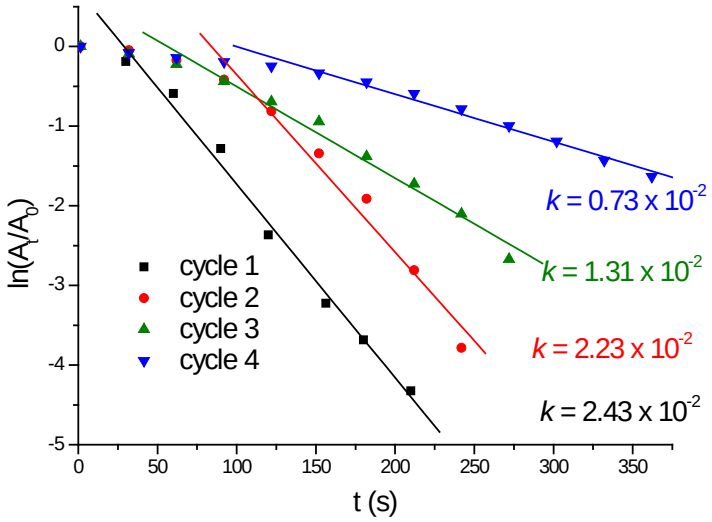

Figure 5.9 Plots of ln(At/A0) versus time for reduction of 4-NP catalyzed by **Au-NDs** for different cycles.

The synergic effect of **NDs** and Au_{NPs}, the small amounts needed for the catalytic tests and the total conversion to 4-AP in short times make **Au-NDs** optimum systems for catalytic purpose.

5.2 Conclusions

A novel recoverable **Au-ND** nanocatalyst was made via direct discharge of an aurate imidazolium gold complex to the nanodiamond surface without the use of any reducing agent. With this method we were able to obtain an Au size distribution of about 23 ± 5 nm. **ND** and **Au-NDs** had been tested as catalysts for reduction of 4-NP to 4-AP. **ND** demonstrated have presence of a catalytic behaviour, with a kinetic constant of 2.08 10^{-3} s^{-1}, due mainly to the presence of impurities. A higher value was obtained for Au-NPs systems, where the synergic effects of **NDs** and Au_{NPs} bring to a *k* value of 2.4 10^{-2} s^{-1}. Furthermore, the Au nanocatalyst was found to be quite stable with excellent catalytic ability up to three catalytic cycles. The small amounts needed for the catalytic tests and the total conversion to 4-AP in short times make **Au-ND** recoverable nanocatalysts optimum systems to convert 4-NP to 4-AP under mild conditions. The use of **NDs** as support was not found before in the literature and this systems can be investigated for other reactions.

5.3 Experimental Section

5.3.1 Materials

Detonation nanodiamond (ND) had been purchased from ITC standard Nanodiamond, purity >98%, 4-5 nm primary particles size. The gold complex $[Cl_3AuNH_2(CH_2)_2ImMe][AuCl_4]$ was prepared as we reporte[10]d in literature.

5.3.2 Synthesis of Au-ND

In a typical reaction 10 mg of purified ND had been dispersed with 100 ml of distilled water. The dispersion had been treated with ultrasounds for 30 min until all the precipitate disappeared. Then 90 ml of the $7 \cdot 10^{-4}$ M Au complex aqueous solution had been slowly added to 30 ml of DND dispersion. The colour of DND suspension immediately changed from a pale gray to pink-red indicating the rapid formation of gold nanoparticles (Au_{NPs}). The reaction mixture had been stirred for 15 minutes, then the dispersion had been centrifuged four times with distilled water and one time with absolute ethanol to remove the organic residues. The solid product had been dried and used in catalytic experiment. An amount of sample was dispersed in water and characterized by UV-Vis absorption. Finally, transmission electron microscopy TEM, selected area electron diffraction SAED analysis and X-ray energy dispersive spectroscopy (EDS) have been performed. Electron microscopy images, electron diffraction pattern, and EDS analysis were performed using a JEOL3000F @300 kV.

5.3.3 Catalysis

In a typical procedure, 0.1 mg of catalyst was added to a quartz cuvettes with 1.68 mL of an aqueous solution of 4-NP (9.0 x 10-2 mM), 3 mL of a freshly prepared $NaBH_4$ solution (0.72 M) and 1 mL of water. The prepared solution in the absence of the catalyst, with 0.15 µmol of 4-NP and 200 µmol of $NaBH_4$, has a characteristic yellow colour with an absorption peak at λ_{max} of 400 nm, corresponding to the formation of the 4-nitrophenolate anion. In the absence of catalyst this peak remained unaltered. As soon as the catalyst was introduced to the solution, a fast blench of the solution was observed, corresponding to the decrease of the intensity of the absorption peak at 400 nm and the concomitant appearance of a new peak at 295 nm attributed to the generation of 4-aminophenolate ion.

The kinetics was monitored by a single beam Hewlett-Packard 8453 diode array recording spectra each 30 seconds in the spectral range of 250 ÷ 500. For the recycling purpose, the catalyst was recovered by centrifugation, washed with water three times and reused.

5.4 APPENDIX

Elemental analysis of **NDs**.

Component	Content, % mass
Fe	0.1
Cr	0.3-0.5
Si	0.15
Al	0.01
Na	0.05
K	0.002
Cu	0.003
Ca	0.01
Mg	0.005
Mn	0.001
Ti	0.002
Non-diamond Carbon (T=20 °C in air)	0.2
Incombustible residue in solid phase, T=800 °C	1.4

References

[1] M. C. Cassani, B. Ballarin, C. Femoni, L. Busetto, *Inorganica Chimica Acta* **2010**, 363, 2055.

[2] B. Ballarin, M. C. Cassani, D. Tonelli, E. Boanini, S. Albonetti, M. Blosi, M. Gazzano, *J. Phys. Chem. C*, 2010, **114**, 9693.

[3]Y. Lin, Y. Qiao , Y. Wang , Y. Yan, J. Huang *J. Mater. Chem.* **2012**, 22, 18314.

[4] K. Kuroda, T. Ishidaa , M. Haruta, *J. Mol. Catal. A: Chemical*, **2009**, 298, 7.

[5] X. Huang,X. Liao, B. Shi, *Green Chem*. **2011**, 13, 280.

[6] B. Ballarin, M. C. Cassani, D. Tonelli, E. Boanini, S. Albonetti, M. Blosi, M. Gazzano, *J. Phys. Chem. C*, **2010**, 114, 9693.

[7]Y. Lin, Y. Qiao , Y. Wang , Y. Yan, J. Huang *J. Mater. Chem.* **2012**,22, 18314.

[8] K. Esumi, K. Miyamoto, T. Yoshimura, *J. Colloid Interface Sci*. **2008**, 323, 105.

[9] K. Hayakawa, T. Yoshimura, K. Esumi, Langmuir **2003**, 5517.

[10] M. C. Cassani, B. Ballarin, C. Femoni, L. Busetto, *Inorganica Chimica Acta* **2010** 363, 2055.